



University of Pennsylvania
ScholarlyCommons


Publicly Accessible Penn Dissertations

2022

Mechanical Properties Of Fibrous Network Materials

Russell Spiewak
University of Pennsylvania

Follow this and additional works at: <https://repository.upenn.edu/edissertations>

 Part of the [Biophysics Commons](#), and the [Mechanical Engineering Commons](#)

Recommended Citation

Spiewak, Russell, "Mechanical Properties Of Fibrous Network Materials" (2022). *Publicly Accessible Penn Dissertations*. 5605.

<https://repository.upenn.edu/edissertations/5605>

This paper is posted at ScholarlyCommons. <https://repository.upenn.edu/edissertations/5605>
For more information, please contact repository@pobox.upenn.edu.

Mechanical Properties Of Fibrous Network Materials

Abstract

We discuss mechanical behavior of specific fibrous network materials, including the evolution of tension in fibrin clots, compression of pulmonary emboli, and fracture of Whatman filter paper. The first material, fibrin clots, consist of random networks of fibrin fibers. When clots form by polymerization they develop tensile pre-stresses. We construct a mathematical model for the evolution of tension in isotropic fibrin gels. As the fiber diameter grows over time, properties which depend on it, such as the stored energy per unit length of a single fiber, the force-stretch relation of a fiber, and therefore the tension in the network as a whole, also evolve over time. The second fibrous network is pulmonary emboli, which consist of random networks of fibrin fibers with fluid-filled pores and red blood cells (RBCs). Stress-strain responses of human pulmonary emboli under cyclic compression were measured, revealing that emboli exhibit hysteretic stress-strain curves characteristic of foams. We describe the hysteretic response of emboli using a model of phase transitions, in which the compressed embolus is segregated into coexisting rarefied and densified phases whose fractions change as compression progresses. Our model takes into account RBC rupture in compressed emboli and stresses due to fluid flow through their small pores. The mechanical response of emboli is shown to vary depending on their RBC content. The third fibrous network is Whatman filter paper. The effect of humidity on properties such as out-of-plane fracture toughness of Whatman filter paper is studied for a broad range of relative humidities. Crack growth is modeled using traction-separation laws, whose parameters are fitted to experiments. Additionally, a novel model is developed to capture the high peak and sudden drop in the experimental force measurement caused by the existence of an initiation region, an imperfect zone ahead of a nascent crack. The relative effect of each independent parameter is explored to better understand the humidity dependence of the traction-separation parameters. The materials studied have biological, clinical, and industrial applications, and the methods described here are also applicable to other fibrous network materials.

Degree Type

Dissertation

Degree Name

Doctor of Philosophy (PhD)

Graduate Group

Mechanical Engineering & Applied Mechanics

First Advisor

Prashant K. Purohit

Subject Categories

Biophysics | Mechanical Engineering

MECHANICAL PROPERTIES OF FIBROUS NETWORK MATERIALS

Russell Spiewak

A DISSERTATION

in

Mechanical Engineering and Applied Mechanics

Presented to the Faculties of the University of Pennsylvania

in

Partial Fulfillment of the Requirements for the

Degree of Doctor of Philosophy

2022

Supervisor of Dissertation

Dr. Prashant K. Purohit

Professor of Mechanical Engineering and Applied Mechanics

Graduate Group Chairperson

Dr. Jennifer R. Lukes

Professor of Mechanical Engineering and Applied Mechanics

Dissertation Committee

Dr. Kevin T. Turner, Professor of Mechanical Engineering and Applied Mechanics and Materials Science and Engineering

Dr. Prashant K. Purohit, Professor of Mechanical Engineering and Applied Mechanics

Dr. John W. Weisel, Professor of Cell and Developmental Biology, Perelman School of Medicine

MECHANICAL PROPERTIES OF FIBROUS NETWORK MATERIALS

COPYRIGHT

2022

Russell Spiewak

ACKNOWLEDGEMENT

This work was partially supported through Department of Education GAANN fellowship grant number P200A160282 to the Department of Mechanical Engineering and Applied Mechanics at the University of Pennsylvania, NSF grant CMMI 1662101, and NIH grant R01 HL135254.

ABSTRACT

MECHANICAL PROPERTIES OF FIBROUS NETWORK MATERIALS

Russell Spiewak

Prashant K. Purohit

We discuss mechanical behavior of specific fibrous network materials, including the evolution of tension in fibrin clots, compression of pulmonary emboli, and fracture of Whatman filter paper.

The first material, fibrin clots, consist of random networks of fibrin fibers. When clots form by polymerization they develop tensile pre-stresses. We construct a mathematical model for the evolution of tension in isotropic fibrin gels. As the fiber diameter grows over time, properties which depend on it, such as the stored energy per unit length of a single fiber, the force-stretch relation of a fiber, and therefore the tension in the network as a whole, also evolve over time.

The second fibrous network is pulmonary emboli, which consist of random networks of fibrin fibers with fluid-filled pores and red blood cells (RBCs). Stress-strain responses of human pulmonary emboli under cyclic compression were measured, revealing that emboli exhibit hysteretic stress-strain curves characteristic of foams. We describe the hysteretic response of emboli using a model of phase transitions, in which the compressed embolus is segregated into coexisting rarefied and densified phases whose fractions change as compression progresses. Our model takes into account RBC rupture in compressed emboli and stresses due to fluid flow through their small pores. The mechanical response of emboli is shown to vary depending on their RBC content.

The third fibrous network is Whatman filter paper. The effect of humidity on properties such as out-of-plane fracture toughness of Whatman filter paper is studied for a broad range of relative humidities. Crack growth is modeled using traction-separation laws, whose parameters are fitted to experiments. Additionally, a novel model is developed to capture the high peak and sudden drop in the experimental force measurement caused by the existence of an initiation region, an imperfect zone ahead of a nascent crack. The relative effect of each independent parameter is explored to better understand the humidity dependence of the traction-separation parameters.

The materials studied have biological, clinical, and industrial applications, and the methods described here are also applicable to other fibrous network materials.

TABLE OF CONTENTS

ACKNOWLEDGEMENT	iii
ABSTRACT	iv
LIST OF TABLES	vii
LIST OF FIGURES	viii
1 Introduction	1
1.1 Biomechanical Origins of Inherent Tension in Fibrin Networks	5
1.2 Structure, Mechanical Properties, and Modeling of Cyclically Compressed Pulmonary Emboli	7
1.3 Humidity Dependence of Fracture Toughness of Cellulose Fibrous Networks	8
2 Biomechanical Origins of Inherent Tension in Fibrin Networks	11
2.1 Introduction	12
2.2 Theoretical Model	14
2.2.1 Fibrin Network Polymerization Model	16
2.2.2 Fiber Radius as a Function of Fibrin Polymerization Time	22
2.3 Force in Helical Rods	23
2.3.1 Tensile Force in a Fiber	32
2.3.2 Kinematics of Fiber Relaxation After Transverse Cutting	35
2.3.3 Continuum Model of Fibrin Gel	40
2.4 Distribution of Fibrin Fiber Lengths	49
2.4.1 Summary of Full Mathematical Model	50
2.5 Discussion	52
3 Structure, Mechanical Properties, and Modeling of Cyclically Compressed Pulmonary Emboli	58
3.1 Introduction	59
3.2 Materials and methods	61
3.3 Modeling framework	62
3.3.1 Fibrin network contribution	62
3.3.1.1 Rarefied Phase	63
3.3.1.2 Densified Phase	63
3.3.1.3 Transition phase	64
3.3.1.4 Cauchy stress to Piola stress conversion	66
3.3.2 RBC contribution	67
3.3.3 Fluid contribution	68
3.4 Model application	69
3.5 Results and Discussion	71
3.5.1 Phase boundary motion	72
3.6 Discussion	73
3.6.1 Stress-strain curves	76
3.6.2 Repeated compression-decompression cycles	78
3.6.3 Response structural dependence	80
3.6.4 Comparison of different emboli	81
3.6.5 Heterogeneity of emboli	82
3.6.6 Comparisons with other studies	84

3.6.7	Implications	88
3.7	Conclusions	89
4	Humidity Dependence of Fracture Toughness of Cellulose Fibrous Networks	91
4.1	Introduction	92
4.2	Materials and Methods	95
4.2.1	Materials	95
4.2.2	Conditioning and Specimen Preparation	95
4.2.3	Out-of-plane Tensile Test	97
4.2.4	Double Cantilever Beam Testing	97
4.3	Theory and Calculations	98
4.3.1	Cohesive Zone Model, Traction-Separation Law, Critical Energy Release Rate, and Non-Dimensional Parameter	98
4.3.2	Finite element analysis	100
4.4	Results and Discussion	101
4.4.1	Experimental Critical Energy Release Rate	101
4.4.2	Finite Element Modeling Results	103
4.4.2.1	Exponential vs. Linear Softening	103
4.4.2.2	Parameters for Different Relative Humidities	103
4.4.2.3	Parametric study	110
4.4.2.4	Comparison of experiments and simulations	112
4.5	Conclusion	113
5	Conclusions	114
	BIBLIOGRAPHY	117

LIST OF TABLES

Table 2.1	Fiber lengths and relaxation times for relaxing fibers	40
Table 2.2	Computed values for stresses for “network” of uniform vertical fibers	55
Table 3.1	Initial and final measurements of emboli	71
Table 3.2	Fitting parameters for emboli #1 and #2	72
Table 3.3	Fitting parameters for emboli #3a, #3b, and #3c	73
Table 4.1	Out-of-plane material properties	102
Table 4.2	Simulation parameters	105
Table 4.3	Simulation parameter values with initiation region	107
Table 4.4	Toughness values from experiments and simulations	113

LIST OF FIGURES

Figure 1.1	Images of fibrous network materials	3
Figure 1.2	Experimental setup to measure inherent tension in fibrin fibrous networks . . .	6
Figure 1.3	Experimental setup to obtain data for cyclical compression of pulmonary emboli	8
Figure 1.4	Reference and deformed configurations of Whatman filter paper DCB specimen	10
Figure 2.1	Cartoon depicting the experimental setup using a rheometer.	13
Figure 2.2	Schematic representation of fibrin fibers	15
Figure 2.3	Average number of protofibrils per fiber cross-section vs. polymerization time	20
Figure 2.4	Parameter study of input parameters to fiber polymerization model	21
Figure 2.5	Tensile force vs. stretch in an individual fiber	34
Figure 2.6	Tensile force in individual fiber vs. polymerization time	36
Figure 2.7	Length of relaxing fiber as it relaxes over time	39
Figure 2.8	Cartoon depicting 8-chain model of fibrous network materials	43
Figure 2.9	Network stress as a function of polymerization time	47
Figure 2.10	Effect of fiber length and radius on network stress, with fixed number density	48
Figure 2.11	Effect of fiber measures on network stress, with fixed solid volume fraction . .	48
Figure 2.12	Probability distributions of fiber lengths and subsequent network stresses . .	49
Figure 2.13	Individual fiber Young's modulus vs. fiber radius	53
Figure 3.1	Experimental setup to obtain data for cyclical compression of pulmonary emboli	61
Figure 3.2	Diagram of rarefied and densified regions in relation to reference frame	65
Figure 3.3	Stress-strain response of embolus #1 to compression and decompression . . .	74
Figure 3.4	Contributions to stress-strain response of embolus #1	75
Figure 3.5	Phase boundary locations for embolus #1	76
Figure 3.6	Stress-strain response of embolus #2 to compression and decompression . . .	77
Figure 3.7	Contributions to stress-strain response of embolus #2	78
Figure 3.8	Phase boundary locations for embolus #2	79
Figure 3.9	Stress-strain response of embolus #3a to compression and decompression . .	80
Figure 3.10	Contributions to stress-strain response of embolus #3a	81
Figure 3.11	Phase boundary locations for embolus #3a	82
Figure 3.12	Stress-strain response of embolus #3b to compression and decompression . .	83
Figure 3.13	Contributions to stress-strain response of embolus #3b	84
Figure 3.14	Phase boundary locations for embolus #3b	85
Figure 3.15	Stress-strain response of embolus #3c to compression and decompression . .	86
Figure 3.16	Contributions to stress-strain response of embolus #3c	87
Figure 3.17	Phase boundary locations for embolus #3c	88
Figure 4.1	Schematic of DCB specimen	96
Figure 4.2	Diagram of finite element simulation	101
Figure 4.3	Comparison of simulations using CPE4 and CPS4 elements	101
Figure 4.4	Force-displacement and energy release rate plots	102
Figure 4.5	Comparisons between simulations with linear and exponential softening . . .	103
Figure 4.6	Force-displacement plots from simulations	104
Figure 4.7	Cohesive parameters and cohesive law at different relative humidities	105
Figure 4.8	Stress profiles along direction of crack propagation	106
Figure 4.9	Cartoon depicting initiation region	107
Figure 4.10	Force-displacement plots from simulations with initiation region	108
Figure 4.11	Simulations with both initiation and steady state regions, compared to only one	109
Figure 4.12	Parametric study	111
Figure 4.13	Results for fixing the <i>NDP</i> in the initiation region	112

Chapter 1

Introduction

Materials comprised of networks of fibers are ubiquitous both in nature and man-made components. Such fibrous network materials include blood clots [1, 2], cytoskeletons [3], collagen networks [4], and other tissues, as well as papers [5–9], carbon nanotube networks [10], felt [6, 11, 12], rubber [13, 14], epoxy [15, 16], gels [17–20], and textiles [6, 11]. Because fibrous network materials are so ubiquitous, it is important to understand the general properties of the materials and the physics and microstructures on which those properties depend. Also, because fibrous networks generally perform a structural function, their mechanical properties are of critical importance. Much research has been done studying such fibrous networks and generalized fibrous network materials, including their formation, fiber properties such as alignment and orientation, and global material properties such as anisotropic moduli, response to tension, compression, and shear, and fracture properties. Works discussing some of these properties will be briefly reviewed shortly.

Properties of general fiber networks have been studied recently by Deogekar and Picu [21], Shahsavari and Picu [22], Picu and Sengab [23], Zhang *et al.* [24], Deogekar *et al.* [25], Deogekar *et al.* [26], Islam and Picu [27] and Deogekar and Picu [28], who have studied cross-linked random fiber networks [21, 22, 25], non-crosslinked random fiber networks with inter-fiber adhesion [23], random fiber networks embedded in an elastic matrix [24], random fiber networks with inclusions [27], and cross-linked fiber networks of cellular shape [25, 26, 28], with large scale finite element simulations. In these works, the fibers are endowed with bending and stretching stiffnesses, and the cross-links connecting the fibers are also endowed with stiffnesses in tension, compression, and shear.

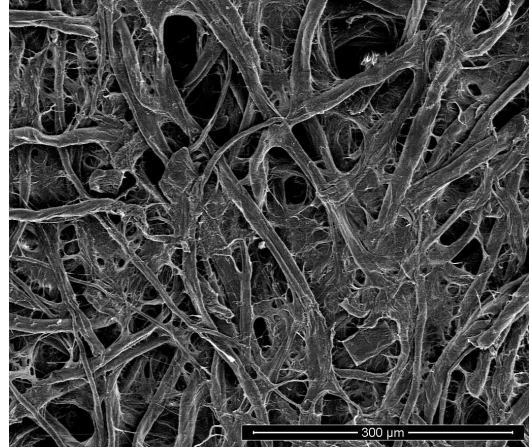
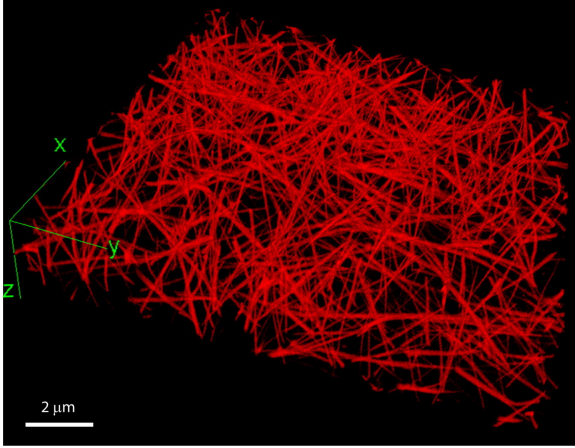
These types of large finite element studies have been going on for at least two decades, if not longer. For example, Onck *et al.* [29] studied strain stiffening of filamentous protein networks in shear using finite element simulations with finite strains of a two-dimensional network model of cross-linked semiflexible filaments. They show that stiffening is caused by non-affine network rearrangements that govern a transition from a bending-dominated response at small strains to

a stretching-dominated response at large strains [29]. Zagar *et al.* [30] numerically studied the elastic properties of a discrete, fully three-dimensional model for an isotropic filamentous networks, where athermal filaments of finite length were interconnected by rigid cross-links. They suggested a relation for the initial network shear modulus as a function of network connectivity, and showed that a nonlinear strain hardening is exhibited when the network is sheared to large strains [30]. Zagar *et al.* [31] used large scale computer simulations of a random network comprised of cross-linked biopolymer-like fibers to explore strain-stiffening trends in biopolymer networks, and suggested two universal stiffening mechanisms [31].

In related work Broedersz *et al.* [32] developed a model for disordered 3D fiber networks to study their linear and nonlinear elastic responses. They determined that responses are primarily controlled by fiber length [32]. Shivers *et al.* [33] considered 2D and 3D disordered networks, comprising interconnected one-dimensional Hookean springs, of varying network geometries, to study anomalies in the Poisson effect and strain fluctuations. They demonstrated that these phenomena are controlled by a collective mechanical phase transition that occurs at a critical uniaxial strain that depends on network connectivity [33]. All of these studies used large scale simulations and focused on tension and shear.

In a slightly different approach based on combining Kinetic Monte Carlo techniques for bond-breaking with finite element simulations of beam networks, Abhilash *et al.* [34] presented a computational model to capture cell-mediated remodeling within fibrous matrices using large scale finite element-based discrete fiber network simulations. They quantified the effect of cell contractility and cell shape anisotropy on matrix remodeling and force transmission [34]. Ban *et al.* [35] developed these ideas further and used large scale fiber network simulations to model plastic deformation by the formation of new cross-links between fibers [35]. Ban *et al.* [36] used a microstructural network model and a coarse-grained constitutive framework that predicts the network Poisson effect and stress-strain responses in uniaxial, biaxial, and triaxial modes of deformation as a function of the microstructural properties of the network, including fiber mechanics and pore size of the network. They found that accounting for the Poisson effect leads to a 100-fold increase in the perceived elastic stiffness of thin collagen samples in extension tests [36].

All of the above authors studied important properties of fiber networks, but they used large scale computer models or finite element simulations. Our approach in this dissertation is different because we do not use computer simulations of discrete fiber networks to analyze their mechanical behavior.



(a) 3D reconstruction of hydrated fibrin network [37].

(b) SEM image of Whatman filter paper [38].

Figure 1.1: Images of fibrous networks materials. (a) 3D reconstruction of hydrated fibrin network using fluorescent confocal microscopy [37]. (b) SEM image of a surface of Whatman filter paper [38]. Images reproduced with permission from the authors.

Instead, we describe the mechanics of fiber networks in terms of continuum models that are far less computationally intensive and reveal physical insights that would be difficult to deduce from a finite element simulation of a network of discrete fibers.

Here, we focus on more specific fibrous network materials such as fibrin fiber networks in blood clots, pulmonary emboli, and Whatman filter paper cellulose networks, and on specific behavior such as development of pre-stress, compression, and fracture. These materials specifically are comprised of randomly oriented, relatively stiff, straight fibers that are joined together to form networks (see Figure 1.1). Studies of these types of polymeric hydrogel fibrous networks began originally with deriving nonlinear models for rubbers and rubber-like materials [13, 14, 39–41] from existing elastic theories, as well as from fluid-saturated porous soils [42], since these hydrogel materials also contain liquid. Based on these and their derivative works, analytical models of the response of fibrous networks to compression have been developed in [6, 43]. Works such as [1, 44] have also incorporated concepts of fiber buckling from analytical models of foams [45] and a continuum theory of phase transitions [46] to connect the densified phase, in which fibers have bent and buckled and the network has become more compact, to the rarefied phase, in which all fibers are still straight, with an intermediary phase in which some fibers are still straight but some have bent or buckled. The framework derived from these studies can be adapted for the networks of randomly oriented, relatively stiff, straight fibers connected together through weak bonds. These materials differ from

material such as aegagropilae in which the fibers are interwoven and held together only by friction [47], and also from thermoresponsive materials such as agarose gels [48] and poly(*n*-isopropylacrylamide) [p(NiPAm)] gels [18–20] which behave as colloidal suspensions above a volume phase transition temperature (VPTT) [18] or lower critical solution temperature (LCST) [20] and then gelate due to ionic cross-linking or protein configuration transition.

Additionally, the mechanical properties studied here comprise three stages of life that materials frequently will experience: first, fiber strands grow and connect to become a network, and the material forms; then, natural forces act upon the material, resulting in physical and structural changes in the material; and finally, the material undergoes failure processes, and the material breaks down. These stages are represented here in the following fashion: First, the growth of a fibrous network material, specifically a fibrin network, is studied analytically from the level of individual fibers and their molecular polymerization, from which material properties are extracted using an 8-chain model [41, 49–51]. Then, since such a material in nature experiences forces which act upon it and change its structural and physical properties, the loading and unloading cycles of compression and decompression experienced by fibrin network blood clots and thromboemboli in veins are simulated here by cyclical compression and decompression of *ex vivo* pulmonary emboli between parallel rheometer plates. Finally, a common failure process is fracture under tensile forces, which is modeled here using continuum cohesive zone traction-separation laws and small scale finite element analysis of Whatman filter paper cellulose fibrous networks. The work here differs from previous studies mentioned earlier in that we do not perform large scale finite element calculations, rather we focus on continuum mechanical models to study mechanical behaviors of these networks. Unlike large finite element calculations, these continuum mechanical models are built to capture specific mechanical behaviors, and their origins are in disparate fields which have little to do with networks. Additionally, the models derived for each of the specific materials can be applied to the other materials discussed, as well as to other fibrous network materials, with some parameter changes and possibly other minor variations.

1.1 Biomechanical Origins of Inherent Tension in Fibrin Networks

Blood forms clots to fuse tears in blood vessels, in order to stop hemorrhaging and heal wounds. Blood clots are composed of networks of fibrin fibers, and often have red blood cells (RBCs), among many other types of cells, lodged between fibers. The pre-cursor molecule to the formation of a clot is fibrinogen. Fibrinogen is transformed into fibrin monomers by the cleavage of fibrinopeptides by thrombin. The fibrin monomers then aggregate in register into half-staggered, double-stranded oligomers, which lengthen into protofibrils. Next, protofibrils aggregate laterally to form fibers, which over time then branch to yield the three dimensional networks which constitute the structural scaffolding of blood clots [52]. Since the minimum energy conformation of protofibrils is when they are straight rather than bent [53], the outer protofibrils of the helical fiber store more energy in their curvatures than do protofibrils closer to the central stem of the helical fiber. The fiber bundle will stop growing in diameter when the energy required to bind another protofibril to the bundle becomes less than the energy required to stretch and bend the protofibril around the helical fiber [53].

Once the clot forms from the fiber bundles, it can serve its purpose to fuse tears in blood vessels. To serve its purpose of healing wounds, the clot pulls the edges of the wound closer together so that growth/repair can occur. The clot must be in tension in order to close the wound; the tension is generated actively by platelets which grab adjacent fibrin fibers and contract [52, 54–56]. However, in this dissertation we show that a polymerizing fibrin network develops a pre-tension even in the absence of platelets. The magnitude of pre-tension and its evolution with time was inferred from experiments carried out in a parallel plate rheometer with fibrin polymerizing between the plates. If the top plate of the rheometer is allowed to move as the clot formed below it the plate was found to move toward the bottom plate just as would be expected in clot contraction. If, on the other hand, the rheometer plates are held fixed, the clot experiences tension instead of contracting, and the stress from this tension on the rheometer plates can be measured (see Figure 1.2).

We will construct a model for the evolution of tension in isotropic fibrin gels by accounting for kinetics of the polymerization reaction that evolves the size of the fibrin fibers in a network model. The model will use a system of ordinary differential equations based on [57] to compute the evolution of the fiber radius from the concentration of fibrin monomers, and the network model will be based

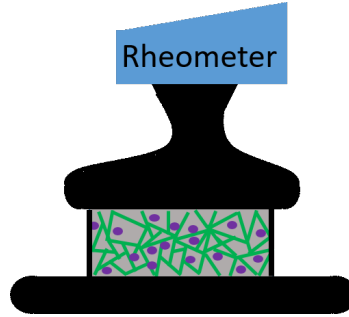


Figure 1.2: Cartoon depicting the experimental setup to measure development of inherent tension in fibrin fibrous networks. Rheometer plates are shown in black. The dark gray shapes represent the fibrin network material, the green lines in the fibrin network material represent the isotropic form of the fiber network, and the randomly placed purple dots represent fibrinogen monomers floating around randomly in the material. Fibrinogen monomers and thrombin are placed between rheometer plates which leads to a polymerization reaction that forms a fibrin network. The rheometer plates are held fixed such that instead of the network contracting, a tension in the network develops. The tensile stress on the rheometer plates is measured as a function of time.

on the Arruda-Boyce 8-chain model [41] used in Brown *et al.* [50] and Purohit *et al.* [51]. As the fiber radius grows over time, properties which depend on the fiber radius, such as the stored energy per unit length of a single fiber, the force-stretch relation of a fiber, and therefore the tension in the network as a whole, will also change over time.

The inherent tension of fibrin clots has a number of conceivable biological implications. First, it may comprise a thermodynamic mechanism to control the diameter of fibrin fibers, as the lateral aggregation of protofibrils stops when the protofibril stretching energy surpasses the energy of bonding [53]. Since fiber diameter is related to a network porosity, fiber length, branch point density, etc., the inherent tension of fibrin clots may modulate the overall network structure. Second, the inherent tension in fibrin fibers can affect the rate of fibrinolysis both at the individual fiber level [58–60] and in whole clot [61] because susceptibility of fibrin to fibrinolytic enzymes depends strongly on the mechanical tension of the proteinaceous fibrous substrate. In aggregate, modulation of the structure of a fibrin network along with the tension of fibers can affect mechanical and enzymatic stability of entire blood clots and thrombi that determine the course and outcomes of various hemostatic disorders [37, 62]. Notably, the magnitude of inherent tension in fibrin networks should be quite variable since it must depend on multiple local and systemic influences that determine fibrin polymerization, including physiological and pathological variations in blood composition.

1.2 Structure, Mechanical Properties, and Modeling of Cyclically Compressed Pulmonary Emboli

As mentioned previously, blood forms clots comprised mostly of a network of fibrin fibers to fuse tears in blood vessels, in order to stop hemorrhaging and heal wounds. However, clots can also form in veins and blood vessels if the flow rate becomes too low. These clots can be compressed by muscular contractile forces and can undergo densification by platelet action, becoming thrombi. The thrombi can break off from the vessel walls, forming emboli. The emboli then flow down the bloodstream, and can obstruct the flow of blood with fatal consequences. For example, pulmonary embolism occurs when blood flow to a part of the lungs is blocked by a venous thrombus that has traveled from the lower limbs. Thrombi are subject to many types of forces, such as those generated in the vasculature by blood flow and those generated by platelets pulling on fibrin in clot contraction, and forces as a result of muscle contraction of the vessel wall, cardiac muscle, and striated muscles adjacent to the blood vessels, especially in the veins of the lower limbs. Therefore, to understand how clots help in healing wounds and to more effectively prevent their negative consequences, it is necessary to understand the mechanical properties of clots and their response to compression, shear, and tension.

As mentioned previously, blood clots are composed of networks of fibrin fibers, and often have red blood cells (RBCs), among many other types of cells, lodged between fibers. The formation of clots has been extensively studied, but the mechanical properties of clots and emboli are not as well understood. As the primary function of clots is mechanical, specifically to stop the flow of blood, understanding the mechanical responses of blood clots to various stimuli, such as radial compression (as occurs in the compression and decompression of arteries and veins) and oscillatory shearing (as experienced by blood flow being pumped due to the beating of the heart), is important. A number of models have been developed to quantify and help to understand the mechanical properties of blood clots, including compressive studies of platelet-poor, platelet-rich and whole blood clots [63]. It has been demonstrated that fibrin networks exhibit foam-like behavior under compression [44]. Most of those studies of clot mechanics, including compression of blood clots, have been carried out *in vitro* using clots made only of fibrin or whole blood [63–66], but the structure of *in vivo* thrombi or emboli differ [67]. Understanding the nuances in mechanical properties of *in vivo* emboli will garner a deeper understanding of thromboembolisms, therapeutic disintegration, and removal

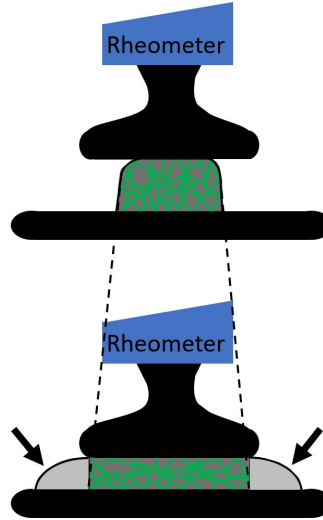


Figure 1.3: Experimental set-up to obtain rheological data for compression experiments. Schematic illustration of compression of an embolus placed between the rheometer plates. Rheometer plates are shown in black. The dark gray shapes represent the embolus, while the light gray shape represents the liquid expelled from the embolus during the compression cycle. The embolus was compressed as the upper rheometer plate moved down, squeezing liquid out of the embolus. Dashed line shows changes in area after the embolus was compressed. Arrows indicate liquid expelled from the embolus. The green lines in the embolus represent the isotropic form of the fiber network.

of intravascular thrombi using mechanical means such as ultrasound, aspiration, and mechanical thrombectomy.

Here, we will develop a model similar to [63], but for *ex vivo* emboli instead of *in vitro* blood clots, for the response of emboli to compression (see Figure 1.3). The emboli come from patients post-mortem, and are subject to cycles of compression and relaxation in different ranges of strain. Our model will account not only for the response to compression of the fibrin network and red blood cells (RBCs) similar to work in previous literature (such as [63]), including the pre-stress of the fibrin network derived from the previous discussion (see Section 1.1) and [68], but also the fluid flow that results from RBC lysis, which we develop from basic principles.

1.3 Humidity Dependence of Fracture Toughness of Cellulose Fibrous Networks

Experiments exploring fracture properties of pulmonary emboli could be difficult to perform, due to the difficulties involved in their proper adhesion to testing apparatuses; even fracture of fibrin

networks in blood clots has only been recently studied [69, 70]. As such, here we develop a fracture model using cellulose, a fibrous network material on which experimentation is much easier. Cellulose fibrous networks and fibrin networks in pulmonary emboli and blood clots are similar in that they both consist of networks of randomly oriented, relatively stiff, straight fibers, but fibrin network gels can stretch to much higher strains [50], even up to 100 or 200% [71], before failure, whereas the strains experienced by cellulose fibrous networks before failure are still securely in the linear elastic regime. As such, the same theory developed here can be applied to pulmonary emboli and fibrin networks in blood clots, and, in fact, to other fibrous networks with randomly oriented, relatively stiff, straight fibers, with some modifications and parameter changes.

Cellulose is an abundantly available polymer in nature. Cellulose networks have good mechanical [72, 73] and barrier [74] properties. Copy paper is a cellulose network which consists of a parallel array of cellulose fibers bound together by the polymer, lignin, whereas filter paper is a cellulose network consisting of pure cellulose fibers bound to each other mechanically by entanglement and chemically by hydrogen bonds. The fibers are flattened hollow tubes, typically 25 to 35 microns wide with thickness 1 to 4 microns. A paper sheet thus consists of a dense three-dimensional array of fibers, bound together at regions where they cross. The strength of a paper sheet arises from the strength of fibers and the number and strength of the fiber-fiber bonds. When paper is loaded in tension, work must be done on the specimen to produce permanent deformation by breaking inter-fiber bonds (namely, a surface area of multiple hydrogen bonds connecting two fibers) [75, 76] and removal of micro-crimps. These cellulose networks can fail when subjected to tensile loads during manufacture or in subsequent converting operations. It has been demonstrated [77] that these failures often occur by rapid propagation of pre-existing flaws, such as notches or creases. On account of the presence of a stress concentration around the flaw, the stress at which failure occurs is well below the strength of a sheet without flaws, thus making fracture toughness, the ability to resist crack growth, of cellulose networks an important performance parameter to be studied.

The objectives of this work are to characterize the out-of-plane z-direction fracture of cellulose networks using cohesive zone modeling and filter paper (a porous 100% cellulose network) as a function of humidity. Using a double cantilever beam (DCB) configuration, cohesive zone modeling, and finite element simulations, we study the dependence on humidity of the toughness value and other cohesive parameters of Whatman filter paper cellulose networks. Continuum cohesive zone models provide the convenience of tuning a few parameters such as peak stress and separation at

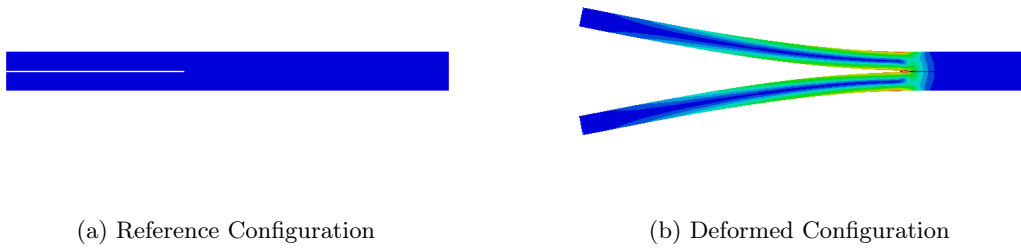


Figure 1.4: Depiction of the (a) Reference configuration, and (b) Deformed configuration, of a Whatman filter paper specimen in the double cantilever beam (DCB) geometry.

failure to model one-dimensional fracture propagation. Use of cohesive zone models also allows us to bypass expensive finite element simulations of discrete fiber networks which require the specification of a host of parameters for the fibers and bonds. For these reasons, and since we do not have control over individual fiber and fiber-fiber bonds properties in cellulose networks, we describe the fracture behavior through continuum traction-separation laws. We perform finite element simulations and input cohesive parameters (see Figure 1.4), and then calculate the toughness values using the traction-separation law from the cohesive zone model. We then compare our results to experimental data.

Chapter 2

Biomechanical Origins of Inherent Tension in Fibrin Networks

This chapter is based on work published in [68] R. Spiewak, A. Gosselin, D. Merinov, R. I. Litvinov, J. W. Weisel, V. Tutwiler, and P. K. Purohit. “Biomechanical origins of inherent tension in fibrin networks”, *Journal of the Mechanical Behavior of Biomedical Materials*, (*In Preparation*).

Abstract

Blood clots form at the site of vascular injury to seal the wound and prevent bleeding. Clots are in tension as they perform their biological functions and withstand hydrodynamic forces of blood flow, vessel wall fluctuations, extravascular muscle contraction and other forces. There are several mechanisms that generate tension in a blood clot, of which the most well-known is the contraction/retraction caused by activated platelets. Here we show through experiments and modeling that clot tension is generated by the polymerization of fibrin. Our mathematical model is built on the hypothesis that the shape of fibrin monomers having two-fold symmetry and off-axis binding sites is ultimately the source of inherent tension in individual fibers and the clot. As the diameter of a fiber grows during polymerization the fibrin monomers must suffer axial twisting deformation so that they remain in register to form the half-staggered arrangement characteristic of fibrin protofibrils. This deformation results in a pre-strain that causes fiber and network tension. Our results for the pre-strain in single fibrin fibers is in agreement with experiments that measured it by cutting fibers and measuring their relaxed length. We connect the mechanics of a fiber to that of the network using the 8-chain model of polymer elasticity. By combining this with a continuum model of swellable elastomers we can compute the evolution of tension in a constrained fibrin gel. The temporal evolution and tensile stresses predicted by this model are in qualitative agreement with experimental measurements of the inherent tension of fibrin clots polymerized between two fixed rheometer plates. These experiments also revealed that increasing thrombin concentration leads to increasing internal tension in the fibrin

network. Our model may be extended to account for other mechanisms that generate pre-strains in individual fibers and cause tension in three-dimensional proteinaceous polymeric networks.

2.1 Introduction

Blood clots are formed at the sites of vessel wall injuries to seal or plug the damage and stem bleeding. Clots result from multiple reactions that involve blood cells and plasma components, including fibrinogen, the soluble protein converted enzymatically to insoluble fibrin [52]. A three-dimensional polymeric fibrin network comprises the scaffold of a blood clot and, in combination with embedded platelets and red blood cells [1], largely determines the clot's biological and mechanical properties.

To fulfill its biomechanical function and prevent or stop bleeding, the blood clot and the fibrin scaffold must have certain mechanical resilience to be able to withstand hydrodynamic forces of blood flow, pulsation of a vessel wall, extravascular muscle contraction, and more [37]. Among many factors that contribute to the mechanical behavior of fibrin, one of the least studied is the physiological tension of the fibrin network generated by at least two mechanisms. The most apparent and well-studied is the external traction and compression of fibrin clots driven by activated platelets, with each individual platelet exerting contractile forces on the order of tens of nano-Newtons on adjacent fibrin fibers [54–56, 78]. However, there is strong evidence that fibrin clots generate inherent (internal or intrinsic) tension unrelated to platelet contractility or any other external mechanical perturbations. For example, the individual hydrated fibrin fibers observed in a light microscope are straight, not sinuous, suggesting that each fiber is under inherent tension [79]. Tension of individual fibrin fibers was introduced in [53], and their elasticity has been shown and quantified in AFM pulling experiments [80] and by active flexing or stretching a separate fibrin fiber using optical tweezers [81]. Finally, the inherent fibrin fiber tension has been established directly by severing these fibers and watching them retract [60]. If a great number of such taut individual fibers form a three-dimensional network, then the entire network must also be under tension. From the general theory of polymer mechanics, tension is self-generated in the polymers that possess some degree of non-uniformity and thermodynamic instability of the major structural elements [82, 83]. The complex spatial axial and lateral packing of the fibrin monomers and oligomers dictates their deviation (stretching) from the relaxed and stable conformational state that provides a fundamental structural and thermodynamic

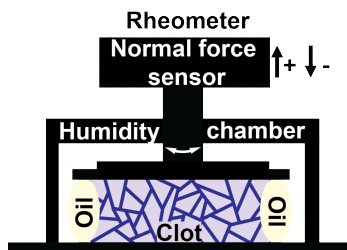


Figure 2.1: Cartoon depicting the experimental setup using a rheometer. Testing apparatus, including rheometer plates, force sensor, and humidity chamber, are shown in black. The light purple shape represents the fibrin network material, the purple lines in the fibrin network represent the isotropic fiber network, and the off-white ovals next to the clot represent the mineral oil added to prevent sample drying during testing. The rheometer plates are held fixed such that a tension in the network results in pulling on the upper plate.

basis for the existence of inherent tension of fibrin networks [84–90].

The inherent tension of fibrin clots has a number of conceivable biological implications. First, it may comprise a thermodynamic mechanism to control the diameter of fibrin fibers, as the lateral aggregation of protofibrils stops when the protofibril stretching energy surpasses the energy of bonding [53]. Since fiber diameter is related to network porosity, fiber length, branch point density, etc., the inherent tension of fibrin clots may modulate the overall network structure. Second, the inherent tension in fibrin fibers can affect the rate of fibrinolysis both at the individual fiber level [58–60] and in whole clot [61] because susceptibility of fibrin to fibrinolytic enzymes depends strongly on the mechanical tension of the proteinaceous fibrous substrate. In aggregate, modulation of the structure of a fibrin network along with the tension of fibers can affect the mechanical and enzymatic stability of entire blood clots and thrombi that determine the course and outcomes of various hemostatic disorders [37, 62]. Notably, the magnitude of inherent tension in fibrin networks should be quite variable since it must depend on multiple local and systemic influences that determine fibrin polymerization, including physiological and pathological variations in blood composition.

Here, our goal is to construct a mathematical model for the evolution of tension in isotropic fibrin networks by accounting for the kinetics of the fibrin polymerization reaction that regulates the size and structure of the fibrin fibers in a network model, accounting for the idea in [53] that twisted monomers make a twisted protofibril, and the aggregation in register with a $22.5nm$ repeat introduces tension. In the following we describe a model for capturing the evolution of tension in a fibrin gel, as the fibers in the network polymerize between rheometer plates (see Figure 2.1). We show how tension develops in a polymerizing fibrin fiber as its diameter increases, then use this

information in a continuum model to predict the evolution of tension in a constrained fibrin clot.

2.2 Theoretical Model

The basis of this mathematical model is that each fiber making up the fibrin network is under tension, and the tension increases as the fiber diameter increases due to polymerization. The existence of tension in fibrin fibers has been demonstrated by cutting individual fibers and observing their retraction [60]. The origin of tension in fibrin fibers is not known, but it may have to do with the spatial geometry of monomeric fibrin and oligomeric protofibrils [53, 92]. The protofibrils making up a fibrin fiber are twisted into a helical shape in their stress-free state due to small axial twisting of the fibrin monomers that polymerize axially and laterally (see Figure 2.2(a) and Figure 2.2(b)). When they come together to form a fiber, the molecules making up a protofibril must be in registry [53, 94], or properly aligned perpendicularly, in order for the linkages between them to form properly (see Figure 2.2(c) and Figure 2.2(d)). However, as the diameter of the fiber increases, the stress-free helix must deform in order for the molecules to be in registry (see Figure 2.2(d) and Figure 2.2(e)), leading to some geometric frustration from the opposing forces [95, 96]. This causes strain in the helical protofibrils and induces stress. This stress is ultimately responsible for the tension in a fibrin fiber.

No models exist for quantifying the tension in a fibrin fiber, let alone as a function of its diameter. Here we build such a model by analyzing the deformation of helical protofibrils and considering the change in radius and pitch of a helical rod. The evolution of the diameter of a fiber is given by a system of ordinary differential equations, based on [57], which track the concentrations of various species as the polymerization reaction proceeds. The helical rod model for a fibrin fiber then outputs the tension in an individual constrained fiber as a function of its (evolving) diameter. We show how a single fiber under tension relaxes when the constraint is removed; this mimics recent experiments in which individual fibers are cut and allowed to relax to determine their pre-strain [60]. Next, we connect the mechanics of a single fiber to the constitutive response of a network using the 8-chain model of polymer elasticity [41, 49–51]. We then use a continuum mechanical model of swellable elastomers [97] to predict the network tension as a function of time in a constrained fibrin gel. Initially we let the network solid volume fraction increase while holding constant the number of fibers per unit reference volume, and then we hold constant the network solid volume fraction to

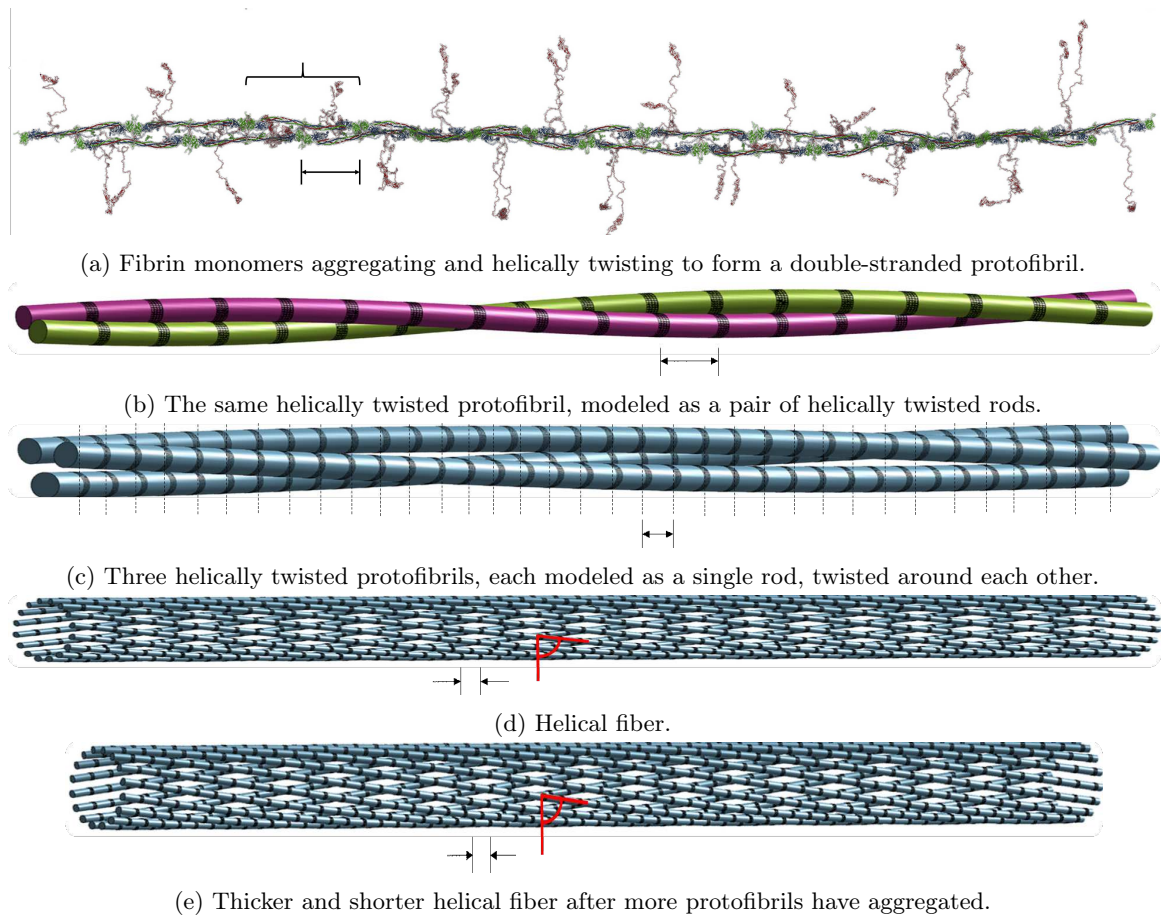
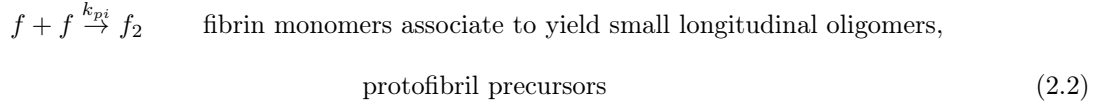
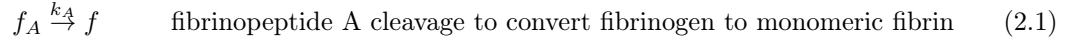


Figure 2.2: Schematic representations of fibrin fibers. (a) A protofibril constructed from fibrin monomers [91], twisted due to the two-axis symmetry and off-axis binding sites [92], depicting the $22.5nm$ half-staggered periodicity. Brace indicates one full monomer. (b) A protofibril modeled as a pair of helical rods. Each rod of the protofibril is comprised of fibrin monomers stacked end to end, twisting around the other rod in a helical fashion. (c) Three helically twisted protofibrils, each formed of the same structure as (b) but depicted and modeled here as a single rod instead, twisted around each other. Dashed lines emphasize the $22.5nm$ vertical striation necessitated to maintain longitudinal periodicity. (d) The outer shell of a helical fiber modeled as a collection of protofibrils helically twisted around the fiber core (not shown). Each protofibril is depicted and modeled here as a single rod. (e) The new outer shell of the same fiber as in (d) after additional protofibril aggregation. When additional protofibrils aggregate onto a growing fiber, the fiber radius gets bigger, but the fiber contracts (i.e., the length of the fiber gets shorter) and the pitch angle α becomes smaller so that the protofibrils can maintain the $22.5nm$ half-staggered registry (although at the scale of this image the difference between the scale bars here and in (d) is difficult to see). Once again, each protofibril is modeled as a single rod. All scale bars are $22.5nm$. All black areas of protein densification [93] correspond to the DED structures in the half-staggered packing. All red angular measures represent the pitch angle α .

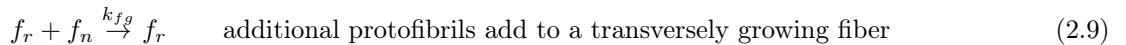
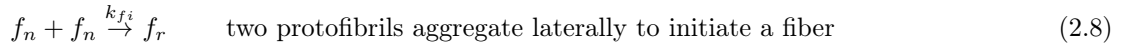
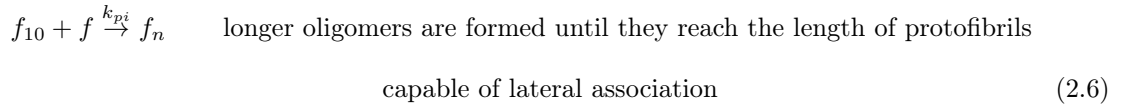
better mimic experiments.

2.2.1 Fibrin Network Polymerization Model

Weisel and Nagaswami [57] propose a system of ordinary differential equations (ODEs), to describe the polymerization of fibrin fibers, comprising fibrin network, from a fibrinogen solution. The polymerization process they describe consists of the following steps – beginning with a concentration of fibrinogen and thrombin (which cleaves the A fibrinopeptides from the fibrinogen to create fibrin monomers), association of fibrin monomers to form double-stranded half-staggered protofibrils, and then aggregation of protofibrils into fibrin fibers, which branch and grow to create the fibrin network gel. Their polymerization process includes a minimum length requirement (which we will call $l_{agg} + 1$) for protofibrils to be capable of aggregation, which produces the observed lag period in the number of protofibrils per fiber. Their model, including the polymerization chemical reaction equations and the resulting system of ODEs, for the example of $l_{agg} = 10$, is given as follows (with some modification of the explanatory text only, to better reflect our current understanding of fibrin polymerization):



⋮



$$\frac{d[f_A]}{dt} = -k_A[f_A] \quad (2.10)$$

$$\frac{d[f]}{dt} = k_A[f_A] - k_{pi}[f] (2[f] + [f_2] + [f_3] + \dots + [f_{10}]) - k_{pg}[f][f_n] \quad (2.11)$$

$$\frac{d[f_2]}{dt} = k_{pi}[f] ([f] - [f_2]) \quad (2.12)$$

$$\frac{d[f_3]}{dt} = k_{pi}[f] ([f_2] - [f_3]) \quad (2.13)$$

⋮

$$\frac{d[f_{10}]}{dt} = k_{pi}[f] ([f_9] - [f_{10}]) \quad (2.14)$$

$$\frac{d[f_n]}{dt} = k_{pi}[f][f_{10}] - 2k_{fi}[f_n][f_n] - k_{fg}[f_r][f_n] \quad (2.15)$$

$$\frac{d[f_r]}{dt} = k_{fi}[f_n][f_n] \quad (2.16)$$

$$\frac{d[f_n^{tot}]}{dt} = 2k_{fi}[f_n][f_n] + k_{fg}[f_r][f_n] \quad (2.17)$$

$$\frac{d[c_{f_n}]}{dt} = 11k_{pi}[f][f_{10}] + k_{pg}[f_n][f] - 2k_{fi}[f_n][c_{f_n}] - k_{fg}[f_r][c_{f_n}] \quad (2.18)$$

$$\frac{d[c_{f_r}]}{dt} = 2k_{fi}[f_n][c_{f_n}] + k_{fg}[f_r][c_{f_n}] \quad (2.19)$$

$$n = \frac{[c_{f_n}]}{[f_n]} \quad (2.20)$$

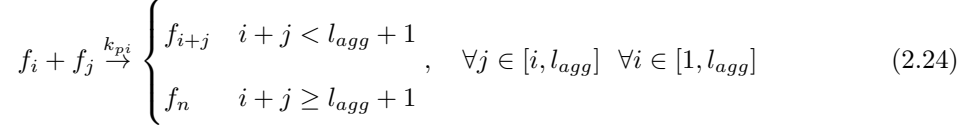
$$m = \frac{[f_n^{tot}]}{[f_r]} \quad (2.21)$$

$$l = \frac{[c_{f_r}]}{[f_n^{tot}]}, \quad (2.22)$$

where f_A represents fibrinogen, f represents fibrin monomers, f_2 through f_{10} represent fibrin oligomers comprised of 2 through 10 monomers, f_n represent protofibrils, f_r represent fibrin fibers, $[f_n^{tot}]$ represents total protofibrils in fibers, $[c_{f_n}]$ represents total fibrin [monomers] in protofibrils, $[c_{f_r}]$ represents total fibrin in fibers, n is the average number of fibrin per protofibril, m is the average number of protofibrils per fiber, and l is the average length of fibers.

Weisel and Nagaswami [57] also mention that the model should also account for longitudinal oligomer-monomer and oligomer-oligomer interactions in the intermediate stages of protofibril formation, which are not explicitly accounted for in the above model. A logical extension to this, which is also mentioned by Weisel and Nagaswami [57], would be to include protofibril growth due to interactions with oligomers, which is also not included in the above model. They additionally describe that a reaction can be included to account for fiber-fiber interactions. Taking these additions into

account, we can write the following chemical polymerization reactions:



These polymerization reactions result in the following system of ODEs:

$$\frac{d[f_A]}{dt} = -k_A[f_A] \quad (2.29)$$

$$\frac{d[f_1]}{dt} = -k_{pi} \left([f_1][f_1] + [f_1] \sum_{i=1}^{l_{agg}} [f_i] \right) - k_{pg}[f][f_n] + k_A[f_A] \quad (2.30)$$

$$\frac{d[f_j]}{dt} = k_{pi} \left(\sum_{i=1}^{\lfloor \frac{j}{2} \rfloor} [f_i][f_{j-i}] - [f_j][f_j] - [f_j] \sum_{i=1}^{l_{agg}} [f_i] \right) - k_{pg}[f_n][f_j] \quad \forall j \in [2, l_{agg}] \quad (2.31)$$

$$\frac{d[f_n]}{dt} = k_{pi} \left(\sum_{j=1}^{\lfloor \frac{l_{agg}+1}{2} \rfloor} \left(([f_j] + [f_{l_{agg}+1-j}]) \sum_{i=l_{agg}+1-j}^{l_{agg}} [f_i] \right) \right) - 2k_{fi}[f_n][f_n] - k_{fg}[f_r][f_n] \quad (2.32)$$

$$\frac{d[f_r]}{dt} = k_{fi}[f_n][f_n] - k_{fA}[f_r][f_r] \quad (2.33)$$

$$\frac{d[f_n^{tot}]}{dt} = 2k_{fi}[f_n][f_n] + k_{fg}[f_r][f_n] + k_{fA}[f_r][f_r] \quad (2.34)$$

$$\frac{d[c_{f_n}]}{dt} = k_{pi} \sum_{i=1}^{l_{agg}} \left((l_{agg} + i) \sum_{j=i}^{\lfloor \frac{l_{agg}+i}{2} \rfloor} [f_j][f_{l_{agg}+i-j}] \right) + k_{pg}[f_n] \sum_{i=1}^{l_{agg}} [f_i] - k_{fi}[f_n][c_{f_n}] - k_{fg}[f_r][c_{f_n}] \quad (2.35)$$

$$\frac{d[c_{f_r}]}{dt} = 2k_{fi}[f_n][c_{f_n}] + k_{fg}[f_r][c_{f_n}] + k_{fA}[f_r][f_r]. \quad (2.36)$$

We retain the same definitions

$$n = \frac{[c_{f_n}]}{[f_n]} \quad (2.37)$$

$$m = \frac{[f_n^{tot}]}{[f_r]} \quad (2.38)$$

$$l = \frac{[c_{f_r}]}{[f_n^{tot}]} \quad (2.39)$$

The parameters in this system are as follows:

- $l_{agg} + 1$, the minimum length for protofibrils to be capable of lateral aggregation: Since the length of protofibrils is about $500nm$ [52, 98] and the half-staggered length of monomers is about $22.5nm$ [52, 53, 93, 98, 99], and thus the number of fibrin monomers in protofibrils are about 20 [52], $l_{agg} = 20$ is chosen.
- f_{A_0} , the initial concentration of fibrin(ogen): $f_{A_0} = 2.8229mg/mL$ is chosen to match the initial fibrin(ogen) concentration value of $5 \times 10^{18} molecules/L$ of Weisel and Nagaswami [57].
- k_A , the rate of fibrinopeptide A cleavage to convert fibrinogen to fibrin monomers: $k_A = 1s^{-1}$.
- k_{pi} , the rate of association of fibrin monomers to yield small oligomers and initiate protofibril formation: $k_{pi} = 6.0 \times 10^{-20} L/molecule s$.
- k_{pg} , the rate of protofibril growth in length by longitudinal association with monomers or shorter oligomers: $k_{pg} = 1.4 \times 10^{-17} L/molecule s$.
- k_{fi} , the rate of protofibril lateral aggregation to initiate a fiber: $k_{fi} = 1.0 \times 10^{-20} L/molecule s$.
- k_{fg} , the rate of fiber growth by association with additional protofibrils: $k_{fg} = 2.0 \times 10^{-16} L/molecule s$.
- k_{fA} , the rate of lateral aggregation of fibers: the value $k_{fA} = 1.0 \times 10^{-19} L/molecule s$ is chosen to be in a similar range as the other rate constants.

The rate constants were selected to be similarly valued to those used by Weisel and Nagaswami [57], and the conditions $k_{pi} < k_{pg}$ and $k_{fi} < k_{fg}$ in Weisel and Nagaswami [57] were ensured.

The output parameter that is most important for this context is m , the average number of protofibrils per fiber cross-sectional area, since that is the one from which the radius of the fiber is

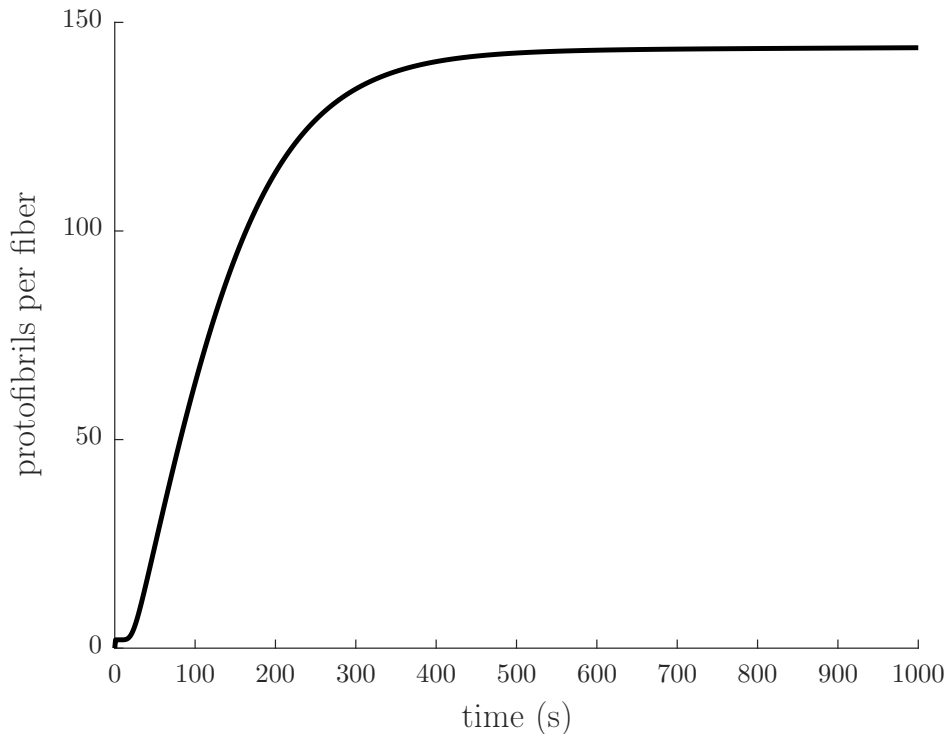


Figure 2.3: The average number of protofibrils per fiber cross-section m over time t , given the input parameters $f_{A_0} = 2.8229\text{mg/mL}$, $l_{agg} = 20$, $k_A = 1\text{s}^{-1}$, $k_{pi} = 6.0 \times 10^{-20}\text{L/molecule s}$, $k_{pg} = 1.4 \times 10^{-17}\text{L/molecule s}$, $k_{fi} = 1.0 \times 10^{-20}\text{L/molecule s}$, $k_{fg} = 2.0 \times 10^{-16}\text{L/molecule s}$, and $k_{fA} = 1.0 \times 10^{-19}\text{L/molecule s}$.

estimated (see Section 2.2.2). For the parameter choice given above, the evolution of m over time can be seen in Figure 2.3.

To study the effect of each parameter on the evolution of m over time, we ran the calculations for a 20% change in each parameter and plotted the results together (see Figure 2.4). As can be seen in Figure 2.4(a), a 20% change in the initial concentration of fibrin(ogen) affects the slope of the increase in thickness: a larger f_{A_0} causes a greater slope. Similarly, as can be seen in Figure 2.4(b), l_{agg} also affects the slope of the increase in thickness, but in the opposite way: a larger l_{agg} results in a smaller slope. In Figure 2.4(c), it can be seen that small changes in k_A have only a very small effect similar to l_{agg} . Figure 2.4(d) shows that small changes in k_{pi} have a similar effect as f_{A_0} , whereas Figure 2.4(e) depicts that small changes in k_{pg} have a similar effect as l_{agg} . Figure 2.4(f) demonstrates that small changes in k_{fi} result in changes in the value of the asymptotic limit plateau region of the average number of protofibrils per fiber m : smaller values of k_{fi} yield larger values of

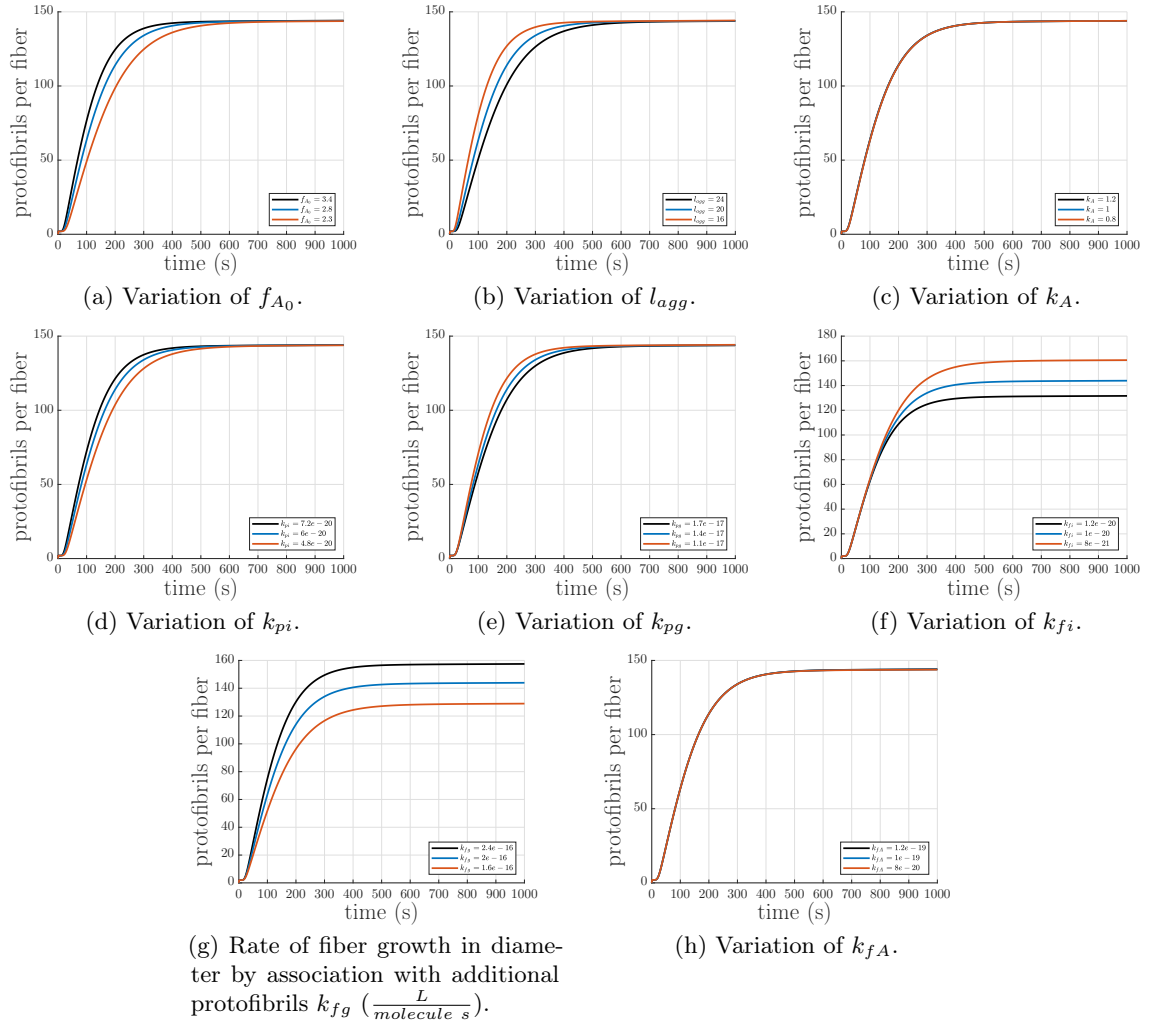


Figure 2.4: Parameter study of the input parameters in the fiber formation model. Each parameter was both increased and decreased by 20%. (a) Variation of initial concentration of fibrinogen f_{A_0} ($\frac{mg}{mL}$). (b) Variation of the minimum length for protofibrils to be capable of lateral aggregation $l_{agg} + 1$ (number of monomers). (c) Variation of the rate of fibrinopeptide A cleavage to convert fibrinogen to fibrin monomers k_A ($\frac{1}{s}$). (d) Variation of the rate of association of fibrin monomers to yield small oligomers and initiate protofibril formation k_{pi} ($\frac{L}{molecule \cdot s}$). (e) Variation of the rate of protofibril growth in length by association with oligomers k_{pg} ($\frac{L}{molecule \cdot s}$). (f) Variation of the rate of protofibril lateral aggregation to initiate a fiber k_{fi} ($\frac{L}{molecule \cdot s}$). (g) Variation of the rate of fiber growth in diameter by association with additional protofibrils k_{fg} ($\frac{L}{molecule \cdot s}$). (h) Variation of the rate of lateral aggregation of fibers k_{fA} ($\frac{L}{molecule \cdot s}$).

the limit. In contrast, Figure 2.4(g) shows that k_{fg} has the opposite effect: smaller values of k_{fg} yield smaller values of the limit. Finally, Figure 2.4(h) depicts that k_{fA} has a small affect on the slope of the asymptotic limit plateau region of m : larger values of k_{fA} result in larger slopes in the asymptotic limit plateau region of m .

2.2.2 Fiber Radius as a Function of Fibrin Polymerization Time

If the radius of the region occupied by a single protofibril is given as r_m , then the cross-sectional area occupied by a single protofibril is

$$a_0 = \pi r_m^2. \quad (2.40)$$

Similarly, if the radius of a fiber is R , then the cross-sectional area of a fiber is given by

$$A_{fiber} = \pi R^2. \quad (2.41)$$

Since the average number of protofibrils per fiber is given above as m ,

$$A_{fiber} = a_0 m, \quad (2.42)$$

which gives us

$$\pi R^2 = \pi r_m^2 m, \quad (2.43)$$

or

$$R(t) = r_m \sqrt{m(t)}. \quad (2.44)$$

This is similar to the expression derived in [100]. The polymerization parameters (see Section 2.2.1) which most directly control the plateau value of $R(t)$ are k_{fi} and k_{fg} .

2.3 Force in Helical Rods

Since it has been observed [53, 91] that both protofibrils and fibrin fibers are comprised of smaller units helically twisted around a central stem, the derivation for the force in a helical fiber is presented here.

A circular helix of radius r and pitch p with right-handed chirality can be described in lab-frame Cartesian coordinates as

$$\mathbf{r}(\zeta) = r \cos(\zeta)\mathbf{e}_1 + r \sin(\zeta)\mathbf{e}_2 + \left(\frac{p}{2\pi}\right)\zeta\mathbf{e}_3, \quad (2.45)$$

and we denote

$$\frac{1}{\eta} = \left| \frac{d\mathbf{r}(\zeta)}{d\zeta} \right| = \sqrt{r^2 + \left(\frac{p}{2\pi}\right)^2} \quad (2.46)$$

for simplicity. If $s(\zeta)$ is an arc-length coordinate along the contour of the helix, then

$$s(\zeta) = \int_0^\zeta \left| \frac{d\mathbf{r}(\sigma)}{d\sigma} \right| d\sigma = \frac{\zeta}{\eta}, \quad (2.47)$$

and the helix can be rewritten as

$$\mathbf{r}(s) = r \cos(\eta s)\mathbf{e}_1 + r \sin(\eta s)\mathbf{e}_2 + \left(\frac{p}{2\pi}\right)\eta s\mathbf{e}_3. \quad (2.48)$$

The tangent to the helix is given as

$$\hat{\mathbf{t}}(s) = \frac{d\mathbf{r}(s)}{ds} = -r\eta \sin(\eta s)\mathbf{e}_1 + r\eta \cos(\eta s)\mathbf{e}_2 + \left(\frac{p}{2\pi}\right)\eta\mathbf{e}_3, \quad (2.49)$$

which is clearly a unit vector since

$$|\hat{\mathbf{t}}(s)|^2 = \eta^2 \left(r^2 + \left(\frac{p}{2\pi}\right)^2 \right) = 1. \quad (2.50)$$

We can define the curvature

$$\kappa = \left| \frac{d\hat{\mathbf{t}}(s)}{ds} \right| = r\eta^2 \quad (2.51)$$

and unit normal vector

$$\hat{\boldsymbol{\nu}}(s) = \frac{1}{\kappa} \left(\frac{d\hat{\mathbf{t}}(s)}{ds} \right) = -\cos(\eta s)\mathbf{e}_1 - \sin(\eta s)\mathbf{e}_2 + 0\mathbf{e}_3, \quad (2.52)$$

from which we can also define the unit binormal vector

$$\hat{\boldsymbol{\beta}}(s) = \hat{\mathbf{t}}(s) \times \hat{\boldsymbol{\nu}}(s) = \left(\frac{p}{2\pi} \right) \eta \sin(\eta s)\mathbf{e}_1 - \left(\frac{p}{2\pi} \right) \eta \cos(\eta s)\mathbf{e}_2 + r\eta\mathbf{e}_3 \quad (2.53)$$

and right-handed torsion

$$\tau = (\hat{\mathbf{t}} \times \hat{\boldsymbol{\nu}}) \cdot \frac{d\hat{\boldsymbol{\nu}}}{ds} = \left(\frac{p}{2\pi} \right) \eta^2. \quad (2.54)$$

(Note that for a helix with left chirality, for example $\mathbf{r}(s) = r \sin(\eta s)\mathbf{e}_1 + r \cos(\eta s)\mathbf{e}_2 + \left(\frac{p}{2\pi} \right) \eta s\mathbf{e}_3$, the right-handed torsion is $\tau = -\left(\frac{p}{2\pi} \right) \eta^2$, but with the given definitions the difference has no other effect.) From here it is clear that

$$\kappa^2 + \tau^2 = \eta^2 \quad (2.55)$$

and thus

$$r = \frac{\kappa}{\kappa^2 + \tau^2} \quad (2.56)$$

$$\left(\frac{p}{2\pi} \right) = \frac{\tau}{\kappa^2 + \tau^2}. \quad (2.57)$$

It can be verified that the three vectors $\hat{\mathbf{t}}(s)$, $\hat{\boldsymbol{\nu}}(s)$, and $\hat{\boldsymbol{\beta}}(s)$ are orthonormal, and that the Frenet-Serret theorem

$$\frac{d}{ds} \begin{bmatrix} \hat{\mathbf{t}}(s) \\ \hat{\boldsymbol{\nu}}(s) \\ \hat{\boldsymbol{\beta}}(s) \end{bmatrix} = \begin{bmatrix} 0 & \kappa & 0 \\ -\kappa & 0 & \tau \\ 0 & -\tau & 0 \end{bmatrix} \begin{bmatrix} \hat{\mathbf{t}}(s) \\ \hat{\boldsymbol{\nu}}(s) \\ \hat{\boldsymbol{\beta}}(s) \end{bmatrix} \quad (2.58)$$

holds. As such, it is logical to express the lab-frame in the Frenet frame, using the transformations

$$\begin{bmatrix} \hat{\mathbf{t}}(s) \\ \hat{\boldsymbol{\nu}}(s) \\ \hat{\boldsymbol{\beta}}(s) \end{bmatrix} = \begin{bmatrix} -r\eta \sin(\eta s) & r\eta \cos(\eta s) & (\frac{p}{2\pi})\eta \\ -\cos(\eta s) & -\sin(\eta s) & 0 \\ (\frac{p}{2\pi})\eta \sin(\eta s) & -(\frac{p}{2\pi})\eta \cos(\eta s) & r\eta \end{bmatrix} \begin{bmatrix} \mathbf{e}_1 \\ \mathbf{e}_2 \\ \mathbf{e}_3 \end{bmatrix} \quad (2.59)$$

$$\begin{bmatrix} \mathbf{e}_1 \\ \mathbf{e}_2 \\ \mathbf{e}_3 \end{bmatrix} = \begin{bmatrix} -r\eta \sin(\eta s) & -\cos(\eta s) & (\frac{p}{2\pi})\eta \sin(\eta s) \\ r\eta \cos(\eta s) & -\sin(\eta s) & -(\frac{p}{2\pi})\eta \cos(\eta s) \\ (\frac{p}{2\pi})\eta & 0 & r\eta \end{bmatrix} \begin{bmatrix} \hat{\mathbf{t}}(s) \\ \hat{\boldsymbol{\nu}}(s) \\ \hat{\boldsymbol{\beta}}(s) \end{bmatrix}. \quad (2.60)$$

Having described the kinematics of a helical rod we now want to examine equilibria with curvature κ and torsion τ , both independent of s . It is assumed that the helical rod can carry forces and moments and that it is acted upon by body forces and body moments. The goal is to find the force and moment in the helical rod, given κ , τ , and the body forces and body moments. In the Frenet frame, the body force per unit length on the helix, assumed independent of position on the helix s , can be written

$$\mathbf{f} = f_t \hat{\mathbf{t}} + f_\nu \hat{\boldsymbol{\nu}} + f_\beta \hat{\boldsymbol{\beta}}, \quad (2.61)$$

and the force vector at any point s in the helix can be written

$$\mathbf{n}(s) = n_t \hat{\mathbf{t}} + n_\nu \hat{\boldsymbol{\nu}} + n_\beta \hat{\boldsymbol{\beta}}. \quad (2.62)$$

Conservation of linear momentum requires

$$\frac{d\mathbf{n}(s)}{ds} + \mathbf{f} = 0, \quad (2.63)$$

which, using the Frenet-Serret theorem Eq. (2.58), reduces to

$$\frac{dn_t}{ds} - n_\nu \kappa + f_t = 0 \quad (2.64)$$

$$\frac{dn_\nu}{ds} - n_\beta \tau + n_t \kappa + f_\nu = 0 \quad (2.65)$$

$$\frac{dn_\beta}{ds} + n_\nu \tau + f_\beta = 0. \quad (2.66)$$

Differentiating Eq. (2.65) with respect to s , and substituting in for $\frac{dn_t}{ds}$ from Eq. (2.64) and $\frac{dn_\beta}{ds}$ from Eq. (2.66), results in

$$\frac{d^2 n_\nu}{ds^2} + \eta^2 n_\nu + (\tau f_\beta - \kappa f_t) = 0, \quad (2.67)$$

which has solution

$$n_\nu(s) = A \cos(\eta s) + B \sin(\eta s) - \frac{1}{\eta^2} (\tau f_\beta - \kappa f_t), \quad (2.68)$$

where A and B are two constants. Putting Eq. (2.68) into Eq. (2.64) and Eq. (2.66), we have

$$\frac{dn_t}{ds} = A\kappa \cos(\eta s) + B\kappa \sin(\eta s) - \frac{\kappa}{\eta^2} (\tau f_\beta - \kappa f_t) - f_t \quad (2.69)$$

$$\frac{dn_\beta}{ds} = -A\tau \cos(\eta s) - B\tau \sin(\eta s) + \frac{\tau}{\eta^2} (\tau f_\beta - \kappa f_t) - f_\beta, \quad (2.70)$$

which can be integrated with respect to s to get

$$n_t = \frac{A\kappa}{\eta} \sin(\eta s) - \frac{B\kappa}{\eta} \cos(\eta s) - \frac{\kappa s}{\eta^2} (\tau f_\beta - \kappa f_t) - f_t s + D_t \quad (2.71)$$

$$n_\beta = -\frac{A\tau}{\eta} \sin(\eta s) + \frac{B\tau}{\eta} \cos(\eta s) + \frac{\tau s}{\eta^2} (\tau f_\beta - \kappa f_t) - f_\beta s + D_\beta, \quad (2.72)$$

where D_t and D_β are arbitrary constants. Substituting Eq. (2.71), Eq. (2.68), and Eq. (2.72) into Eq. (2.65) yields

$$f_\nu = \tau D_\beta - \kappa D_t. \quad (2.73)$$

It is useful to recast the force balance in the directors \mathbf{d}_i , $i = 1, 2, 3$ of a material frame in the reference configuration of the circular cross-section of the rod comprising the helix. This frame is a rotation by an angle

$$\phi(s) = (\kappa_3 - \tau) s \quad (2.74)$$

about the normal vector $\hat{\mathbf{t}}$, where κ_3 is a constant. In this frame,

$$\begin{bmatrix} \mathbf{d}_1(s) \\ \mathbf{d}_2(s) \\ \mathbf{d}_3(s) \end{bmatrix} = \begin{bmatrix} 0 & \cos \phi & \sin \phi \\ 0 & -\sin \phi & \cos \phi \\ 1 & 0 & 0 \end{bmatrix} \begin{bmatrix} \hat{\mathbf{t}}(s) \\ \hat{\boldsymbol{\nu}}(s) \\ \hat{\boldsymbol{\beta}}(s) \end{bmatrix}, \quad (2.75)$$

and

$$\begin{bmatrix} \hat{\mathbf{t}}(s) \\ \hat{\boldsymbol{\nu}}(s) \\ \hat{\boldsymbol{\beta}}(s) \end{bmatrix} = \begin{bmatrix} 0 & 0 & 1 \\ \cos \phi & -\sin \phi & 0 \\ \sin \phi & \cos \phi & 0 \end{bmatrix} \begin{bmatrix} \mathbf{d}_1(s) \\ \mathbf{d}_2(s) \\ \mathbf{d}_3(s) \end{bmatrix}. \quad (2.76)$$

The material frame also has the property

$$\frac{d\mathbf{d}_i}{ds} = \boldsymbol{\kappa} \times \mathbf{d}_i, \quad i = 1, 2, 3, \quad (2.77)$$

where the curvature vector can be represented

$$\boldsymbol{\kappa} = \kappa_1 \mathbf{d}_1 + \kappa_2 \mathbf{d}_2 + \kappa_3 \mathbf{d}_3, \quad (2.78)$$

or, in the Frenet frame, as

$$\boldsymbol{\kappa} = (\kappa_1 \cos \phi - \kappa_2 \sin \phi) \hat{\boldsymbol{\nu}} + (\kappa_1 \sin \phi + \kappa_2 \cos \phi) \hat{\boldsymbol{\beta}} + \kappa_3 \hat{\mathbf{t}} \quad (2.79)$$

$$= \kappa_3 \hat{\mathbf{t}} + \kappa \hat{\boldsymbol{\beta}}, \quad (2.80)$$

with

$$\kappa_1 = \kappa \sin((\kappa_3 - \tau) s) \quad (2.81)$$

$$\kappa_2 = \kappa \cos((\kappa_3 - \tau) s) \quad (2.82)$$

$$\kappa_3 = \text{constant}. \quad (2.83)$$

We next analyze the angular momentum. Conservation of angular momentum can be expressed

as

$$\frac{d\mathbf{m}}{ds} + \hat{\mathbf{t}} \times \mathbf{n} + \boldsymbol{\ell} = \mathbf{0}, \quad (2.84)$$

where \mathbf{m} is the moment at any point on the helix and $\boldsymbol{\ell}$ is a body moment per unit arc length. Following the example of Nizette and Goriely [101], to relate the moment \mathbf{m} and the curvature vector $\boldsymbol{\kappa}$, we use the constitutive relation from linear elasticity for a rod of circular cross section

$$\mathbf{m} = K_b (\kappa_1 - \kappa_{01}) \mathbf{d}_1 + K_b (\kappa_2 - \kappa_{02}) \mathbf{d}_2 + K_t (\kappa_3 - \kappa_{03}) \mathbf{d}_3, \quad (2.85)$$

where

$$K_b = E \frac{\pi r^4}{4} \quad (2.86)$$

is the bending modulus with E the Young's modulus of the rod,

$$K_t = G \frac{\pi r^4}{2} \quad (2.87)$$

is the twisting modulus with G the shear modulus of the rod, and

$$\kappa_{01} = \kappa_0 \sin((\kappa_3 - \tau)s), \quad (2.88)$$

$$\kappa_{02} = \kappa_0 \cos((\kappa_3 - \tau)s), \quad (2.89)$$

κ_{03} , and κ_0 are the spontaneous curvatures of the helix in the stress-free state. In the Frenet frame, the constitutive relation giving the moment \mathbf{m} can be written

$$\mathbf{m} = K_b (\kappa - \kappa_0) \hat{\boldsymbol{\beta}} + K_t (\kappa_3 - \kappa_{03}) \hat{\mathbf{t}}. \quad (2.90)$$

As in [101], we also take the body moment

$$\boldsymbol{\ell} = \mathbf{0}. \quad (2.91)$$

Now, the conservation of angular momentum reduces to the following three equations:

$$K_t \frac{d\kappa_3}{ds} = 0 \quad (2.92)$$

$$K_t (\kappa_3 - \kappa_{03}) \kappa - K_b (\kappa - \kappa_0) \tau - n_\beta = 0 \quad (2.93)$$

$$n_\nu = 0, \quad (2.94)$$

recalling that

$$\kappa = \frac{r}{r^2 + \left(\frac{p}{2\pi}\right)^2}, \quad (2.95)$$

$$\kappa_0 = \frac{r_0}{r_0^2 + \left(\frac{p_0}{2\pi}\right)^2}, \quad (2.96)$$

and κ_{03} are constants. Eq. (2.92) shows that κ_3 is constant, and Eq. (2.93) shows that

$$n_\beta = K_t (\kappa_3 - \kappa_{03}) \kappa - K_b (\kappa - \kappa_0) \tau, \quad (2.97)$$

which is therefore also a constant. Combining Eq. (2.94) with Eq. (2.68), we have

$$0 = A \cos(\eta s) + B \sin(\eta s) - \frac{1}{\eta^2} (\tau f_\beta - \kappa f_t) \forall s. \quad (2.98)$$

In order for this equation to be true for all s , we must conclude that

$$A = B = 0, \quad (2.99)$$

$$\tau f_\beta = \kappa f_t. \quad (2.100)$$

Using these conclusions, Eq. (2.71) and Eq. (2.72) become

$$n_t = D_t - f_t s \quad (2.101)$$

$$n_\beta = D_\beta - f_\beta s. \quad (2.102)$$

However, since we have also Eq. (2.97) independent of s , from the last equation we must conclude

also that

$$f_\beta = 0 \quad (2.103)$$

$$D_\beta = n_\beta = K_t (\kappa_3 - \kappa_{03}) \kappa - K_b (\kappa - \kappa_0) \tau. \quad (2.104)$$

Since we also have Eq. (2.100), if $f_\beta = 0$, we must also have

$$f_t = 0, \quad (2.105)$$

and therefore

$$n_t = D_t \quad (2.106)$$

is also a constant. Thus, we have

$$\mathbf{n} = D_t \hat{\mathbf{t}} + (K_t (\kappa_3 - \kappa_{03}) \kappa - K_b (\kappa - \kappa_0) \tau) \hat{\boldsymbol{\beta}} \quad (2.107)$$

$$\mathbf{f} = (K_t (\kappa_3 - \kappa_{03}) \kappa \tau - K_b (\kappa - \kappa_0) \tau^2 - \kappa D_t) \hat{\boldsymbol{\nu}}. \quad (2.108)$$

In the material frame, the body force per unit length on the helix can be written

$$\mathbf{f} = f_1 \mathbf{d}_1 + f_2 \mathbf{d}_2 + f_3 \mathbf{d}_3, \quad (2.109)$$

and the force vector at any point s in the helix can be written

$$\mathbf{n}(s) = n_1 \mathbf{d}_1 + n_2 \mathbf{d}_2 + n_3 \mathbf{d}_3. \quad (2.110)$$

From our previous analysis, we have

$$\mathbf{n} = \left(K_t (\kappa_3 - \kappa_{03}) - K_b (\kappa - \kappa_0) \frac{\tau}{\kappa} \right) (\kappa_1 \mathbf{d}_1 + \kappa_2 \mathbf{d}_2) + D_t \mathbf{d}_3 \quad (2.111)$$

$$\mathbf{f} = \left(K_t (\kappa_3 - \kappa_{03}) \tau - K_b (\kappa - \kappa_0) \frac{\tau^2}{\kappa} - D_t \right) (\kappa_2 \mathbf{d}_1 - \kappa_1 \mathbf{d}_2), \quad (2.112)$$

which gives us

$$n_1 = \left(K_t (\kappa_3 - \kappa_{03}) - K_b (\kappa - \kappa_0) \frac{\tau}{\kappa} \right) \kappa_1 \quad (2.113)$$

$$n_2 = \left(K_t (\kappa_3 - \kappa_{03}) - K_b (\kappa - \kappa_0) \frac{\tau}{\kappa} \right) \kappa_2 \quad (2.114)$$

$$n_3 = D_t \quad (2.115)$$

$$f_1 = \left(K_t (\kappa_3 - \kappa_{03}) \tau - K_b (\kappa - \kappa_0) \frac{\tau^2}{\kappa} - D_t \right) \kappa_2 \quad (2.116)$$

$$f_2 = - \left(K_t (\kappa_3 - \kappa_{03}) \tau - K_b (\kappa - \kappa_0) \frac{\tau^2}{\kappa} - D_t \right) \kappa_1 \quad (2.117)$$

$$f_3 = 0. \quad (2.118)$$

Suppose there is a force $\mathbf{F} = F\mathbf{e}_3$ applied on the helical filament along its axis. This applied force in the Frenet frame can be expressed

$$\mathbf{F} = F\mathbf{e}_3 = F \left(\left(\frac{p}{2\pi} \right) \eta \hat{\mathbf{t}} + r\eta \hat{\boldsymbol{\beta}} \right). \quad (2.119)$$

The filament will carry the force as the force vector $\mathbf{n} = \mathbf{F}$. Thus, in the Frenet frame, we have

$$D_t = F \left(\frac{p}{2\pi} \right) \eta \quad (2.120)$$

$$K_t (\kappa_3 - \kappa_{03}) \kappa - K_b (\kappa - \kappa_0) \tau = Fr\eta. \quad (2.121)$$

Solving the second of these two equations for F and substituting back into the first, we arrive at

$$D_t = \left(K_t (\kappa_3 - \kappa_{03}) - K_b (\kappa - \kappa_0) \frac{\tau}{\kappa} \right) \tau. \quad (2.122)$$

Thus, the body force per unit length on the helix and the force vector at any point s on the helix become

$$\mathbf{f} = \mathbf{0} \quad (2.123)$$

$$\mathbf{n} = \left(K_t (\kappa_3 - \kappa_{03}) - K_b (\kappa - \kappa_0) \frac{\tau}{\kappa} \right) (\kappa_1 \mathbf{d}_1 + \kappa_2 \mathbf{d}_2 + \tau \mathbf{d}_3). \quad (2.124)$$

In the case when $\kappa_0 = \kappa_{03} = 0$, the force vector

$$\frac{\mathbf{n}}{K_b} = \left(\frac{K_t}{K_b} \kappa_3 - \tau \right) [\boldsymbol{\kappa} - (\kappa_3 - \tau) \mathbf{d}_3] \quad (2.125)$$

from Nizette and Goriely [101] is recovered.

The magnitude of the force vector is

$$n = \left| \left(K_t (\kappa_3 - \kappa_{03}) - K_b (\kappa - \kappa_0) \frac{\tau}{\kappa} \right) \right| \eta. \quad (2.126)$$

In the main text we assume there is no twisting moment acting on the helix, so $K_t (\kappa_3 - \kappa_{03}) = 0$.

2.3.1 Tensile Force in a Fiber

It has been observed [53, 91] that protofibrils and fibrin fibers are comprised of smaller longitudinal units helically twisted around a central stem. Thus, the theory developed in 2.3 is applicable to the components of both fibrin fibers and protofibrils. For a helix of radius r and pitch p , the pitch angle is given by

$$\tan \alpha = \left| \frac{\tau}{\kappa} \right| = \frac{p}{2\pi r} \quad (2.127)$$

where τ is the torsion of and κ is the curvature of the helical curve. Additionally, since the adjacent helical protofibrils must maintain registry required for the $22.5nm$ half-staggered longitudinal band pattern [52, 53, 98], the pitch angle must remain constant through the cross-section of the fiber at different values of the radius r . As r evolves in time the pitch angle also evolves. For example, the pitch angle $\alpha = 80.8^\circ$ calculated from the measured quantities $r = 50nm$ and $p = 1930nm$ for fibrin fibers [53]. The pitch angle $\alpha = 85.5^\circ$ calculated from the extracted quantities $r = 5nm$ and $p = 400nm$ from simulations of equilibrated molecular structures [91]. Assuming also that there is no twisting moment, so that $\kappa_3 = \kappa_{03}$, the magnitude of the force in a protofibril can be written as (see 2.3)

$$n(r) = \left| -K_b \sin \alpha \frac{1}{r} \left(\frac{\cos^2 \alpha}{r} - \kappa_0 \right) \right|, \quad (2.128)$$

where K_b is a bending modulus and κ_0 is a spontaneous curvature, both material properties of the helical protofibrils. In a tension-free state with pitch angle α_s (for example, in a hypothetical free-floating twisted but unstretched fiber) the total force on the fiber is $F = 0$. Since the radial distribution of protofibrils is disordered [53], the number density of protofibrils per unit cross-sectional area is assumed to be constant and the fiber cross-section is taken as being circular of radius R . Then, the force balance in the tension-free fiber cross-section is

$$\int_{r_m}^R \frac{2\pi r}{a_0} n(r) dr = 0, \quad (2.129)$$

where again

$$a_0 = \pi r_m^2 \quad (2.130)$$

is the area occupied by one protofibril. Since K_b , a_0 , and α_s are constant, the integral simplifies to

$$\int_{r_m}^R \frac{\cos^2 \alpha_s}{r} dr = \int_{r_m}^R \kappa_0 dr, \quad (2.131)$$

which gives

$$\cos^2 \alpha_s = \frac{\kappa_0 (R - r_m)}{\ln \left(\frac{R}{r_m} \right)}. \quad (2.132)$$

This sets the pitch angle of the fiber as a function of the radius R in a stress-free state.

For a fiber of pitch angle $\alpha_e \neq \alpha_s$ both twisted and stretched to connect to a network, the total force on the fiber is $F \neq 0$. In this case, the force balance for the cross-section of a fiber under tension is

$$\int_{r_m}^R \frac{2\pi r}{a_0} n(r) dr = F. \quad (2.133)$$

This time, the solution of the integral for the force on the fiber is

$$F = \frac{2\pi}{a_0} K_b \sin \alpha_e \left(\kappa_0 (R - r_m) - \cos^2 \alpha_e \ln \left(\frac{R}{r_m} \right) \right). \quad (2.134)$$

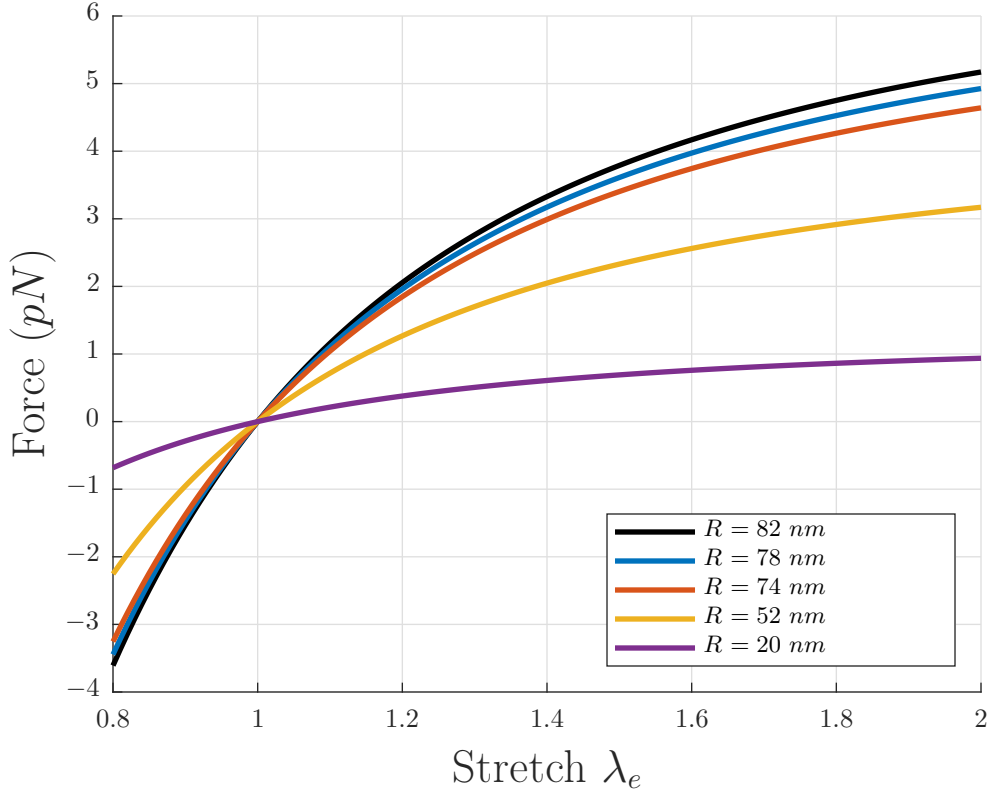


Figure 2.5: Tensile force F vs. stretch λ_e in an individual fiber for different fiber radii. Thicker fibers develop higher tensile forces.

If we define

$$\lambda_e = \frac{\tan \alpha_e}{\tan \alpha_s} \quad (2.135)$$

as the elastic stretch of the fiber between the twisted but unstretched state with pitch angle α_s and the twisted and stretched state with pitch angle α_e , then the force on the fiber Eq. (2.134) can be considered as a function of λ_e and $\alpha_s(R)$, where $\alpha_s(R)$ is known from Eq. (2.132), and $R(t)$ from Eq. (2.44) can be calculated from the fiber polymerization equations in Section 2.2.1. The result from Eq. (2.134) for different values of R , in line with previously reported range of fibrin fiber radii of 25–115nm [69], are shown in Figure 2.5 for parameter values discussed below. Note that $F = 0$ at $\lambda_e = 1$ for all values of R . This will be useful when we define a stress-free intermediate configuration in the continuum model (see Section 2.3.3).

The parameters in Eq. (2.134) are as follows: $a_0 = \pi r_m^2$, the area of a circular region of radius r_m

occupied by one protofibril (plus surrounding fluid); K_b , the bending modulus of the fiber; λ_e , the stretch of the fiber between the twisted but unstretched state with pitch angle α_s and the twisted and stretched state with pitch angle α_e ; and κ_0 , the spontaneous curvature in the stress-free state. The radius of the area occupied by a single protofibril is known to be $r_m = 6.5nm$ [88, 91, 102]. With an estimate of the persistence length of protofibrils of $L_p = 400nm$ [91] and a room temperature of $T = 290K$, the bending modulus can be estimated as $K_b = k_B T L_p \approx 1600pN nm^2$, where k_B is the Boltzmann constant. κ_0 can be estimated in two ways: the first way utilizes the relationship between curvature and the radius and pitch of a helix Eq. (2.96), and the extracted quantities $r_0 = 5nm$ and $p_0 = 400nm$ from simulations of equilibrated molecular structures of free protofibrils [91], which gives a value $\kappa_0 \approx 1.226 \times 10^{-3}nm^{-1}$; the second way rearranges Eq. (2.132), uses $\tan \alpha_s = \frac{p}{2\pi R}$, and takes the average value of κ_0 for the values of $R = 50nm$ and the range $p = 1930 \pm 280nm$ from [53], which gives a value $\langle \kappa_0 \rangle \approx 1.235 \times 10^{-3}nm^{-1}$. These two estimates are in excellent agreement, so the value $\kappa_0 = 1.23 \times 10^{-3}nm^{-1}$ is chosen.

Using these values, the tensile force F in a fiber vs time t in polymerization can be seen in Figure 2.6 with $\lambda_e = 1.501$ held fixed.

2.3.2 Kinematics of Fiber Relaxation After Transverse Cutting

According to the theory presented in Section 2.3.1, a fiber of length l in a network will relax to an equilibrium length l/λ_e when cut transversely. This assertion can be confirmed by solving for the length of a fiber over time as it relaxes. Here, the fiber will be modeled as a rod relaxing through a fluid. Similar to [103], the kinematics over time t are developed for a rod-like structure of length l in one spatial dimension characterized by the reference configuration variable ς . All relevant vectors have the same direction along the length of the fiber from $\varsigma = 0$ to l , so they will be treated as scalars with unit vector direction along the length of the fiber. The fiber is assumed to be moving in a fluid, which itself is flowing with velocity v , which causes a drag force. Thus, the spatial position of a material point ς at time t is $z(t, \varsigma)$, the velocity of the spatial point is $\frac{\partial z}{\partial t}$, and the stretch

$$\lambda = \left| \frac{\partial z}{\partial \varsigma} \right| = \frac{\tan \alpha}{\tan \alpha_e} \quad (2.136)$$

depends on both position and time. Here $\alpha(\varsigma, t)$ is the current pitch angle and we have chosen the reference state to be the one with uniform stretch λ_e everywhere. The balance of linear momentum

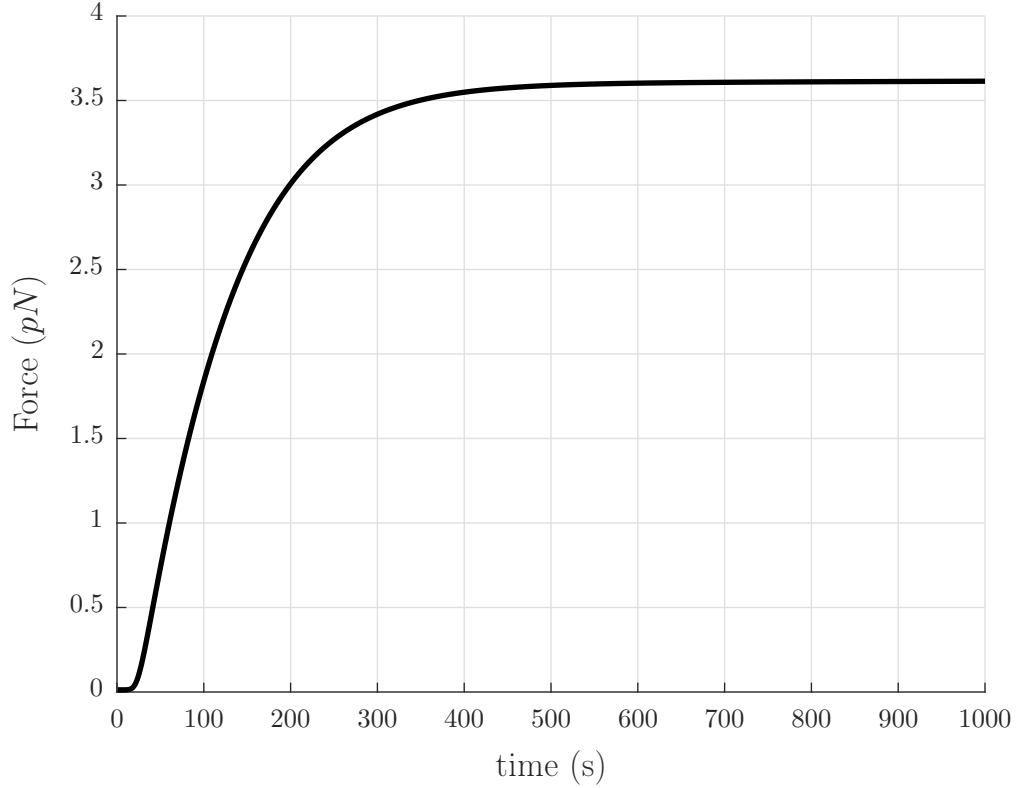


Figure 2.6: Tensile force F in individual fibers vs time t in polymerization for the values $r_m = 6.5nm$, $K_b = 1600pN nm^2$, $\lambda_e = 1.501$, and $\kappa_0 = 1.23 \times 10^{-3}nm^{-1}$.

for a segment of the fiber in this reference configuration can be written

$$\frac{d}{dt} \int_{\varsigma_1}^{\varsigma_2} \rho \frac{\partial z}{\partial t} d\varsigma = F(t, \varsigma_2) - F(t, \varsigma_1) + \int_{\varsigma_1}^{\varsigma_2} b(t, \varsigma) d\varsigma, \quad (2.137)$$

where the linear density ρ is mass per unit length of the fiber, $F = F(t, \varsigma)$ is the force at time t acting on material point ς , and $b = b(t, \varsigma)$ is a distributed load per unit length at ς . Here, the inertia force is negligible, so $\rho = 0$. The distributed body force

$$b(t, \varsigma) = -d_w \left(\frac{\partial z(t, \varsigma)}{\partial t} - v \right) \quad (2.138)$$

where d_w is the effective drag coefficient caused by the drag force exerted on the fiber by the surrounding fluid. The effective drag coefficient d_w is estimated using results proposed by [104] for thin bodies in flow with low Reynolds' number. These results take advantage of thinness to

make simplifications to approximate solutions for the flow around these bodies, and superimpose fundamental singularities around the body to solve for complex flows. Exact solutions can be obtained for mathematically simple bodies in mathematically simple flows. Their expression for the axial drag coefficient is

$$d_w = \frac{2\pi\mu}{\ln\left(\frac{l}{R}\right) + c}, \quad (2.139)$$

where μ is the fluid viscosity, l is the length of the body, R is the radius of gyration of the body, and c depends on the shape of the body. For a uniform cylinder,

$$c = \ln 2 - \frac{3}{2}. \quad (2.140)$$

As such, the linear momentum equation becomes

$$F(t, \varsigma_2) - F(t, \varsigma_1) - \int_{\varsigma_1}^{\varsigma_2} d_w \left(\frac{\partial z(t, \varsigma)}{\partial t} - v \right) d\varsigma, \quad (2.141)$$

which can be localized to

$$\frac{\partial F(t, \varsigma)}{\partial \varsigma} = d_w \left(\frac{\partial z(t, \varsigma)}{\partial t} - v \right) \quad (2.142)$$

since there are no discontinuities. In this case, the fluid is not flowing, so $v = 0$. Therefore, the localized balance of linear momentum becomes

$$\frac{\partial F(t, \varsigma)}{\partial \varsigma} = d_w \left(\frac{\partial z(t, \varsigma)}{\partial t} \right). \quad (2.143)$$

We take the constitutive law for the force F to be the same as in Eq. (2.134),

$$F(t, \varsigma) = \frac{2\pi}{a_0} K_b \sin \alpha \left(\kappa_0(R - r_m) - \ln \left(\frac{R}{r_m} \right) \cos^2 \alpha \right), \quad (2.144)$$

with

$$\tan \alpha = \frac{\partial z}{\partial \varsigma} \tan \alpha_e. \quad (2.145)$$

For the fiber in question, one end is assumed fixed and the free end has no force. Therefore, the boundary conditions are

$$z(t, \varsigma = 0) = 0, \quad (2.146)$$

$$F(t, \varsigma = l) = 0. \quad (2.147)$$

The initial condition at time $t = 0+$ is that $z(\varsigma) = \varsigma$ everywhere except very close to the end which is severed. At the severed end the tension instantaneously goes to zero. Since we integrate the PDE for the relaxation numerically by a finite difference method we give the initial condition in discrete form as:

$$z(t = 0, \varsigma) = \begin{cases} \varsigma, & 0 \leq \varsigma \leq 0.99l, \\ \frac{\tan \alpha_s}{\tan \alpha_e} (\varsigma - 0.99l) + 0.99l, & 0.99l < \varsigma \leq l, \end{cases} \quad (2.148)$$

where the last (100^{th}) element is assumed to be at zero force.

Eq. (2.143) can be solved using a finite difference method. Eq. (2.143) is discretized for numerical calculation as

$$\frac{F_{i,j+\frac{1}{2}} - F_{i,j-\frac{1}{2}}}{\Delta \varsigma} = d_w \frac{z_{i+1,j} - z_{i,j}}{\Delta t}, \quad (2.149)$$

where j denotes the j th node and i denotes the i th time step, $\Delta \varsigma$ is the element length, and Δt is the time step. From this, the position of the fiber at the next time increment can be calculated by

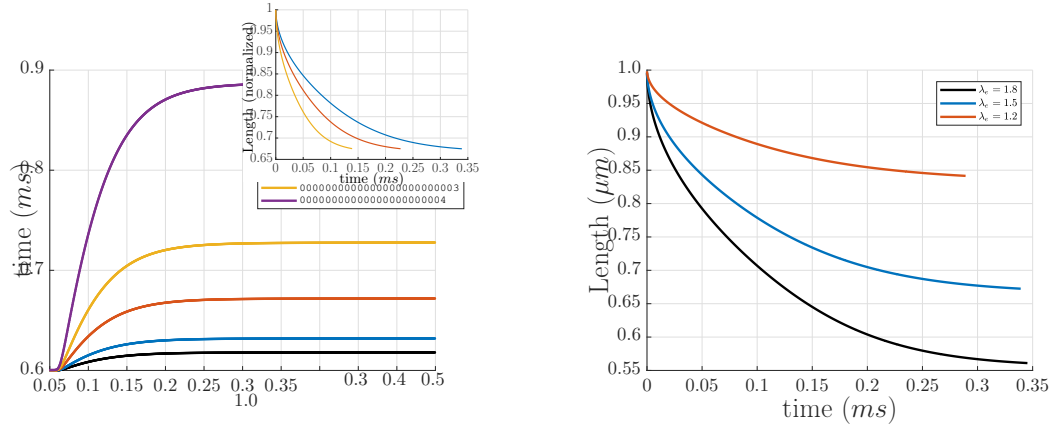
$$z_{i+1,j} = \frac{F_{i,j+\frac{1}{2}} - F_{i,j-\frac{1}{2}}}{\Delta \varsigma} \frac{\Delta t}{d_w} + z_{i,j}. \quad (2.150)$$

The condition

$$\Delta t \leq \frac{d_w}{2k_a} (\Delta \varsigma)^2, \quad (2.151)$$

with the largest slope of the force-stretch relation curve

$$k_a = \frac{2\pi}{a_0} K_b \tan \alpha_e \cos^3 \alpha_s \left(\kappa_0 (R - r_m) + (1 + \sin^2 \alpha_s) \ln \left(\frac{R}{r_m} \right) \right), \quad (2.152)$$



(a) Length $z(t, \zeta = l)$ of the fiber relaxing over time t for different initial lengths l values. Inset: normalized length $\frac{z(t, \zeta = l)}{z(t=0, \zeta = l)}$ over time t for the same l values.

(b) Length $z(t, \zeta = l)$ of the fiber relaxing over time t for different stretch λ_e values.

Figure 2.7: Length $z(t, \zeta = l)$ of the fiber relaxing over time t for different initial lengths l and different stretch λ_e values. (a) Length $z(t, \zeta = l)$ of the fiber relaxing over time t , with $R = 78nm$, $\tan \alpha_s = 5.22$, $\tan \alpha_e = 7.84$, $\lambda_e = 1.501$, and the initial length values $l = 0.5\mu m$, $l = 0.75\mu m$, and $l = 1.0\mu m$. Inset: the same curves with y -axis normalized by the initial lengths of the fibers $z(t = 0, \zeta = l)$. For $\lambda_e = 1.501$, the fibers relax to the lengths $0.34\mu m$, $0.50\mu m$, and $0.67\mu m$, respectively, from Eq. (2.143), in excellent agreement with the lengths $l/\lambda_e = 0.33\mu m$, $l/\lambda_e = 0.50\mu m$, and $l/\lambda_e = 0.67\mu m$ from the theory proposed in Section 2.3.1. (b) Length $z(t, \zeta = l)$ of the fiber relaxing over time t for different stretch λ_e values, with $R = 78nm$, $\tan \alpha_s = 5.22$, $l = 1.0\mu m$, and the stretch and pitch angle values $\lambda_e = 1.2$ and $\tan \alpha_e = 6.27$, $\lambda_e = 1.501$ and $\tan \alpha_e = 7.84$, and $\lambda_e = 1.8$ and $\tan \alpha_e = 9.40$.

must be satisfied to ensure stability of the method.

The inputs to this partial differential equation are as follows: the fiber radius, R ; the pitch angle of the fiber in the stress-free state, α_s ; the pitch angle of the fiber in the state in which it is twisted, stretched, and connected to the network, α_e ; the fluid viscosity, μ ; and the length of the fiber l when it is connected to the network. The fiber radius R is chosen from the final value calculated from the polymerization over time t , Eq. (2.44), which is in line with the previously reported range of fibrin fiber radii of $25 - 115nm$ [69]. The pitch angle in the stress-free state α_s is calculated as in Eq. (2.132), and the pitch angle of the fiber α_e in its connected state is computed from Eq. (2.135) with the fixed value $\lambda_e = 1.501$ used above in Section 2.3.1. Since the fluid in which the rod resides predominantly behaves like water, $\mu = 1.002 \times 10^{-3} Pa \cdot s$, the fluid viscosity of water. The probability density function of the fiber lengths $P(l)$ in a network is a log-normal distribution function of l with parameters $\mu = 0.53$ and $\sigma = 0.78$, as found in [105]. The most probable value is $l = 0.9\mu m$, with a likely range of about $0.5\mu m \leq l \leq 2\mu m$ (see also 2.4). Figure 2.7 depicts the length $z(t, \zeta = l)$

$z(t = 0, \varsigma = l) = l$	t_f	$z(t = t_f, \varsigma = l)$	$\frac{l}{\lambda_e}$	$L = \frac{l}{\lambda_e \lambda_s}$
$0.5\mu m$	$0.12ms$	$0.34\mu m$	$0.33\mu m$	$0.81\mu m$
$0.75\mu m$	$0.23ms$	$0.50\mu m$	$0.50\mu m$	$1.22\mu m$
$1.0\mu m$	$0.34ms$	$0.67\mu m$	$0.67\mu m$	$1.62\mu m$
$1.5\mu m$	$0.62ms$	$1.01\mu m$	$1.00\mu m$	$2.44\mu m$
$2.0\mu m$	$0.98ms$	$1.35\mu m$	$1.33\mu m$	$3.25\mu m$

Table 2.1: Relaxation times t_f and lengths, both calculated from Eq. (2.143) and from l/λ_e from the theory proposed in Section 2.3.1, for different initial lengths $z(t = 0, \varsigma = l) = l$. Relaxation time t_f was taken as the amount of time required to reach the expected length $l/\lambda_e \pm 1\%$ from the theory proposed in Section 2.3.1.

of the fiber relaxing over time t , with $R = 78nm$, $\tan \alpha_s = 5.22$, $\tan \alpha_e = 7.84$, $\lambda_e = 1.501$, and $l = 0.5\mu m$. For $\lambda_e = 1.501$, the fiber relaxes to the length $0.34\mu m$ in time $t_f = 0.12ms$ from Eq. (2.143), in excellent agreement with the length $l/\lambda_e = 0.33\mu m$ from the theory proposed in Section 2.3.1. Relaxation time t_f was taken as the amount of time required to reach the expected length $l/\lambda_e \pm 1\%$ from the theory proposed in Section 2.3.1. Relaxation times and lengths, both calculated from Eq. (2.143) and from l/λ_e from the theory proposed in Section 2.3.1, for different initial lengths l are presented in table Table 2.1.

Studies such as [106] (specifically as interpreted by [60]) demonstrate that fibrin fibers recoil in a timescale on the order of milliseconds or even submilliseconds. The relaxation times t_f given by the theory developed here agree with the millisecond and submillisecond recoil times presented by [106]. Additionally, recent works of Cone, et al. [60] have also measured lengths of individual fibers from fibrin networks prior to cleavage and the subsequent fragments, and calculated the average prestrain value as $\langle \varepsilon \rangle = 23 \pm 11\%$. The prestrain from the model presented here can be calculated as

$$\varepsilon = 1 - \frac{1}{\lambda_e}. \quad (2.153)$$

With the value of $\lambda_e = 1.501$ calculated from the mechanisms in Section 2.3.3, the prestrain is $\varepsilon = 33\%$. This value is in excellent agreement with the prestrain measured by Cone et al. [60]. This suggests that our assumption that $\lambda_e \approx 1.5$ is reasonable.

2.3.3 Continuum Model of Fibrin Gel

Consider a hypothetical free fibrin fiber polymerizing in space, beginning as a string of length L of protofibrils in this initial configuration. As it is not attached to any other fibers, such an imaginary fiber would not be constrained by outside agents (note that an actual fibrin fiber would polymerize

attached to other fibers in a network and would thus be under tension). As polymerization of this imaginary fiber proceeds, protofibrils aggregate laterally around the initial protofibril. If the fiber is not constrained in any way, the length of the fiber will decrease as the radius increases, as outer protofibrils stretch and protofibrils near the center contract in order for the protofibrils to maintain registry required for the $22.5nm$ half-staggered pattern [52, 53, 90, 98]. Let us assume that the stretch of this fiber (with respect to the initial configuration of length L) is

$$\lambda_s(t) \leq 1, \tag{2.154}$$

where t is the elapsed time since the start of polymerization (see Section 2.2.1). If there was an unconstrained isotropic network of such fibers which we describe as a continuum then this network will shrink compared to its configuration at $t = 0$ and the deformation gradient will be given by:

$$\mathbf{F}_s(t) = \lambda_s(t)\mathbf{I}. \tag{2.155}$$

Following the framework developed in [97] we will call this state of the continuum as an intermediate stress-free configuration. In this state, the length of the fibers is $\lambda_s L$, and the fibers are twisted helically but are not under tension. Imagine next that the network was actually formed between two rheometer plates whose normals are in the z -direction. If the distance between the plates is not allowed to change then the network is constrained and it will pull on the plates as the fiber diameter increases. Accordingly, there is a force along the \mathbf{e}_z direction, and there are zero forces in the \mathbf{e}_x and \mathbf{e}_y directions. Thus, due to this constraint, the fibers will be in a twisted and stretched state and the continuum representing the network has stretches $\lambda_{ex}(t)$, $\lambda_{ey}(t)$, and $\lambda_{ez}(t)$ measured with respect to the intermediate state, giving a deformation gradient

$$\mathbf{F}_e(t) = \frac{\partial \mathbf{x}_e}{\partial \mathbf{x}_s}, \tag{2.156}$$

where \mathbf{x}_e is the position in the fully deformed configuration of a particle whose position in the intermediate configuration is \mathbf{x}_s , and the elastic right Cauchy-Green tensor is

$$\mathbf{C}_e = \mathbf{F}_e^T \mathbf{F}_e = \begin{bmatrix} \lambda_{ex}^2 & 0 & 0 \\ 0 & \lambda_{ey}^2 & 0 \\ 0 & 0 & \lambda_{ez}^2 \end{bmatrix}. \quad (2.157)$$

The total deformation gradient is then

$$\mathbf{F}(t) = \mathbf{F}_e(t) \mathbf{F}_s(t). \quad (2.158)$$

Next, we need to give an expression for the stored energy density in the continuum as a function of \mathbf{F} . To this end, we will use the 8-chain model proposed in [41, 49, 107]. This model was shown to describe fibrin networks [50, 51], rubbers and elastomers [41, 107], actin filament networks [100], and other random networks. In [50] the stored energy density had two parts – (a) due to the deformation of the fibrin fibers, for which we use the Arruda-Boyce 8-chain model [41], and (b) due to volumetric deformation that the 8-chain model cannot capture for which we use a bulk-modulus. In the 8-chain model, the network is represented by a cube of length a in the reference (undeformed) configuration with eight fibers (or chains) of length

$$L = \frac{\sqrt{3}}{2} a \quad (2.159)$$

connecting each of the vertices to the center of the cube (see Figure 2.8). If the sides of the cube are parallel to the principal coordinates of the deformation, then after the deformation the length of each fiber is $\lambda_e(t) \lambda_s(t) L$, where

$$\lambda_e = \sqrt{\frac{\lambda_{ex}^2 + \lambda_{ey}^2 + \lambda_{ez}^2}{3}}. \quad (2.160)$$

If the strain energy per unit reference length of the fiber in the intermediate configuration due to the elastic deformation is $G(\lambda_e)$, then the stored energy in each fiber is $G(\lambda_e) \lambda_s L$, and the force-extension relation of a fiber is

$$F(\lambda_e) = \frac{dG(\lambda_e)}{d\lambda_e}. \quad (2.161)$$

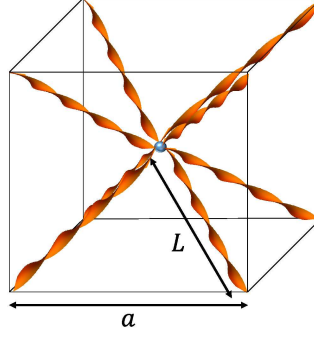


Figure 2.8: Cartoon depicting the 8-chain model representing fibrous network materials. A node in the center of an imaginary cube of initial side length a is connected to the eight vertices by eight chains, each of initial length $L = \frac{\sqrt{3}}{2}a$.

The contribution of fiber deformation to the total strain energy per unit volume is $\frac{\nu}{\lambda_s^3} \lambda_s LG(\lambda_e)$, where

$$\nu = \nu_{nd} = \frac{3\sqrt{3}}{L^3} \quad (2.162)$$

is the density of fibers in the reference configuration. Next, we need to account for the energy of volumetric deformation that is not captured by the 8-chain model. If the volume of the cube in the intermediate configuration is V_s and the volume change of the cube to the final configuration is ΔV , then

$$\frac{\Delta V}{V_s} = \lambda_{ex} \lambda_{ey} \lambda_{ez} - 1. \quad (2.163)$$

The strain energy per unit intermediate volume due to this volumetric deformation is denoted as $g(\lambda_{ex} \lambda_{ey} \lambda_{ez})$. Thus, the strain energy density per unit volume of the cube in the intermediate configuration is given by

$$U_e(\lambda_{ex}, \lambda_{ey}, \lambda_{ez}) = \frac{\nu}{\lambda_s^3} \lambda_s LG(\lambda_e) + g(\lambda_{ex} \lambda_{ey} \lambda_{ez}). \quad (2.164)$$

By observing that the strain energy density in the reference configuration U is related to the strain energy density in the intermediate configuration by

$$U = \lambda_s^3 U_e, \quad (2.165)$$

the strain energy density in the intermediate configuration can be converted into the strain energy density in the reference configuration as

$$U(\lambda_{ex}, \lambda_{ey}, \lambda_{ez}, \lambda_s) = \nu\lambda_s LG(\lambda_e) + \lambda_s^3 g(\lambda_{ex}\lambda_{ey}\lambda_{ez}). \quad (2.166)$$

Having described the kinematics and energetics of the continuum in this way we now want to enforce equilibrium. A comprehensive continuum mechanical theory to do this exercise for gels is given in [97]. We refer the reader to [97] for detailed derivations of the equations used below. Similar to the analyses in [97], the second Piola-Kirchoff stress can be written

$$\mathbf{T}_e = 2\mathbf{F}_e \frac{\partial U}{\partial \mathbf{C}_e} \quad (2.167)$$

$$\mathbf{T}_R = 2\mathbf{F}_e \frac{\partial U}{\partial \mathbf{C}_e} \mathbf{F}_s^{-T}, \quad (2.168)$$

where \mathbf{T}_R is the reference Piola-Kirchoff stress that satisfies the equilibrium equation

$$\text{Div } \mathbf{T}_R = 0 \quad (2.169)$$

in the reference configuration. Using our expression for the stored energy function we get,

$$\mathbf{T}_e = \frac{\nu\lambda_s L}{3\lambda_e} \begin{bmatrix} \lambda_{ex} & 0 & 0 \\ 0 & \lambda_{ey} & 0 \\ 0 & 0 & \lambda_{ez} \end{bmatrix} F(\lambda_e) + \lambda_s^3 f(\lambda_{ex}\lambda_{ey}\lambda_{ez}) \begin{bmatrix} \frac{1}{\lambda_{ex}} & 0 & 0 \\ 0 & \frac{1}{\lambda_{ey}} & 0 \\ 0 & 0 & \frac{1}{\lambda_{ez}} \end{bmatrix} \lambda_{ex}\lambda_{ey}\lambda_{ez} \quad (2.170)$$

$$\mathbf{T}_R = \frac{\nu L}{3\lambda_e} \begin{bmatrix} \lambda_{ex} & 0 & 0 \\ 0 & \lambda_{ey} & 0 \\ 0 & 0 & \lambda_{ez} \end{bmatrix} F(\lambda_e) + \lambda_s^2 f(\lambda_{ex}\lambda_{ey}\lambda_{ez}) \begin{bmatrix} \frac{1}{\lambda_{ex}} & 0 & 0 \\ 0 & \frac{1}{\lambda_{ey}} & 0 \\ 0 & 0 & \frac{1}{\lambda_{ez}} \end{bmatrix} \lambda_{ex}\lambda_{ey}\lambda_{ez}. \quad (2.171)$$

where $f(\frac{\Delta V}{V_s}) = g'(\frac{\Delta V}{V_s})$. It should be noted that the shear components of \mathbf{T}_e and \mathbf{T}_R are all 0 in principal coordinates. Since there are no forces or constraints applied on the fibers in the intermediate configuration, it is reasonable to assume $F(1) = f(1) = 0$.

In the present case with a network polymerizing in between fixed rheometer plates with surfaces

perpendicular to the axial \mathbf{e}_z direction, forces are applied only in the axial \mathbf{e}_z direction, and

$$T_{Rxx} = T_{Ryy} = 0. \quad (2.172)$$

Due to isotropy,

$$\lambda_{ex} = \lambda_{ey} = \lambda_* \quad (2.173)$$

are also expected, and so

$$\lambda_x = \lambda_y = \lambda_* \lambda_s \quad (2.174)$$

$$\lambda_z = \lambda_{ez} \lambda_s. \quad (2.175)$$

Since during polymerization the rheometer plates are fixed,

$$\lambda_z = 1. \quad (2.176)$$

Hence,

$$\lambda_{ez} = \frac{1}{\lambda_s}. \quad (2.177)$$

As such, equilibrium in terms of the Piola-Kirchoff stresses reduce to the following two equations:

$$0 = \frac{\nu L}{3\lambda_e} \lambda_* F(\lambda_e) + \lambda_s \lambda_* f \left(\frac{\lambda_*^2}{\lambda_s} \right) \quad (2.178)$$

$$T_{Rzz} = \frac{\nu L}{3\lambda_e \lambda_s} F(\lambda_e) + \lambda_s^2 \lambda_*^2 f \left(\frac{\lambda_*^2}{\lambda_s} \right), \quad (2.179)$$

for the two unknowns λ_* and T_{Rzz} , where now

$$\lambda_e = \sqrt{\frac{2\lambda_*^2 \lambda_s^2 + 1}{3\lambda_s^2}}. \quad (2.180)$$

The network stress T_{Rzz} can be multiplied by the area of the rheometer plate to get the force exerted on the network due to polymerization.

The unknowns in this model are as follows: L , the length of the fiber in the imaginary refer-

ence configuration; $F(\lambda_e)$, the force-stretch relation of a fiber; f , the relationship between volumetric strain and pressure; λ_s , the stretch between the imaginary reference configuration and the intermediate configuration; λ_* , the stretches between the intermediate configuration and the final configuration in the directions other than that in the axial \mathbf{e}_z direction; and, in the fixed solid volume fraction formulation, the solid volume fraction ϕ_s . The length of the fiber L in the imaginary reference configuration can be found by calculating

$$L = \frac{l}{\lambda_e \lambda_s}, \quad (2.181)$$

from the distribution found in [105], as discussed in Section 2.3.2. The force-stretch relation of a fiber $F(\lambda_e)$ is the same as the force in a fiber Eq. (2.134) derived in Section 2.3.1. The relationship between volumetric strain and pressure is taken to be

$$f\left(\frac{\lambda_*^2}{\lambda_s}\right) = K\left(\frac{\lambda_*^2}{\lambda_s} - 1\right), \quad (2.182)$$

where $K = 1314.67Pa$ is a bulk modulus as found in [2]. We have verified that a higher bulk modulus value of $K = 100KPa$ has little effect on the results. The stretch between the imaginary reference configuration and the intermediate configuration is taken to be

$$\lambda_s(R(t)) = \frac{\tan \alpha_s(R(t))}{\tan \alpha_0}, \quad (2.183)$$

where $\tan \alpha_s(R(t))$ is given by Eq. (2.132), and $\tan \alpha_0 = \frac{400}{2\pi \times 5}$ for a single protofibril based on [91]. The stretches λ_* between the intermediate configuration and the final configuration in the directions other than that in the axial \mathbf{e}_z direction can be solved for each elapsed polymerization time t from Eq. (2.178). This calculated value of λ_* , along with the λ_s value, can be used to calculate λ_e in Eq. (2.180). In solving these equations, we use $\lambda_e = 1.501$. Finally, the network Piola-Kirchhoff stress T_{Rzz} can be computed from Eq. (2.179).

Using the above values and choosing $l = 0.5\mu m$, the Piola-Kirchhoff stress T_{Rzz} as a function of polymerization time t can be seen in Figure 2.9. As the clot polymerizes the tension increases, as expected. Steady state is reached by about 1000 seconds, in qualitative agreement with experiments.

To study the effect of the estimated parameter length l and final fiber radius R on the network Piola stress T_{Rzz} , we ran simulations with different values for each and compared the re-

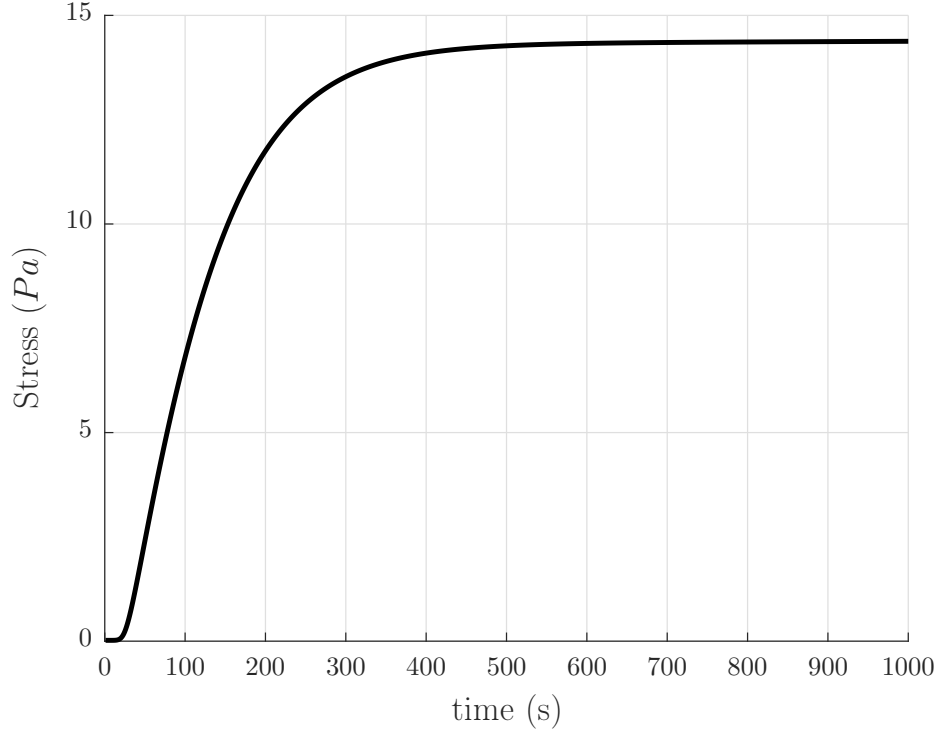


Figure 2.9: Piola-Kirchhoff stress T_{Rzz} in the network in the fixed number density formulation as a function of polymerization time t , using the length of the fiber connected in a network $l = 0.5\mu m$.

sults. Figure 2.10(a) depicts the change in Piola stress T_{Rzz} for fiber length l values in the range $0.5\mu m \geq l \geq 2.0\mu m$. As can be seen in Figure 2.10(a), larger fiber lengths produce smaller network Piola stresses T_{Rzz} . Additionally, as can be seen in Figure 2.10(b), thicker fibers of the same length produce larger network Piola stresses T_{Rzz} .

The above discussion held the number of fibers per unit reference volume constant, giving a density ν_{nd} . If, instead, as in experiments in Figure 2 in [68] and in other experiments [69], the solid volume fraction ϕ_s is held constant at $\phi_s = 0.01$ or 1%, a value previously estimated for plasma clot fibrin networks (see Figures S3 and S4 in the supplement of [69]), the density becomes

$$\nu = \nu_{vf} = \frac{\phi_s}{\pi R^2 \lambda_e \lambda_s L}. \quad (2.184)$$

When using this density in the calculations of network stress, results for varying different input parameters are more consistent. As can be seen in Figure 2.11(a), fibers of different lengths produced the same network stress T_{Rzz} ; this is not the same effect as in Figure 2.10(a) which held the number

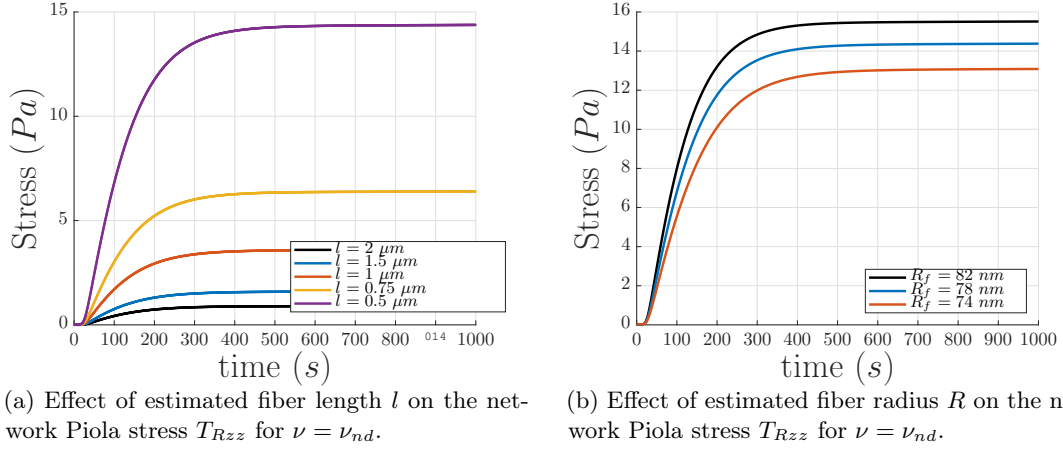


Figure 2.10: (a) Effect of estimated fiber length l on the network Piola stress T_{Rzz} using five values of l from the most likely range of l from the experimental probability distribution found in [105], as discussed in Section 2.3.2. These plots assume that l remains fixed as solid volume fraction ϕ_s evolves with time. (b) Network Piola stress T_{Rzz} vs. polymerization time t for constant fiber length $l = 0.5 \mu m$, for different final values of fiber radius R_f . Thicker fibers contribute more network Piola stress T_{Rzz} .

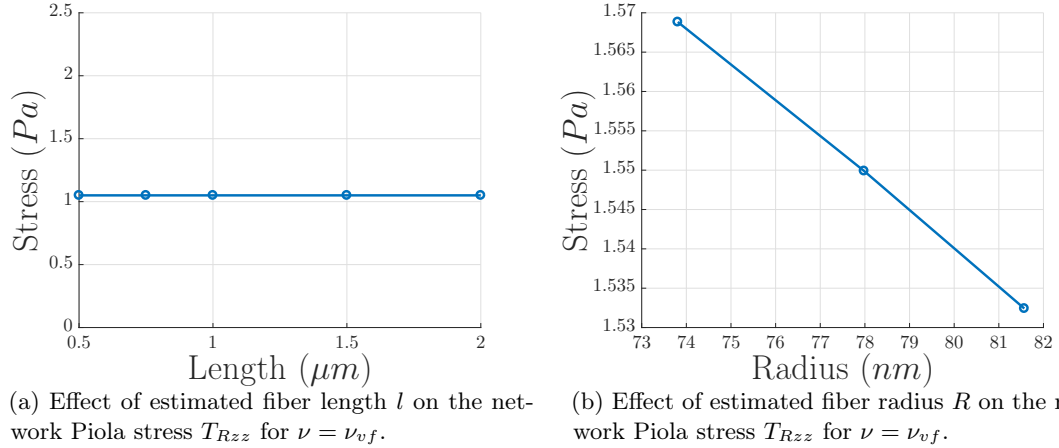


Figure 2.11: (a) Effect of estimated fiber length l on the final network Piola stress T_{Rzz} using five values of l from the most likely range of l from the probability distribution found in [105], as discussed in Section 2.3.2. (b) Effect of final fiber radius R on final network Piola stress T_{Rzz} , for constant fiber length $l = 0.5 \mu m$. Thinner fibers contribute more network Piola stress T_{Rzz} . Since the solid volume fraction during polymerization is not constant, only the values calculated from the final time in the polymerization have been included. The final solid volume fraction for each of these points is $\phi_s = 0.01$.

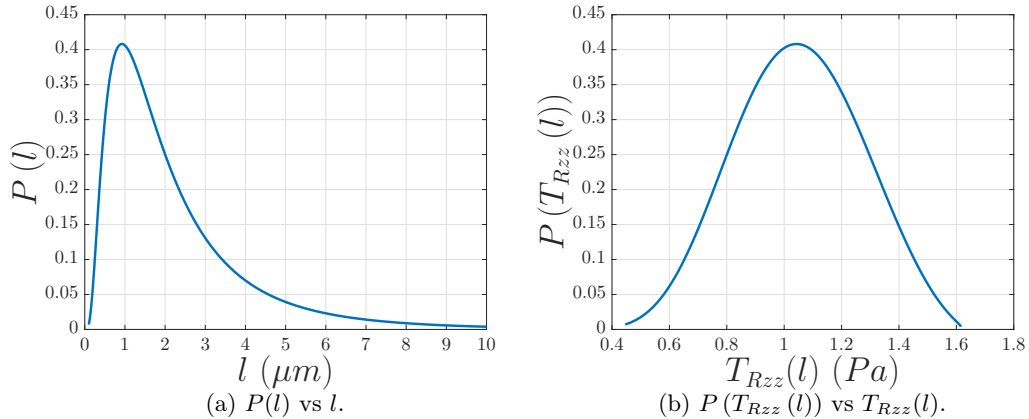


Figure 2.12: Probability distributions of (a) fiber lengths as found in [105], and (b) network stresses based on the fiber lengths and holding constant the solid volume fraction $\phi_s = 0.01$ as estimated in [69].

density of fibers fixed, where larger fiber lengths produce smaller network Piola stresses T_{Rzz} . Also, the estimated final values of the tensile stress are in agreement with experimental results in Figure 2 of [68]. Additionally, as can be observed in Figure 2.11(b), thinner fibers of the same length produce larger network Piola stresses T_{Rzz} , which is also different from the trend observed in Figure 2.10(b) which held the number density fixed. Recall from experiments [68] that increased thrombin concentration causes decrease in turbidity, which is related to the average protofibrils per fiber m [57], leading to a decrease in R . Thus, these results for $\nu = \nu_{vf}$ are in agreement with the trend expected from [57] and the results from experiments where increased thrombin concentration yields increased magnitude of network stress (see Section 2.6 in [68]). In a real network there is a distribution of fiber lengths, so we accounted for this in rudimentary way in 2.4 and showed that the resulting values of final tensile stress are not very different from those reported in Figure 2.11.

2.4 Distribution of Fibrin Fiber Lengths

Figure 2.12(a) depicts the probability distribution of fiber lengths in a fibrin network, as found in [105]. The probability density function is a log-normal distribution function of l with parameters $\mu = 0.53$ and $\sigma = 0.78$, as found in [105]. Figure 2.12(b) depicts the probability density of l vs the peak stress T_{Rzz} from the simulations utilizing that l as an input parameter, with the radius for

that given l calculated by

$$R = \sqrt{\frac{\phi_s}{\nu\pi l}}, \quad (2.185)$$

where the density $\nu = 0.1\mu m^{-3}$, as measured in [44], and T_{Rzz} is also calculated using $\nu = 0.1\mu m^{-3}$ from [44]. The mean value of T_{Rzz} is $1.21Pa$. This mean value is roughly of the same order of magnitude as the network Piola stresses T_{Rzz} calculated from the simulations in Figure 2.9. The stress values resulting from these computations are also of the same order of magnitude as the values produced by experiments in Section 2.6 in [68].

2.4.1 Summary of Full Mathematical Model

The model can be summarized as follows: The system of ODEs, resulting from the chemical rate equations governing fiber polymerization, are as follows:

$$\frac{d[f_A]}{dt} = -k_A[f_A] \quad (2.186)$$

$$\frac{d[f_1]}{dt} = -k_{pi} \left([f_1][f_1] + [f_1] \sum_{i=1}^{l_{agg}} [f_i] \right) - k_{pg}[f][f_n] + k_A[f_A] \quad (2.187)$$

$$\frac{d[f_j]}{dt} = k_{pi} \left(\sum_{i=1}^{\lfloor \frac{j}{2} \rfloor} [f_i][f_{j-i}] - [f_j][f_j] - [f_j] \sum_{i=1}^{l_{agg}} [f_i] \right) - k_{pg}[f_n][f_j] \quad \forall j \in [2, l_{agg}] \quad (2.188)$$

$$\frac{d[f_n]}{dt} = k_{pi} \left(\sum_{j=1}^{\lfloor \frac{l_{agg}+1}{2} \rfloor} \left(([f_j] + [f_{l_{agg}+1-j}]) \sum_{i=l_{agg}+1-j}^{l_{agg}} [f_i] \right) \right) - 2k_{fi}[f_n][f_n] - k_{fg}[f_r][f_n] \quad (2.189)$$

$$\frac{d[f_r]}{dt} = k_{fi}[f_n][f_n] - k_{fA}[f_r][f_r] \quad (2.190)$$

$$\frac{d[f_n^{tot}]}{dt} = 2k_{fi}[f_n][f_n] + k_{fg}[f_r][f_n] + k_{fA}[f_r][f_r] \quad (2.191)$$

$$\frac{d[c_{f_n}]}{dt} = k_{pi} \sum_{i=1}^{l_{agg}} \left((l_{agg} + i) \sum_{j=i}^{\lfloor \frac{l_{agg}+i}{2} \rfloor} [f_j][f_{l_{agg}+i-j}] \right) + k_{pg}[f_n] \sum_{i=1}^{l_{agg}} [f_i] - k_{fi}[f_n][c_{f_n}] - k_{fg}[f_r][c_{f_n}] \quad (2.192)$$

$$\frac{d[c_{f_r}]}{dt} = 2k_{fi}[f_n][c_{f_n}] + k_{fg}[f_r][c_{f_n}] + k_{fA}[f_r][f_r]. \quad (2.193)$$

with

$$m = \frac{[f_n^{tot}]}{[f_r]}. \quad (2.194)$$

The fiber radius R as a function of the average number of protofibrils per fiber cross-section m is

$$R(t) = r_m \sqrt{m(t)}. \quad (2.195)$$

The stretch connecting the imaginary reference configuration and the intermediate configuration of a fiber, as a function of fiber radius R , is given by

$$\lambda_s(R(t)) = \frac{\tan \alpha_s(R(t))}{\tan \alpha_0} = \frac{\sqrt{\frac{\ln\left(\frac{R(t)}{r_m}\right)}{\kappa_0(R(t)-r_m)} - 1}}{\frac{400}{2\pi \times 5}}. \quad (2.196)$$

The stretch between the intermediate configuration and the final configuration of the whole network in the directions other than that in the axial \mathbf{e}_z direction λ_* is calculated by solving

$$0 = \frac{\nu L}{3\lambda_e} \lambda_* F(\lambda_e) + \lambda_s \lambda_* f\left(\frac{\lambda_*^2}{\lambda_s}\right) \quad (2.197)$$

using the force in a fiber

$$F = \frac{2\pi}{a_0} K_b \sin \alpha \left(\kappa_0(R - r_m) - \cos^2 \alpha \ln \left(\frac{R}{r_m} \right) \right) \quad (2.198)$$

with

$$\tan \alpha = \lambda_e \tan \alpha_s = \lambda_e \sqrt{\frac{\ln\left(\frac{R(t)}{r_m}\right)}{\kappa_0(R(t)-r_m)} - 1}, \quad (2.199)$$

the stretch between the intermediate configuration and the final configuration

$$\lambda_e = \sqrt{\frac{2\lambda_*^2 \lambda_s^2 + 1}{3\lambda_s^2}}, \quad (2.200)$$

and the relationship between volumetric strain and pressure

$$f\left(\frac{\lambda_*^2}{\lambda_s}\right) = K\left(\frac{\lambda_*^2}{\lambda_s} - 1\right). \quad (2.201)$$

Then, the network Piola stress can be computed from

$$T_{Rzz} = \frac{\nu L}{3\lambda_e\lambda_s}F(\lambda_e) + \lambda_s^2\lambda_*f^2\left(\frac{\lambda_*^2}{\lambda_s}\right). \quad (2.202)$$

The model takes the unknown input parameters initial concentration of fibrinogen f_{A_0} , rate of fibrinopeptide A cleavage to convert fibrinogen to fibrin monomers k_A , the rate of association of fibrin monomers to yield small oligomers and initiate protofibril formation k_{pi} , the rate of protofibril growth in length by association with oligomers k_{pg} , the rate of protofibril aggregation to initiate a fiber k_{fi} , the rate of fiber growth by association with additional protofibrils k_{fg} , the rate of interactions between fibers k_{fA} , and initial length of a fiber connected in a network l . The model outputs the radius of a polymerizing fiber $R(t)$, force on a fiber F , the stretches λ_s and λ_e , the relaxed length of a fiber l/λ_e , and the network Piola stress T_{Rzz} .

2.5 Discussion

In this paper we have followed [53, 57] and modeled fibrin clot formation – from fibrinogen to fibrin monomers and oligomers to protofibrils to fiber formation – by a set of ODEs for the chemical rate of change in concentration of the reacting structures of each individual stage. The solution of that system of ODEs gives the average number of protofibrils per fiber cross-section as a function of polymerization time. Variation of the rate constants involved in the intermediary biochemical reactions demonstrates that the two most important stages determining final fiber radius are fiber initiation by lateral aggregation of protofibrils and fiber growth by transverse association with additional protofibrils. The resulting (final value of) average number of protofibrils per fiber cross-sectional area is directly related to the radius of a fiber. Therefore, we can calculate how the radius of a fiber evolves in time. This radius is used as an input to calculate the evolving tensile force in a fiber which ultimately determines the tensile force in a network constrained between two rheometer plates.

We assumed that since the radial distribution of protofibrils is disordered [53, 90], the number density of protofibrils per unit fiber cross-sectional area is constant. In particular, we assumed that

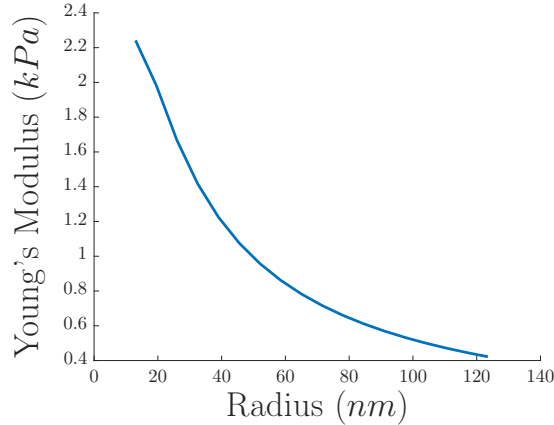


Figure 2.13: Calculated Young’s modulus of an individual fiber in a fibrin network vs. fiber radius. Note the trend that the Young’s modulus decreases with increasing radius.

a single protofibril occupies a circle of radius $6.5nm$ in the fiber cross-section. Thus, if the number of protofibrils in a fiber is known (from the solution of the ODEs), the radius of the fiber as a function of time can be calculated. The resulting values of the fiber radius are in line with the previously reported range of fibrin fiber radii of $25 - 115nm$ [69]. However, we note that other works suggest that the density of protofibrils per fiber cross-sectional area is not constant [86, 93, 108–111]; the number of protofibrils per fiber cross sectional area is proportional to $D^{1.3}$ [109] or $D^{1.4\pm 0.2}$ [111], and not D^2 as we have used. It has also been suggested that the fiber core is more dense than the periphery layers [111]. We used the constant number density assumption in our calculations due to its simplicity and also because a specific numerical value ($6.5nm$) for the inter-protofibril distance was available. On the other hand, other works [109, 111] provide scaling laws which do not furnish enough information to compute actual numerical values of the fiber radius. Additionally, even if a more accurate relationship between the number of protofibrils per fiber cross sectional area is specified, it will only change the computation of the radius from the average number of protofibrils in a fiber. Our overall approach of computing the fiber tension and the network tension will still remain the same. Furthermore, our simple assumption of constant number density of protofibrils per fiber cross-sectional area is able to capture a crucial experimental observation that the Young’s modulus of a fibrin fiber decreases with increasing radius, as demonstrated below.

Our equation (see Eq. (2.134)) for the force-stretch relation of a single fiber is derived by mathematicizing ideas in [53] which trace the origin of tension in fibrin fibers to the two-axis symmetry and off-axis binding sites of individual fibrin monomers. This causes protofibrils to be helical as

clearly seen in the the simulations of [91] and images of [94]. If a number of such helical protofibrils are to form a fibrin fiber by lateral aggregation then it is necessary that the individual monomers be properly aligned. This causes some protofibrils to stretch and others to shorten so that there is overall force balance in the cross-section [53]. We have enforced this force balance in a fiber cross-section by considering the equilibrium of each individual helical protofibril, which may have stretched or shortened depending on its location in the fiber cross-section. This force balance is expressed as Eq. (2.134) and the radius R of a fiber enters as a parameter in this equation. Starting with the force F in Eq. (2.134) and dividing by the assumed cross sectional area πR^2 , we get the stress σ in a fiber due to external force F . Then, since this stress and the stretch in Eq. (2.135) are both functions of the variable $\tan \alpha_e$, the Young's modulus E of a fiber may be calculated as

$$E = \left. \frac{d\sigma/d\alpha_e}{d\lambda_e/d\alpha_e} \right|_{\lambda_e=1} = \frac{4}{a_0 R^2} K_b \kappa_0 (R - r_m) \sin^3 \alpha_s. \quad (2.203)$$

The results of this equation can be found in Figure 2.13, and the trend of decreasing Young's modulus with increasing radius is similar to the trend in [110]. There may be additional contributions to individual fiber modulus, for example the long and largely unstructured α -C regions may have significant contribution as well [110], but we have captured the general trend in Figure 2.13.

The force-stretch relation given by Eq. (2.134) and Eq. (2.135) can be combined with the equation of motion of a fiber subject to fluid drag to predict the relaxation to equilibrium of a severed fibrin fiber. Here we have shown that the relaxation time depends on the fiber length and radius and the resulting time scales as well as fiber pre-strains are in excellent agreement with the cutting experiments of [60]. Importantly, we made no attempt to compare the forces (or stresses) in our calculations with those documented in [60] because the experimental values of the forces are obtained from the strains using a Young's modulus that is different from those calculated in Figure 2.13. Also, a simple linear relation between stress and strain in a single fibrin fiber may not be appropriate at large strains. Finally, we acknowledge that the process of enzymatic cleavage of a fibrin fiber (as in [112]) is quite complex since one would have to also model the diffusion and binding/unbinding of the enzyme together with mechanics of cleavage of individual protofibrils.

Finally, we connect the mechanical behavior of a fibrin network to that of individual fibers by using the 8-chain model [41, 49] together with the continuum mechanics of swellable gels [97]. Interestingly, models of 'swellable' elastomers are applicable here even though fibrin fibers tend to

R (nm)	λ_e	F (pN)	A_{fiber} (nm ²)	σ (Pa)
74	1.48	0.78	17,200	45.4
78	1.50	0.83	19,100	43.5
82	1.52	0.88	21,100	41.7

Table 2.2: Computed values for fiber (and network) stresses, given a fixed and uniform fiber radius for a “network” of fibers vertically connected between two horizontal plates with a fixed separation distance $0.5\mu m$. The fiber stretches λ_e are calculated using Eq. (2.184) in Eq. (2.178). Inherent forces in fibers F are computed from Eq. (2.134), using pitch angles calculated from Eq. (2.135). The cross-sectional area of each fiber $A_{fiber} = \pi R^2$. Inherent fiber stresses σ are computed by dividing the force F by the fiber cross-sectional area A_{fiber} .

‘shrink’ in length as their diameter increases with time. We show that the inherent tensile stress in polymerizing fibrin networks depends on fiber length, radius, solid volume fractions, etc. Our results from the continuum model in Section 2.3.3 are in agreement with the results from experiments. The order of magnitude of the inherent tension is the same in both experiments and continuum model and steady state is reached by around 1000s in both the model and the experiments. Additionally, our continuum model can recover the trend that thinner fibers produce larger network stress for fixed solid volume fraction as observed in recent experiments [68] coupled with the study of the effect of thrombin concentration on turbidity in [57], although the predicted trends from the model are weaker than those from experiments.

This trend in Figure 2.11(b) that thinner fibers produce larger network stress is not obvious. One hypothesis to explain this phenomenon involves the following simplified scenario: imagine that two fixed horizontal plates are connected by a “network” consisting of only vertical fibers of uniform thickness. Since the fibrin volume fraction is constant irrespective of the fiber radius, the total sum of the cross-sectional area of all those fibers will be the same whether the fibers are thinner or thicker, but there will be more thinner fibers in such a scenario than if the fibers were thicker. Now, from Eq. (2.134), the force in a fiber can be calculated as a function of the fiber radius, from which the inherent stress in the fiber can be computed by dividing by the cross-sectional area of a fiber πR^2 . If the cross-sectional area of a fiber increases faster as the radius increases than does the force in the fiber, the inherent stress in the fiber will decrease with radius, and the total “network” stress will decrease with fiber radius as well.

This can be better illustrated by the use of concrete examples, such as the three radii in Figure 2.11(b), namely, $R = 74nm$, $R = 78nm$, and $R = 82nm$. For these radii and choosing the same fiber length $l = 0.5\mu m$, the resulting fiber stretches λ_e from using Eq. (2.184) in Eq. (2.178) are

$\lambda_e = 1.48$, $\lambda_e = 1.50$, and $\lambda_e = 1.52$, respectively. With these values and computing the pitch angle α_e from Eq. (2.135), the inherent forces in each fiber are $F = 0.78pN$, $F = 0.83pN$, and $0.88pN$, respectively. The cross-sectional area of each fiber is $A_{fiber} = 17200nm^2$, $A_{fiber} = 19100nm^2$, and $A_{fiber} = 21100nm^2$, respectively, which, combined with the inherent forces in the fibers, yields the fiber inherent stresses $\sigma = 45.4Pa$, $\sigma = 43.5Pa$, and $41.7Pa$, respectively. It should be noted that these calculations were performed in a simplified scenario to illustrate one possible hypothesis, and they do not take into account confounding factors such as the isotropic nature of fibrin gels or branch points, although they give some physical intuition for the phenomenon.

Our calculation based on the 8-chain model assumes a given constant length of all fibers, but this is not the case for real fibrin networks. The constant length we use to compute pre-tension should really be interpreted as the average fiber length in a network. We may be able to do slightly better by using the probability density function for the fiber lengths and computing a probability density for the pre-tension values obtained (see 2.4). However, this still does not account exactly for the different values of pre-tension in each fiber of a real fibrin gel, although it does utilize known information about the structure of a true fibrin network. A proper accounting of the variation of fiber lengths to predict pre-tension in a network will likely require computations that are beyond the scope of the research presented in this paper.

Pre-tension in fibrin networks specifically is important because it contributes to the stability of the material. Fibrin fiber networks, as well as many other biological networks, have connectivity (average number of fibers connected at a junction) below the Maxwell isostatic threshold, which, for networks with a large number of elements, is twice the dimensionality [113–115]. Thus, if the fiber interactions were limited to tension and compression central forces, the network materials would be unstable for small deformations and would be floppy rather than rigid [114, 115]. The presence of pre-tension in fibrin networks, similar to the presence of fiber bending in F-actin networks in cytoskeletons [116], active stresses generated by myosin motors in cytoskeletal networks [117] and in fibrin networks in blood clots [118], thermal fluctuations [49, 119], and osmotic pressure in actin networks [100], stabilizes and rigidifies the network material [114, 115].

Estimations of inherent stress in a fibrin fiber network, as well as of other network material properties, will be useful in interpreting experiments performed on blood clots and thrombi, in the use of fibrin as a biomaterial – for example, the inherent tension may comprise a thermodynamic mechanism to control fiber diameter, and thus modulate the overall network structure – and in

the application and development of novel methods of treatment of thrombotic states such as in mechanical thrombectomy since the susceptibility of fibrin to fibrinolytic enzymes depends strongly on the mechanical tension of the proteinaceous fibrous substrate [58–61]. Thus, variation of the tension in fibers and the structure of the fibrin network can affect mechanical and enzymatic stability of entire blood clots and thrombi, which determines the course and outcome of hemostatic disorders [37, 62].

Chapter 3

Structure, Mechanical Properties, and Modeling of Cyclically Compressed Pulmonary Emboli

This chapter is based on work published in [1] I. N. Chernysh, R. Spiewak, C. L. Cambor, P. K. Purohit, and J. W. Weisel. “Structure, mechanical properties, and modeling of cyclically compressed pulmonary emboli”, *Journal of the Mechanical Behavior of Biomedical Materials*, **105**: 103699, (2020). DOI:10.1016/j.jmbbm.2020.103699.

Abstract

Pulmonary embolism occurs when blood flow to a part of the lungs is blocked by a venous thrombus that has traveled from the lower limbs. Little is known about the mechanical behavior of emboli under compressive forces from the surrounding musculature and blood pressure. We measured the stress-strain responses of human pulmonary emboli under cyclic compression, and showed that emboli exhibit a hysteretic stress-strain curve. The fibrin fibers and red blood cells (RBCs) are damaged during the compression process, causing irreversible changes in the structure of the emboli. We showed that damage is accumulated as more cycles are applied. The stress-strain curves depend on embolus structure, such that variations in composition give quantitatively different responses. Emboli with a high fibrin component demonstrate higher normal stress compared to emboli that have a high RBC component. We describe the hysteretic response characteristic of foams, using a model of phase transitions in which the compressed foam is segregated into coexisting rarefied and densified phases whose fractions change during compression. Our model takes account of the rupture of RBCs in the compressed emboli and stresses due to fluid flow through their small pores. Our results can help in classifying emboli as rich in fibrin or rich in red blood cells, and can help in understanding what responses to expect

when stresses are applied to thrombi *in vivo*.

3.1 Introduction

Venous thromboembolism is a pathological condition in which a blood clot forms in the veins, most often in the deep veins of the lower extremity, groin, or less commonly in the upper extremity. Venous thrombi result from a combination of hypercoagulability with injured or activated endothelium and impaired blood flow [120, 121] with one of the most serious and common consequences being pulmonary embolism. The propagation and dissolution of venous thrombi are associated with the balance between local and systemic thrombogenic stimuli and protective anticoagulant and fibrinolytic mechanisms [122–124]. If part of a thrombus embolizes and travels in the circulation and lodges in the lungs, the result is pulmonary embolism. Because the clot can block blood flow to part of the lungs, pulmonary embolism is often a fatal type of vascular disease, with an estimated global incidence rate of 115-269 per 100,000 and mortality rate of 9.4-32.3 per 100,000 [125]. Around 23% of patients with pulmonary embolism die, either undiagnosed or within one day of diagnosis [126], with the high mortality rate being attributed in part to difficulties in identification and management.

Pulmonary embolism is a complex disorder divided into four major disease processes, including venous thrombosis, thrombus in transit or pulmonary embolism, acute pulmonary embolism, and pulmonary circulation reconstruction. All these aspects of pulmonary embolism have been studied intensively using a variety of approaches ranging from epidemiological and diagnostic studies to some detailed molecular, cellular and genetic approaches, as well as *ex vivo* pathological studies and clinical trials. Those studies were primarily focused on the pathological changes in the blood component of the disease, coagulation pathways, the function of vascular smooth muscle cells, microvesicles, and the inflammatory pathways that play key roles in pulmonary embolism [127–131].

Less is known about the mechanical properties of thrombi or thromboemboli. Thrombi are subject to many types of forces, such as those generated in the vasculature by blood flow and those generated by platelets pulling on fibrin in clot contraction, and forces as a result of muscle contraction of the vessel wall, cardiac muscle and striated muscles adjacent to the blood vessels, especially in the veins of the lower limbs. As a result, the structure of the developing thrombus can be modified from these forces, and on the other hand, increasing thrombus size alters blood flow. Irregular vessel geometry due to thrombus development may result in stenosis and complicated flow patterns. For

example, reduction in a vessel diameter by 75% stenosis results in 94% decrease in luminal cross section area that causes approximately a 64-fold increase in wall shear, such that pathological shear rates may exceed $250,000 \text{ s}^{-1}$ [132, 133]. Increasing shear rate impairs normal vascular function and may result in embolization of thrombi [134, 135]. In summary, there are multiple forces acting on a growing thrombus, including shear, tensile, and compressive forces.

A number of models have been developed to quantify and help to understand the mechanical properties of blood clots, including compressive studies of platelet-poor, platelet-rich and whole blood clots [63]. It has been demonstrated that fibrin networks exhibit foam-like behavior with compression [44]. Most of those studies of clot mechanics, including compression of blood clots, have been carried out *in vitro* using clots made only of fibrin or whole blood [63–66], but the structure of *in vivo* thrombi or emboli differ [67].

There are not many *ex vivo* studies on thrombi or emboli because of the difficulty of obtaining such material. In one study, tensile loading of a thrombus showed that the material exhibited linear or mildly non-linear response [136, 137], while the results from another group clearly demonstrated non-linear elastic behavior [138]. A study of the effects of aging on compression of human thromboemboli demonstrated that aged thromboemboli had a highly compact structure and were prone to fragmentation compared to fresh thromboemboli, which are soft and elastic [139]. Another study showed that applying and holding a low (5%) compressive strain over time results in a decrease of compressive load during a stress-relaxation test [140].

In this study, we used *ex vivo* human pulmonary emboli as a model for thromboemboli and investigated the mechanical response and structural changes with cycling of compression to maximum compressive strain and passive decompression. Compression impinges on thrombi developing inside a vessel, where they are subject to the forces from contraction of the vessel wall or muscles surrounding the vessel, or cardiac muscle. Moreover, cyclic compression arises from pulsatile blood flow. This new knowledge is important to understand structural changes that may happen during thromboemboli developing *in vivo* in a vessel, and may help to evaluate risks of embolization of thrombi as well as for developing new approaches to therapy, such as removal by thrombectomy.

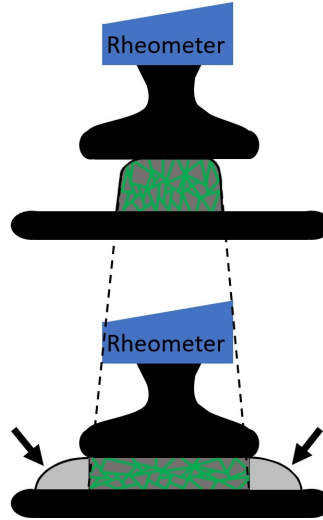


Figure 3.1: Experimental set-up to obtain rheological data for compression experiments. Schematic illustration of compression of an embolus placed between the rheometer plates. Rheometer plates are shown in black. The dark gray shapes represent the embolus, while the light gray shape represents the liquid expelled from the embolus during the compression cycle. The embolus was compressed as the upper rheometer plate moved down, squeezing liquid out of the embolus. Dashed line shows changes in area after the embolus was compressed. Arrows indicate liquid expelled from the embolus. The green lines in the embolus represent the isotropic form of the fiber network.

3.2 Materials and methods

Pulmonary emboli ($n=3$) were obtained during autopsies performed in the Department of Pathology, Hospital of the University of Pennsylvania (Philadelphia, Pennsylvania, USA), within 24 hours after the patient's death. These specimens from pulmonary arteries were all large (several centimeters) and from patient review most likely arose from the lower limbs. The emboli were stored in phosphate buffered saline, pH 7.4, and experiments were carried out in a timely fashion to minimize storage time. Changes that might have occurred post mortem are unknown but no morphological signs of fibrinolysis [141] or other post-mortem changes were observed.

Emboli were positioned between two 40 mm plates of a rheometer (ARG2; TA Instruments, New Castle, DE) with a built-in temperature control system, and compressed continuously at rates of $10 \mu\text{m}/\text{min}$ (see Figure 3.1). After the upper plate was moved down to apply an axial force on the upper surface of the embolus and the maximum compressive strain was achieved, the upper plate was returned to its starting position at the same rate. However, since the embolus is not attached to the rheometer plate, it was allowed to rise back up by passive decompression with no external forces applied. Emboli were exposed to repeated compressive/decompressive loads. Emboli were

vertically squeezed to various degrees of compression: the first set of compression/decompression cycles was at $0 \leq \epsilon \leq 0.5$ compressive strain, the second set of compression/decompression cycles was at $0.5 \leq \epsilon \leq 0.75$ or $0.5 \leq \epsilon \leq 0.8$, and the third set of compression/decompression cycles was at $0.75 \leq \epsilon \leq 0.9$ or $0.8 \leq \epsilon \leq 0.9$. Three cycles were done for each set of compression /decompression. The compressive strain (degree of compression) was defined as the absolute fractional change in embolus thickness $\epsilon = |\Delta h/h_0|$, where $\Delta h = h - h_0$, and h_0 and h are the thickness dimensions of the uncompressed and compressed embolus, respectively. During compression and decompression, the normal stress was measured and stress-strain curves were plotted for further analysis.

3.3 Modeling framework

Blood clots and thrombi/emboli are composed of a fibrin network, platelets, and Red Blood Cells (RBCs), and the RBCs release fluid upon lysis. We develop a simple microscopically informed model, taking into account the lysis of RBCs and leakage of fluid under compression. A key feature of our model is the transition from a rarefied to a densified phase of the fiber network that is characteristic of foams under compression; hence, we do not assume the material to be homogeneous after deformation.

The total stress in blood clots or thrombi under compression can be modeled as a combination of the stress carried by the fibrin network σ_{net} , the stress carried by RBCs σ_{RBC} , and the stress due to fluid flow σ_{fl} :

$$\sigma = \sigma_{net} + \sigma_{RBC} + \sigma_{fl}. \quad (3.1)$$

Following previous work [63], we denote compressive stresses and compressive strains as positive ($\sigma > 0$ and $\epsilon > 0$ for compression).

3.3.1 Fibrin network contribution

It has been demonstrated earlier that the stress-strain response of the fibrin network is composed of three segments: a rarefied phase, a densified phase, and a transition phase between them [63].

3.3.1.1 Rarefied Phase

The rarefied phase has a linear stress-strain response [29, 63]

$$\epsilon = \Gamma_L(\sigma) = \frac{\sigma - \sigma_{pre}}{E_L}, \quad (3.2)$$

where E_L is the modulus of the fibrin network and $\sigma_{pre} \leq 0$ is a pre-stress to account for the effect of platelets [63, 142, 143]. It has been shown [45, 63] that E_L is related to the Young's modulus of a single fiber E_s by

$$E_L = E_s \phi_0^2, \quad (3.3)$$

where ϕ_0 is the volume fraction of the fibrin network. Additionally, since platelets are much smaller than RBCs, they make up a much smaller part of the volume of the clot than the RBCs. Additionally, whereas RBCs flow with the fluid at low stresses and lyse at higher stresses, the platelets are firmly adherent to the fibrin. However, platelets do apply contractile forces to the fibrin network, the effect of which is a pre-tension in the network. We account for this pre-tension as σ_{pre} .

3.3.1.2 Densified Phase

In the densified phase, fibers are bent and buckled, and some have even broken. The nonlinear stress-strain response for dense networks has the form [6, 11, 63]

$$\sigma = kE_s(\phi^3 - \phi_0^3), \quad (3.4)$$

where $k \approx 0.1$ is determined by the material and loading conditions [44, 63], and

$$\phi = \frac{\phi_0}{1 - \epsilon} \quad (3.5)$$

is the increase in volume fraction of the clot with clot compression [44, 63], where ϕ_0 is the initial volume fraction of the clot.

Additionally, fibrin fibers sticking to each other reduces the free energy of the network. We can treat each contact point between fibers as a bond that releases free energy U_{bond} , so that the total

free energy per unit deformed volume is given by [63]

$$E = N_c U_{bond} + \int \sigma d\epsilon, \quad (3.6)$$

where

$$N_c = C\phi^2 \quad (3.7)$$

is the number of contact points per unit volume in a dense isotropic network [6, 63] and C is a material constant. Inserting Eqs. (3.7), (3.4), and (3.5) into Eq. (3.6) and then differentiating with respect to ϵ , we arrive at a new stress-strain law for the densified region [63]:

$$\sigma = \frac{2C\phi_0^2 U_{bond} + kE_s\phi_0^3}{(1-\epsilon)^3} - kE_s\phi_0^3 = \frac{K - \Delta G}{(1-\epsilon)^3} - K, \quad (3.8)$$

where

$$K = kE_s\phi_0^3 \quad (3.9)$$

is a constant with units of stress and

$$\Delta G = -2CU_{bond}\phi_0^2 \quad (3.10)$$

is a normalized bonding energy density.

Thus, the densified phase has nonlinear stress-strain response [6, 44, 63, 144]

$$\epsilon = \Gamma_H(\sigma) = 1 - \left(\frac{K - \Delta G}{\sigma + K} \right)^{\frac{1}{3}}, \quad (3.11)$$

3.3.1.3 Transition phase

As a fibrin network is compressed, it transitions from being fully in the rarefied phase to being fully in the densified phase. In the transition phase, the rarefied phase and densified phase coexist in distinct regions separated by a phase transition front or phase boundary [63, 64]. The transition to the densified phase begins at stress $\sigma_{LH} < \sigma_M$, where σ_M is the maximum stress at which the rarefied phase can exist. Similarly, for decompression, the network starts in the densified phase, and the transition to the rarefied phase begins at $\sigma_{HL} > \sigma_m$, where σ_m is the minimum stress at which the densified phase can exist. Also, $\sigma_{LH} > \sigma_{HL}$, so both phases can exist at stress σ in the region

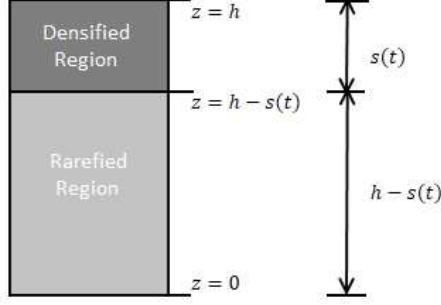


Figure 3.2: Diagram of the rarefied and densified regions in relation to the reference frame.

$\sigma_{HL} \leq \sigma \leq \sigma_{LH}$. The transformation strain is defined as [46, 63]

$$\gamma_T(\sigma) = \Gamma_H(\sigma) - \Gamma_L(\sigma) = 1 - \left(\frac{K - \Delta G}{\sigma + K} \right)^{\frac{1}{3}} - \frac{\sigma - \sigma_{pre}}{E_L}, \quad (\sigma_m \leq \sigma \leq \sigma_M). \quad (3.12)$$

During loading and unloading, we assume that the phase transition occurs under quasi-static conditions, so the stress in any part of the embolus is the same. Letting h be the initial height of the embolus, and z ($0 \leq z \leq h$) be the reference coordinate along the direction of loading, $w(z, t)$ be the local vertical displacement, and fixing the reference frame $z = 0$ at the bottom of the embolus, then $w(0, t) = 0$ for all t . The displacement at the top of the embolus is denoted as $\delta(t) = w(h, t)$ [63]. If for $\sigma_{HL} \leq \sigma \leq \sigma_{LH}$ there is a separation at $z = h - s(t)$ between the two parts of the continuum, such that for $z < h - s(t)$ the network is in the rarefied phase and for $z > h - s(t)$ the network is in the densified phase, the displacement at the top is given by [63]

$$\delta(t) = \Gamma_L(\sigma(t)) [h - s(t)] + \Gamma_H(\sigma(t)) s(t). \quad (3.13)$$

Thus, $h - s(t)$ represents the height of the phase boundary (see Figure 3.2), and $\frac{s(t)}{h}$ is the fraction of densified phase. To describe the motion of the phase boundary $s(t)$ as it moves from the top of the clot to the bottom, a kinetic law is introduced [46, 63]:

$$\dot{s} = \Phi(f) = \begin{cases} M_{LH}(f - f_{LH}), & f > f_{LH} \\ 0, & f_{HL} \leq f \leq f_{LH} \\ M_{HL}(f - f_{HL}), & f < f_{HL} \end{cases}, \quad (3.14)$$

where Φ is a material property [46, 63] and

$$f(\sigma) = \int_{\sigma_0}^{\sigma} \gamma_T(\sigma') d\sigma' \quad (3.15)$$

is the driving force on the phase boundary [46, 63]. f is assumed to be a unique function of stress, σ_0 is a Maxwell stress at which the Gibbs free energy of both phases are equal, $M_{LH} > 0$ and $M_{HL} > 0$ are mobilities that could be fitted to experimental data and are not necessarily equal, and $f_{LH} = f(\sigma_{LH})$ and $f_{HL} = f(\sigma_{HL})$ [46, 63]. $\Phi(f)$ must also satisfy the dissipation condition $f\Phi(f) \geq 0$ [46, 63]. The nucleation criteria can be defined as follows: the stress σ_{LH} at which the densified phase nucleates in the rarefied phase during loading is assumed to be where the driving force f is just greater than f_{LH} , and the stress σ_{HL} at which the rarefied phase nucleates in the densified phase during unloading is assumed to be where the driving force f is just less than f_{HL} . This is done so that the phase boundary begins to move as soon as it appears [63]. Finally, the differential equation governing the phase transition is [63]

$$\dot{\sigma} = \frac{\frac{\gamma_T(\sigma)}{h} (\gamma_T(\sigma)\dot{s} - \dot{\delta})}{\Gamma_L(\sigma)\Gamma'_H(\sigma) - \Gamma'_L(\sigma)\Gamma_H(\sigma) - \gamma'_T(\sigma)\frac{\delta}{h}}. \quad (3.16)$$

Thus, the stress contribution from the network σ_{net} is defined as

$$\sigma_{net} \equiv \begin{cases} \sigma_{net} = -\sigma_{pre} + E_L \epsilon, & \text{fully rarefied phase} \\ \dot{\sigma}_{net} = \frac{\frac{\gamma_T(\sigma)}{h} (\gamma_T(\sigma)\dot{s} - \dot{\delta})}{\Gamma_L(\sigma)\Gamma'_H(\sigma) - \Gamma'_L(\sigma)\Gamma_H(\sigma) - \gamma'_T(\sigma)\frac{\delta}{h}}, & \text{transition phase} \\ \sigma_{net} = \frac{K - \Delta G}{(1 - \epsilon)^3} - K, & \text{fully densified phase} \end{cases}. \quad (3.17)$$

3.3.1.4 Cauchy stress to Piola stress conversion

The phase transition theory discussed above uses the Piola, or nominal stress. The derivations below for RBC contribution and fluid contribution use Cauchy stress. To be consistent and work with Piola stress, we must convert the Cauchy stresses to Piola stress. This conversion can be done by considering the definitions of Cauchy stress $\sigma = \frac{F}{A}$ and of Piola stress $\tau = \frac{F}{A_0}$, where F is the applied force, A is the cross-sectional area of the current configuration, and A_0 is the cross-sectional

area of the reference configuration. Since F is the same in both expressions,

$$\tau = \frac{A}{A_0}\sigma. \quad (3.18)$$

The current cross-sectional area A of the deformed embolus is computed by linear interpolation of the experimentally measured initial cross-sectional area A_0 and final cross-sectional area A_f :

$$A = \frac{A_f - A_0}{\epsilon_f - \epsilon_0}(\epsilon - \epsilon_0) + A_0, \quad (3.19)$$

where $\epsilon_0 = 0$ since there is no strain before any compression and $\epsilon_f = 1 - \frac{h_f}{h}$, where h is the initial height of the embolus and h_f is the final height of the embolus. Thus, the conversion from Cauchy stress σ to Piola stress τ is

$$\tau = \frac{A}{A_0}\sigma = \left(\frac{\frac{A_f}{A_0} - 1}{1 - \frac{h_f}{h}}\epsilon + 1 \right)\sigma. \quad (3.20)$$

3.3.2 RBC contribution

The large deformation response of RBCs under tension and compression has been studied [145, 146] using a nonlinearly elastic neo-Hookean model given by [147–149]. This model was shown to predict the compression response of blood clots quite well [63]. In our notation (in which $\sigma > 0$ and $\epsilon > 0$ for compression), this model for RBCs in uniaxial deformation is given by [150]

$$\sigma_{neo} = 2C_{neo} \left(3\epsilon + \frac{\epsilon^3}{1 - \epsilon} \right), \quad (3.21)$$

where C_{neo} is a material constant that can be fitted to the experimental data [63]. Since only the RBCs from the densified phase become deformed, of the initial volume fraction of RBCs in the clot, only the fraction of RBCs that were in the densified region carry stress. Denoting the initial volume fraction of RBCs for a given cycle as $f_{0, \min \leq \epsilon \leq \max}$ in a strain region $\min \leq \epsilon \leq \max$, we then approximate the stress carried by the RBCs, after converting from Cauchy stress to Piola stress (details for which can be found in Section 3.3.1.4), as

$$\sigma_{RBC} = \frac{A}{A_0} f_{0, \min \leq \epsilon \leq \max} \frac{s(t)}{h} \sigma_{neo} = \frac{A}{A_0} f_{0, \min \leq \epsilon \leq \max} \frac{s(t)}{h} 2C_{neo} \left(3\epsilon + \frac{\epsilon^3}{1 - \epsilon} \right), \quad (3.22)$$

where A is the current cross-sectional area of the embolus and A_0 is the initial cross-sectional area. $f_{0,\min\leq\epsilon\leq\max}$ can be fitted to experimental data for a given region, with the caveat that since some RBCs lyse during compression, $f_{0,\min\leq\epsilon\leq\max}$ should be reduced for every subsequent cycle.

3.3.3 Fluid contribution

Liang, *et al.* have shown that the stress-strain response and the width of the phase boundary in thrombi depend on the compression rate. This suggests that the poroelastic effects of fluid pumping significantly contribute to the stress [63]. It has been observed by Kim, *et al.* that in a clot compressed from the top, labeled beads situated at the bottom of the clot only move when the phase boundary reaches the bottom of the clot [44]. Thus, fluid at the bottom does not move much before the phase boundary reaches the bottom. On the other hand, at the top of the clot, the clot is densified and the fluid is pumped out. Accordingly, the stress contribution from the fluid pumping must be dependent upon the size of the densified region or the location of the phase boundary, and not simply the analytic formula for compressive stress of a poro-viscoelastic foam under compression given by [45, 63]. Following Gibson and Ashby [45], we will use Darcy's law to relate the flux of fluid to the local pressure gradient in the porous medium:

$$q = -\frac{k}{\mu} \frac{dp}{dx} \approx \frac{k}{\mu} \frac{\sigma}{L}, \quad (3.23)$$

where μ is the viscosity of fluid, the permeability $k \propto l^2(1 - \epsilon)$, where l is the pore size in the reference configuration, and the pressure gradient $\frac{dp}{dx} \approx -\frac{\sigma}{L}$, where L is the horizontal dimension of the clot in the deformed configuration. Note that the stress σ is the same in both the densified and rarefied region but it is carried differently due to the strain ϵ_H in the densified region being different from the strain ϵ_L in the rarefied region. Let the velocity of compression at the top of the clot be V relative to the reference frame, the velocity of the phase boundary in the deformed configuration be v_{ph} , the height of the clot in the reference configuration be h , and the permeability and viscosity in the rarefied phase and densified phase be $k_L \propto l^2(1 - \epsilon_L)$, μ_L , $k_H \propto l^2(1 - \epsilon_H)$, and μ_H , respectively. Following Gibson and Ashby [45], and equating the fluxes of fluid through the sides of the clot to the fluxes due to vertical compression and applying Darcy's law, we have the two equations

$$\frac{k_H}{\mu_H} \frac{\sigma}{L} = \frac{(V - v_{ph})L}{2s(t)(1 - \epsilon_H)} \quad (3.24)$$

$$\frac{k_L}{\mu_L} \frac{\sigma}{L} = \frac{(v_{ph})L}{2(h-s(t))(1-\epsilon_L)}, \quad (3.25)$$

from which we conclude that the Cauchy stress σ due to fluid flow, in terms of the current area A , is

$$\sigma = V \frac{A}{l^2} \frac{1}{\frac{(h-s(t))(1-\epsilon_L)^2}{\mu_L} + \frac{s(t)(1-\epsilon_H)^2}{\mu_H}}. \quad (3.26)$$

Converting to Piola stress, as described in Section 3.3.1.4 above, yields

$$\sigma_{fl} = V \frac{A^2}{A_0 l^2} \frac{1}{\frac{(h-s(t))(1-\epsilon_L)^2}{\mu_L} + \frac{s(t)(1-\epsilon_H)^2}{\mu_H}}. \quad (3.27)$$

Gibson and Ashbey [45] give the contribution of pore fluid in foams as

$$\sigma_g^* = \frac{C\mu\dot{\epsilon}}{1-\epsilon} \left(\frac{L}{l} \right)^2, \quad (3.28)$$

where the strain rate

$$\dot{\epsilon} = \frac{V}{h(1-\epsilon)}. \quad (3.29)$$

If we take $s(t) = 0$ as is the case in the fully rarefied phase, then Eq. (3.26) becomes

$$\sigma = \frac{V}{h} \frac{A}{l^2} \frac{\mu_L}{(1-\epsilon_L)^2}, \quad (3.30)$$

and we recover the result Eq. (3.28) in terms of current area A . Similarly, if we take $s(t) = h$ as is the case in the fully densified phase, then Eq. (3.26) becomes

$$\sigma = \frac{V}{h} \frac{A}{l^2} \frac{\mu_H}{(1-\epsilon_H)^2}, \quad (3.31)$$

which again is the same form as Eq. (3.28) with different constants.

3.4 Model application

The stress-strain curves of emboli under compression can be computed using these ideas and fitted to the experimental data, as follows. The initial and final heights and cross-sectional areas, h and h_f , and A_0 and A_f , respectively, of an embolus are given, as well as the compression rate V . We begin by

fitting the high strain non-linear response of the network using the data in the decompression cycle of the chosen fitting region and Eq. (3.11). We choose a region of data points in the decompression cycle for which we assume that the transition to the rarefied phase has not yet begun. We use the decompression cycle because only the network carries stress in the decompression cycle; since the embolus is not attached to the compression plate, fluid is not pumped back into the embolus, and since the RBCs do not re-form once they lyse, RBCs do not contribute to decompression stresses. Next, we fit the low strain linear response of the network using the data from the decompression cycle in the approximate strain region $0 \leq \epsilon \leq 0.05$ and Eq. (3.2), and obtain values for σ_{pre} and E_L .

Then, we consider the transition region, and remember that the curve is given by $\epsilon = \frac{\delta(t)}{h}$ (see Eq. (3.13) and Eq. (3.16)). With $\Gamma_L(\sigma)$ and $\Gamma_H(\sigma)$ already known, we want to fit the plateau regions of the stress-strain curves using Eq. (3.16). Our remaining fitting parameters are, for the upper plateau, σ_{LH} and M_{LH} , and for the lower plateau, σ_{HL} and M_{HL} .

Next we consider the RBC contribution, using Eq. (3.22). The fitting parameters are C_{neo} and $f_{0, \epsilon_{min} \leq \epsilon \leq \epsilon_{max}}$. We can estimate the order of magnitude of C_{neo} by considering small strains such that Eq. (3.22) can be approximated linearly as $\sigma_{RBC} \approx 6C_{neo}f_{0, \min \leq \epsilon \leq \max} \epsilon$, the network contribution is just $\sigma_{net} = (1 - f_{0, \min \leq \epsilon \leq \max}) E_L \epsilon$, and the fluid contribution is zero because fluids are released mostly due to lysis of RBC. Thus,

$$\sigma \approx (6C_{neo}f_{0, \min \leq \epsilon \leq \max} + (1 - f_{0, \min \leq \epsilon \leq \max}) E_L) \epsilon. \quad (3.32)$$

Approximating $E_L \approx 1 \text{ kPa}$, the stress at strain $\epsilon \approx 0.15$ in Figure 3(B) of [1], where $f_{0, \min \leq \epsilon \leq \max} = 0.7$, is $\sigma \approx 5.7 \text{ kPa}$. Thus, from Eq. (3.32), $C_{neo} \approx 9 \text{ kPa}$. More exact values of C_{neo} can be fit from the experimental data (see Table 3.2). Some RBCs are irreversibly damaged as loading/unloading ensues. The damaged cells will not be able to carry load, so the fraction of load-carrying (or intact) red blood cells (f_0) also decreases from one cycle to the next. However, the mechanical properties of the load carrying red blood cells (C_{neo}) do not change.

Finally, we consider the fluid contribution using Eq. (3.27). Since the entire fluid contribution in our model comes from fluid leaking out of RBCs and in the very first cycle no RBCs have lysed, for the very first cycle $\sigma_{fl} = 0$. Since the fluid that leaks out of RBCs that have lysed is basically water and is the same in both the rarefied region and the densified region, $\mu_L = \mu_H = 1.002 \times 10^{-6} \text{ kPa s}$.

Embolus	h (mm)	h_f (mm)	A_0 (mm ²)	A_f (mm ²)
1	5.3	0.5	158.8	1489
2	2.56	0.2	131.2	313.7
3a	2.60	0.33	120.81	266.4
3b	2.80	0.35	74	383
3c	2.23	0.28	177.4	236

Table 3.1: Initial and final heights and cross-sectional areas of emboli #1, #2, #3a, #3b, and #3c.

Thus, the fitting parameter is l , which can be estimated from Figure 5 in [1] to be less than a micron for pulmonary emboli. This is smaller than that in whole blood clots shown in Figure 4 in [1].

A nice feature of this theoretical study is that it can reveal the location of the phase boundary as a function of ϵ , which the experiments cannot directly observe. The locations of the phase boundaries are found using $\frac{s(t)}{h}$, and inverting Eq. (3.13) after substituting in the relation $\epsilon = \frac{\delta(t)}{h}$.

3.5 Results and Discussion

Embolus #1 has initial and final heights and cross-sectional areas $h = 5.3\text{mm}$, $h_f = 0.5\text{mm}$, $A_0 = 158.8\text{mm}^2$, and $A_f = 1489\text{mm}^2$, respectively, and embolus #2 has $h = 2.56\text{mm}$, $h_f = 0.2\text{mm}$, $A_0 = 131.2\text{mm}^2$, and $A_f = 313.7\text{mm}^2$ (see Table 3.1). Embolus #3 was cut into three sections (a, b, and c), each of which was treated individually. The stress-strain responses of sections a, b and c were measured and fitted separately. Embolus #3a has $h = 2.60\text{mm}$, $h_f = 0.33\text{mm}$, $A_0 = 120.81\text{mm}^2$, and $A_f = 266.4\text{mm}^2$. Embolus #3b has $h = 2.80\text{mm}$, $h_f = 0.35\text{mm}$, $A_0 = 74\text{mm}^2$, and $A_f = 383\text{mm}^2$. Embolus #3c has $h = 2.23\text{mm}$, $h_f = 0.28\text{mm}$, $A_0 = 177.4\text{mm}^2$, and $A_f = 236\text{mm}^2$ (see Table 3.1).

All the fitting parameters are summarized in Table 3.2(a) for embolus #1 and Table 3.2(b) for embolus #2, and in Table 3.3(a) for embolus #3a, Table 3.3(b) for embolus #3b, and Table 3.3(c) for embolus #3c. For all parameters, we used numbers that gave us the best agreement with experimental data. These fits are not expected to be perfect, because emboli are complex materials with varying compositions. Rather, the purpose of our model is to account for the general trends seen in the cyclic stress-strain response of emboli in terms of the stress-strain responses of the main constituents, which are the fibrin network and the RBCs.

(a) Emb. #1		σ_{pre}	E_L	l	K	ΔG	σ_{LH}	σ_{HL}	M_{LH}	M_{HL}	C_{neo}	f_{0,ϵ_i}	Fitting region
ϵ_1	Cycle 1	-0.25	0.9	3.75	10.48	10.12	0.08	-18	3.6	24	2.75	0.30	-
	Cycle 2	-0.35	0.7	4.00	10.48	10.12	0.08	-0.03	3.6	24	2.75	0.12	-
	Cycle 3	-0.40	0.4	4.25	10.48	10.12	0.08	-0.03	3.6	24	2.75	0.11	-
ϵ_2	Cycle 1	-0.40	0.4	4.75	10.48	10.12	0.08	-0.03	3.6	24	2.75	0.09	(0.65,0.8)
	Cycle 2	-0.40	0.4	6.75	9.68	9.39	0.08	-0.03	3.6	24	2.75	0.06	(0.65,0.8)
	Cycle 3	-0.40	0.4	6.75	5.41	5.24	0.08	-0.03	3.6	24	2.75	0.03	(0.65,0.8)
ϵ_3	Cycle 1	-0.40	0.4	6.75	5.41	5.24	0.08	-0.03	3.6	24	2.75	0.01	-
	Cycle 2	-0.40	0.4	8.75	5.41	5.24	0.08	-0.03	3.6	24	2.75	0.01	-

(b) Emb. #2		σ_{pre}	E_L	l	K	ΔG	σ_{LH}	σ_{HL}	M_{LH}	M_{HL}	C_{neo}	f_{0,ϵ_i}	Fitting region
ϵ_1	Cycle 1	0	0.9	2.75	11.12	10.86	0.08	-18	3.6	24	2.75	0.80	-
	Cycle 2	-0.2	0.7	3.00	11.12	10.86	0.08	-0.03	3.6	24	2.75	0.50	-
	Cycle 3	-0.2	0.4	3.25	11.12	10.86	0.08	-0.03	3.6	24	2.75	0.40	-
ϵ_2	Cycle 1	-0.4	0.4	3.35	11.12	10.86	0.08	-0.03	3.6	24	2.75	0.38	(0.69,0.8)
	Cycle 2	-0.4	0.4	3.40	11.26	11.02	0.08	-0.03	3.6	24	2.75	0.25	(0.69,0.8)
	Cycle 3	-0.4	0.4	3.45	11.30	11.07	0.08	-0.03	3.6	24	2.75	0.20	(0.69,0.8)
ϵ_3	Cycle 1	-0.4	0.4	3.50	11.30	11.07	0.08	-0.03	3.6	24	2.75	0.15	-
	Cycle 2	-0.4	0.4	3.55	11.30	11.07	0.08	-0.03	3.6	24	2.75	0.15	-

Table 3.2: Fitting parameters for (a) embolus #1 and (b) embolus #2. The three strain regions are $\epsilon_1 \in [0, 0.5]$, $\epsilon_2 \in [0.5, 0.8]$, and $\epsilon_3 \in [0.8, 0.92]$. σ_{pre} is the pre-stress in the network with units kPa , E_L is the Young's modulus in the rarefied phase with units kPa , l is the pore size with units $10^{-7}m$, K is the stress constant in the densified phase with units kPa , ΔG is the normalized bonding energy density with units kPa , σ_{LH} and σ_{HL} are nucleation stresses with units kPa , M_{LH} and M_{HL} are phase boundary mobilities with units $\frac{10^{-6}}{kPa \cdot s}$, C_{neo} is the RBC elasticity coefficient with units kPa , and $f_{0,\epsilon_i} = f_{0,\epsilon_{min} \leq \epsilon \leq \epsilon_{max}}$ is the initial fraction of RBCs for the strain region $[\epsilon_{min} \leq \epsilon \leq \epsilon_{max}]$ for $\epsilon_i \in \{\epsilon_1, \epsilon_2, \epsilon_3\}$. Also listed are the fitting regions of ϵ for the densified phase constants.

3.5.1 Phase boundary motion

The phase boundary, or transition front, between the densified region and rarefied region in the transition phase has been observed in compression experiments on blood clots formed from whole blood [63]. For emboli extracted from patients, however, it is significantly more difficult to observe. Our model reveals the location of the phase boundary, as can be observed for embolus #2 in Figure 3.8. In the strain region $\epsilon_1 \in [0, 0.5]$, the phase boundary appears and the transition region begins at higher strains for each subsequent loading cycle (see Figure 3.8). The phase boundary in the unloading cycle does not generally have to be at the same location as it was in the loading cycle because the stress carried by the network during loading is different from that during unloading (for example, fluid pumping does not contribute to the stresses during unloading). As such, the phase boundary may not return to the top of the embolus at the same strain at which it was originally manifest during the corresponding loading cycle. This is the case in the strain region $\epsilon_2 \in [0.5, 0.8]$, where the phase boundary is not in the same location after unloading to strain $\epsilon = 0.5$ as it was at the beginning of the loading in that cycle. Once again, the phase boundary also appears at higher

(a) Emb. #3a													
		σ_{pre}	E_L	l	K	ΔG	σ_{LH}	σ_{HL}	M_{LH}	M_{HL}	C_{neo}	f_{0,ϵ_i}	Fitting region
ϵ_1	Cycle 1	0	0.80	2.75	6.87	6.61	0.08	-18	3.6	24	2.75	0.40	-
	Cycle 2	0	0.75	3.00	6.87	6.61	0.08	-0.03	3.6	24	2.75	0.30	-
	Cycle 3	0	0.40	3.25	6.87	6.61	0.08	-0.03	3.6	24	2.75	0.28	-
ϵ_2	Cycle 1	-0.40	0.40	3.35	6.87	6.61	0.08	-0.03	3.6	24	2.75	0.20	(0.62,0.75)
	Cycle 2	-0.40	0.40	3.40	5.95	5.68	0.08	-0.03	3.6	24	2.75	0.10	(0.62,0.75)
	Cycle 3	-0.40	0.40	3.45	6.13	5.86	0.08	-0.03	3.6	24	2.75	0.10	(0.62,0.75)
ϵ_3	Cycle 1	-0.40	0.40	6.00	6.13	5.86	0.08	-0.03	3.6	24	2.75	0.02	-
(b) Emb. #3b													
		σ_{pre}	E_L	l	K	ΔG	σ_{LH}	σ_{HL}	M_{LH}	M_{HL}	C_{neo}	f_{0,ϵ_i}	Fitting region
ϵ_1	Cycle 1	0	0.90	2.50	11.52	11.01	0.08	-18	3.6	24	2.75	0.32	-
	Cycle 2	0	0.70	2.85	11.52	11.01	0.08	-0.03	3.6	24	2.75	0.22	-
	Cycle 3	0	0.40	3.00	11.52	11.01	0.08	-0.03	3.6	24	2.75	0.20	-
ϵ_2	Cycle 1	-0.40	0.40	4.50	11.52	11.01	0.08	-0.03	3.6	24	2.75	0.10	(0.62,0.75)
	Cycle 2	-0.40	0.40	4.55	12.75	12.23	0.08	-0.03	3.6	24	2.75	0.07	(0.62,0.75)
	Cycle 3	-0.40	0.40	4.60	12.95	12.45	0.08	-0.03	3.6	24	2.75	0.05	(0.62,0.75)
ϵ_3	Cycle 1	-0.40	0.40	4.75	12.95	12.45	0.08	-0.03	3.6	24	2.75	0.02	-
	Cycle 2	-0.40	0.40	4.75	12.95	12.45	0.08	-0.03	3.6	24	2.75	0.02	-
	Cycle 3	-0.40	0.40	4.75	12.95	12.45	0.08	-0.03	3.6	24	2.75	0.02	-
(c) Emb. #3c													
		σ_{pre}	E_L	l	K	ΔG	σ_{LH}	σ_{HL}	M_{LH}	M_{HL}	C_{neo}	f_{0,ϵ_i}	Fitting region
ϵ_1	Cycle 1	-0.08	0.90	1.75	18.10	17.27	0.08	-18	3.6	24	2.75	0.90	-
	Cycle 2	-0.08	0.70	2.00	18.10	17.27	0.08	-0.03	3.6	24	2.75	0.70	-
	Cycle 3	-0.08	0.40	2.25	18.10	17.27	0.08	-0.03	3.6	24	2.75	0.65	-
ϵ_2	Cycle 1	-0.40	0.40	2.25	18.10	17.27	0.08	-0.03	3.6	24	2.75	0.55	(0.62,0.75)
	Cycle 2	-0.40	0.40	2.50	15.76	15.04	0.08	-0.03	3.6	24	2.75	0.45	(0.62,0.75)
	Cycle 3	-0.40	0.40	2.50	14.87	14.20	0.08	-0.03	3.6	24	2.75	0.35	(0.62,0.75)
ϵ_3	Cycle 1	-0.40	0.40	4.75	14.87	14.20	0.08	-0.03	3.6	24	2.75	0.02	-
	Cycle 2	-0.40	0.40	4.75	14.87	14.20	0.08	-0.03	3.6	24	2.75	0.02	-
	Cycle 3	-0.40	0.40	4.75	14.87	14.20	0.08	-0.03	3.6	24	2.75	0.02	-

Table 3.3: Fitting parameters for (a) embolus #3a, (b) embolus #3b, and (c) embolus #3c. The three strain regions are $\epsilon_1 \in [0, 0.5]$, $\epsilon_2 \in [0.5, 0.75]$, and $\epsilon_3 \in [0.75, 0.92]$. σ_{pre} is the pre-stress in the network with units kPa , E_L is the Young's modulus in the rarefied phase with units kPa , l is the pore size with units $10^{-7}m$, K is the stress constant in the densified phase with units kPa , ΔG is the normalized bonding energy density with units kPa , σ_{LH} and σ_{HL} are nucleation stresses with units kPa , M_{LH} and M_{HL} are phase boundary mobilities with units $\frac{10^{-6}}{kPa \cdot s}$, C_{neo} is the RBC elasticity coefficient with units kPa , and $f_{0,\epsilon_i} = f_{0,\epsilon_{min} \leq \epsilon \leq \epsilon_{max}}$ is the initial fraction of RBCs for the strain region $[\epsilon_{min} \leq \epsilon \leq \epsilon_{max}]$ for $\epsilon_i \in \{\epsilon_1, \epsilon_2, \epsilon_3\}$. Also listed are the fitting regions of ϵ for the densified phase constants.

strains for each subsequent cycle (see Figure 3.8).

3.6 Discussion

A few general observations can be made from these tables. First, the pore size in the stress-free state becomes larger after each loading/unloading cycle. This is due to bundling of fibers and re-arrangement of embolus microstructure. Second, the Young's modulus in the rarefied phase decreases after the first few cycles of loading/unloading and then remains constant for subsequent cycles. This is due to re-arrangement of embolus microstructure and possible damage of the fibrin

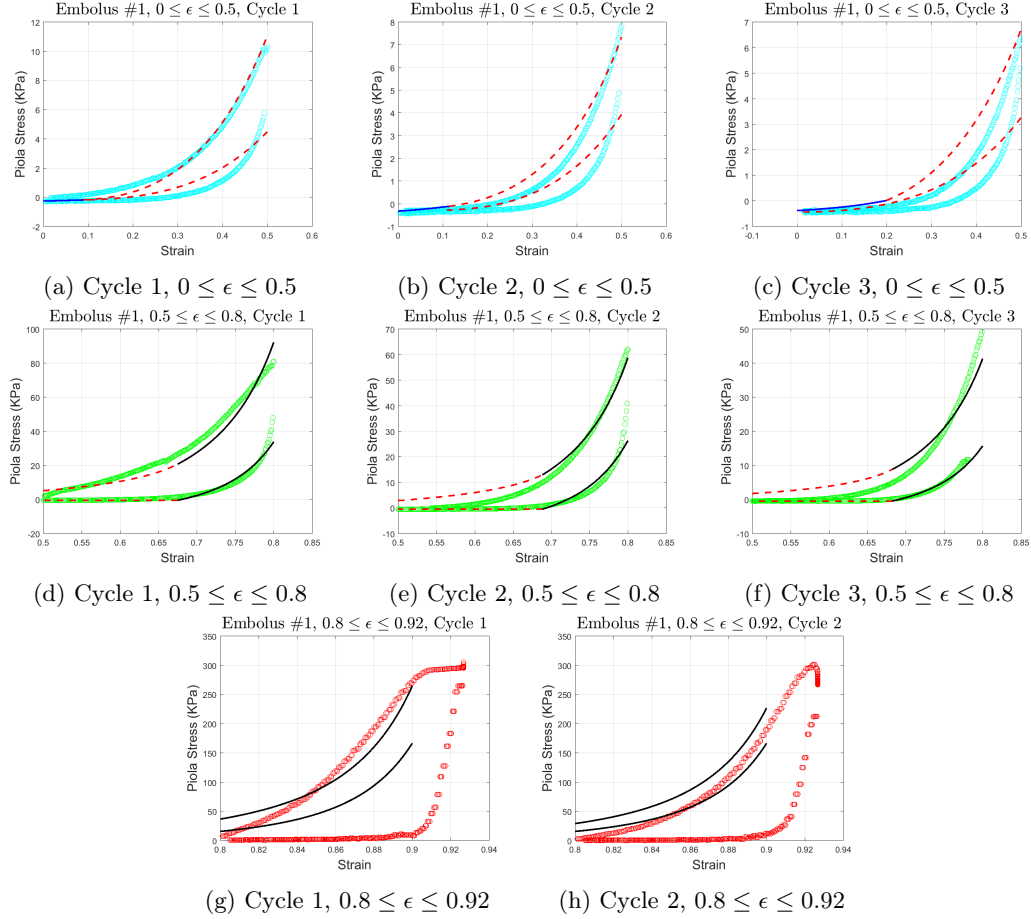


Figure 3.3: The stress-strain response of embolus #1 to compression and decompression for the regions $0 \leq \epsilon \leq 0.5$ ((a), (b), and (c)), region $0.5 \leq \epsilon \leq 0.8$ ((d), (e), and (f)), and region $0.8 \leq \epsilon \leq 0.92$ ((g) and (h)). The circles represent data points from the experiments, the solid blue lines represent the fully rarefied phase, the dashed red lines represent the transition phase, and the solid black lines represent the fully densified phase.

fibers comprising the network. Both of these observations are consistent with earlier work on the compression of whole blood clots, platelet-rich plasma clots and platelet-poor plasma clots [63].

There are also some differences between emboli and blood clots. First, in the early loading/unloading cycles, the contribution to stresses due to the deformation of the fibrin network is lower in emboli than it is in blood clots. This is because RBCs flow out of blood clots during compression, but are unable to escape through the smaller pores in the emboli. As a result, the stress in emboli is largely carried by the deformation of RBCs at low strains and by the pumping of liquid released by lysis of RBCs at higher strains. Second, the fraction of RBCs in emboli becomes smaller after each cycle of loading/unloading, because they are lysed due to the large deformations

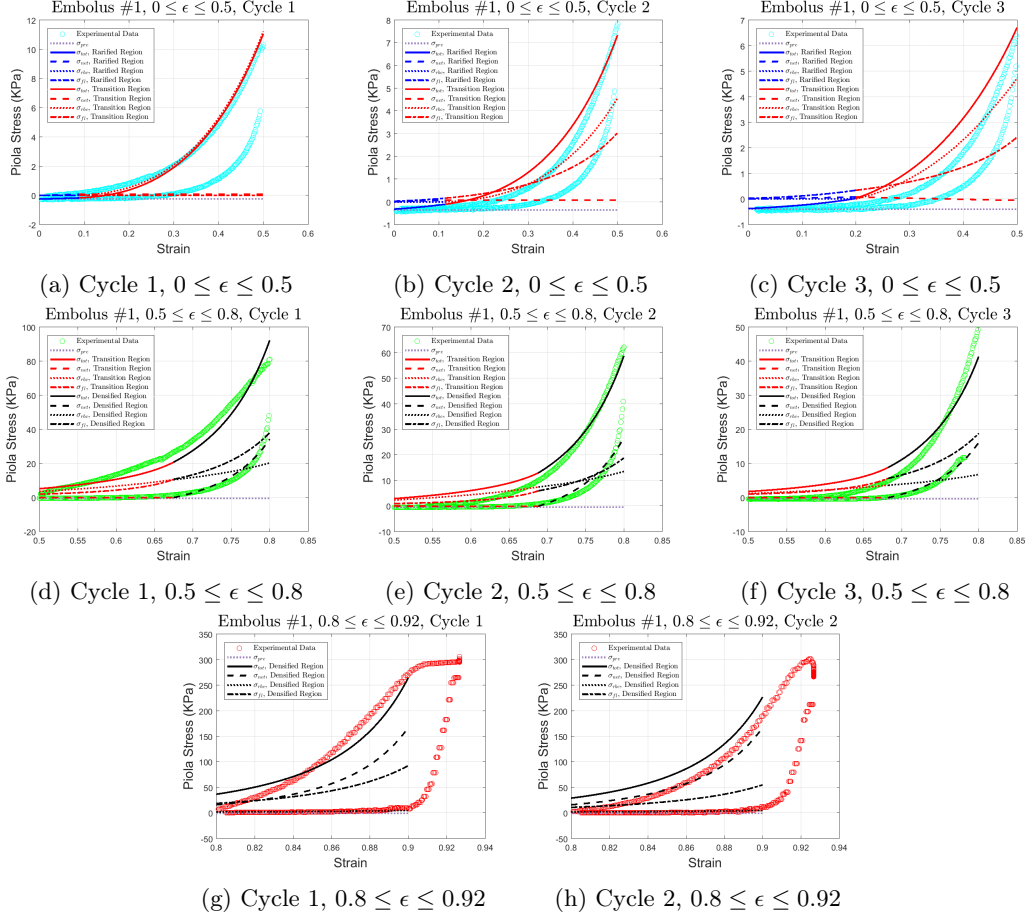


Figure 3.4: The contributions in the stress-strain response of embolus #1 to compression for the regions $0 \leq \epsilon \leq 0.5$ ((a), (b), and (c)), region $0.5 \leq \epsilon \leq 0.8$ ((d), (e), and (f)), and region $0.8 \leq \epsilon \leq 0.92$ ((g) and (h)). The circles represent data points from the experiments, the purple dotted lines represent the pre-stress, the solid lines represent the total stresses, the dashed lines represent the network contributions, the dotted lines represent the RBC contributions, and the dot-dashed lines represent the fluid contributions.

suffered. In contrast, in blood clots the RBCs that flowed out of the network under compressive loading were sucked back in during unloading, and their volume fraction does not change much after each loading/unloading cycle. Third, the phase boundary, or transition front, between the densified region and rarefied region in the transition phase has been observed in compression experiments on blood clots formed from whole blood [63]. For emboli extracted from patients, however, it is significantly more difficult to observe. Our model reveals the location of the phase boundary, as can be observed for embolus #2 in Figure 3.8. More details regarding the phase boundary and its motion are discussed in Section 3.5.1.

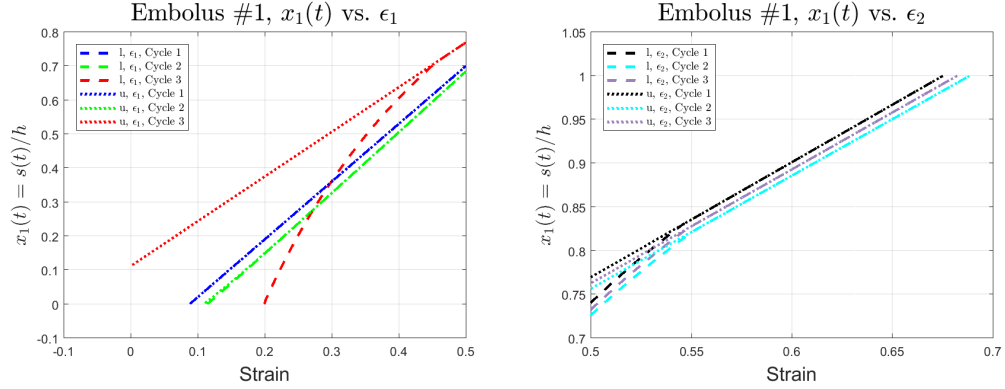


Figure 3.5: Phase boundary location for loading (l, dashed lines) and unloading (u, dotted lines) phases of embolus #1, cycles 1, 2, and 3 of strain regions $\epsilon_1 \in [0, 0.5]$ and $\epsilon_2 \in [0.5, 0.8]$.

3.6.1 Stress-strain curves

In the present *ex vivo* study, the mechanical response of pulmonary emboli to axial compression and passive decompression was experimentally measured, correlated with structural changes, and modeled. We observed directly for the first time that pulmonary emboli behave like foams (open soft network of fibers with pores) in response to compression and passive decompression, which is in agreement with prior work in which the compression responses of platelet-poor plasma clots, platelet-rich plasma clots, and whole blood clots was demonstrated [63]. The stress-strain curves of emboli for strains up to $\epsilon = 0.9$ for all cycles of the emboli revealed four characteristic portions for compression and passive decompression: for compression 1) linear regime in which the normal stress increased proportionally with increasing compressive strain, and 2) non-linear response as result of densification of the fibrin network and severe deformation/rupture of the RBCs; for the passive decompression portion of the cycle, 3) non-linear elastic region or re-stretching of the network, when normal stress dropped rapidly; 4) lowering strains further, the normal stress was rather insensitive to decompression because no external forces were applied, which resulted in a closed cycle. Stress-strain curves showed some similarity to those for blood clots formed *in vitro*; the same four linear and non-linear regimes are present [63]. However, for emboli there were no sudden changes in slope when the linear regime changed to non-linear for the compression and decompression parts of curves, as observed for all three types of blood clots formed *in vitro* in [63] in Figure 2. Those differences in mechanical response could be due to structural differences between clots formed *in vitro* compared to those formed *in vivo*.

An embolus that forms within a vessel and then travels to the lungs is a much more complicated

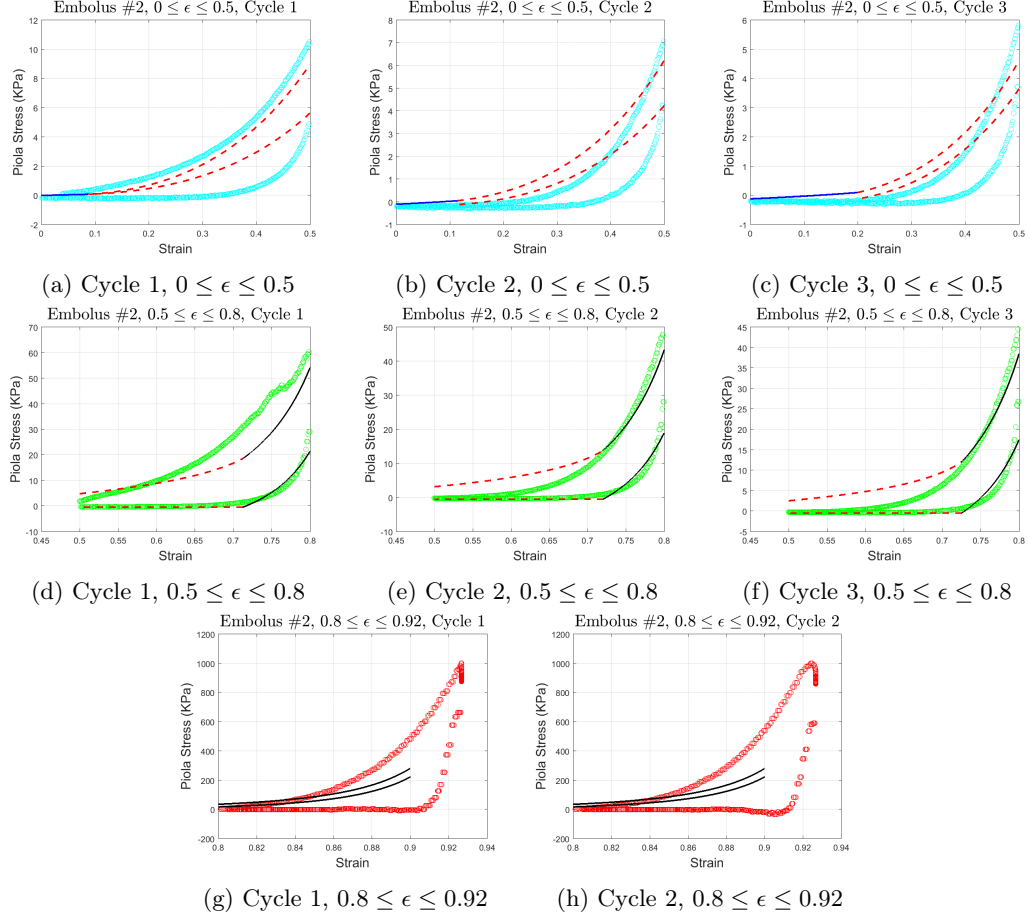


Figure 3.6: The stress-strain response of embolus #2 to compression and decompression for the regions $0 \leq \epsilon \leq 0.5$ ((a), (b), and (c)), region $0.5 \leq \epsilon \leq 0.8$ ((d), (e), and (f)), and region $0.8 \leq \epsilon \leq 0.92$ ((g) and (h)). The circles represent data points from the experiments, the solid blue lines represent the fully rarefied phase, the dashed red lines represent the transition phase, and the solid black lines represent the fully densified phase.

structure than a clot formed *in vitro* [151]. Clots formed *in vitro* have a foam-like structure with open space of more than 50% due to the space not occupied by RBCs, white blood cells, and platelets that are incorporated into the fibrin mesh, whereas clots formed *in vivo* are denser, with less than 1% open space. These differences in structure may contribute to the observed smooth transition without a sudden change in slope from the linear to the non-linear regime in the mechanical response. In addition, sudden changes in slope were not observed in the decompression part of the curve, due to differences in experimental conditions [63]. Here, we observed passive decompression, since the emboli were not attached to rheometer plates, as were the clots in our previous work. Therefore, we could only measure the mechanical response from the elastic energy that was accumulated in the

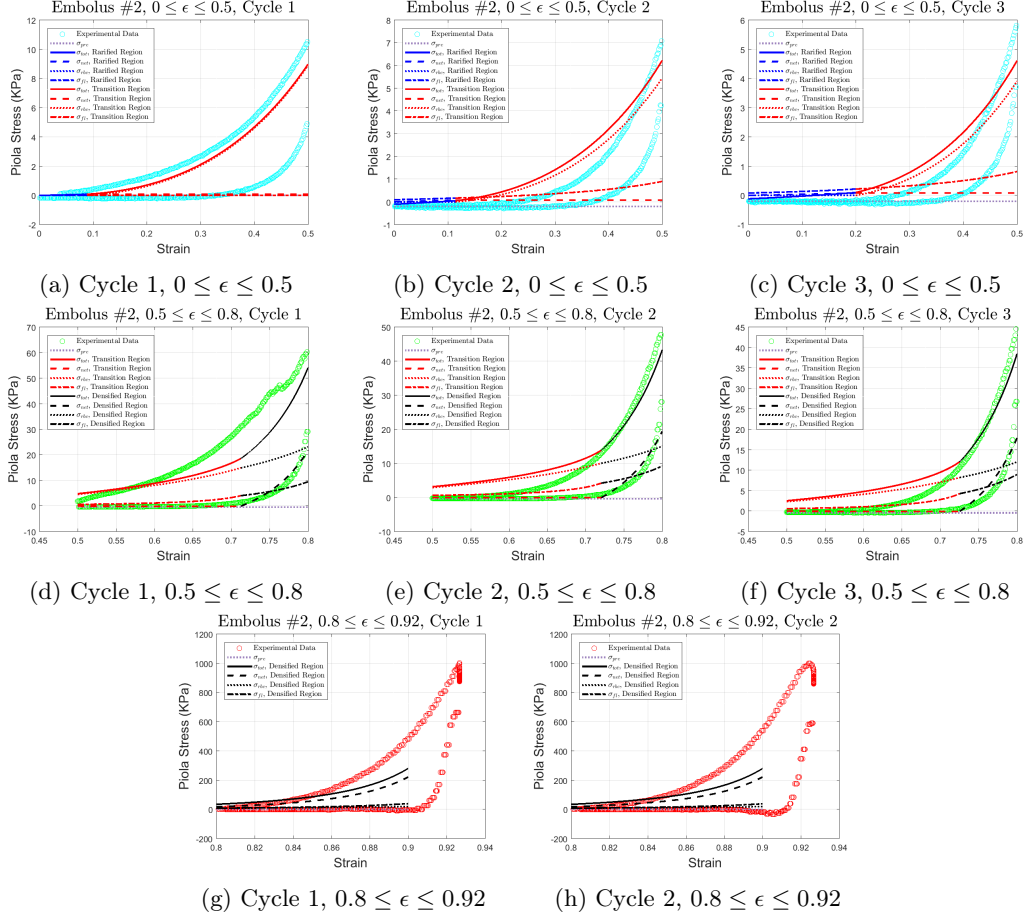


Figure 3.7: The contributions in the stress-strain response of embolus #2 to compression for the regions $0 \leq \epsilon \leq 0.5$ ((a), (b), and (c)), region $0.5 \leq \epsilon \leq 0.8$ ((d), (e), and (f)), and region $0.8 \leq \epsilon \leq 0.92$ ((g) and (h)). The circles represent data points from the experiments, the purple dotted lines represent the pre-stress, the solid lines represent the total stresses, the dashed lines represent the network contributions, the dotted lines represent the RBC contributions, and the dot-dashed lines represent the fluid contributions.

emboli during compression, because no direct forces could be applied to return the embolus to its original thickness. This response may be more physiological, since it mimics the mechanical response when a thrombus within a blood vessel responds to forces of blood flow or vessel wall contraction.

3.6.2 Repeated compression-decompression cycles

All emboli were subjected to three loading and unloading cycles for 3 sets of compressive strains: $0 \leq \epsilon \leq 0.5$; $0.5 \leq \epsilon \leq 0.75$ or $0.5 \leq \epsilon \leq 0.8$, and $0.75 \leq \epsilon \leq 0.9$ or $0.8 \leq \epsilon \leq 0.9$. We found that the stress-strain curves of the first cycle differed from those of the second and third cycles for all sets

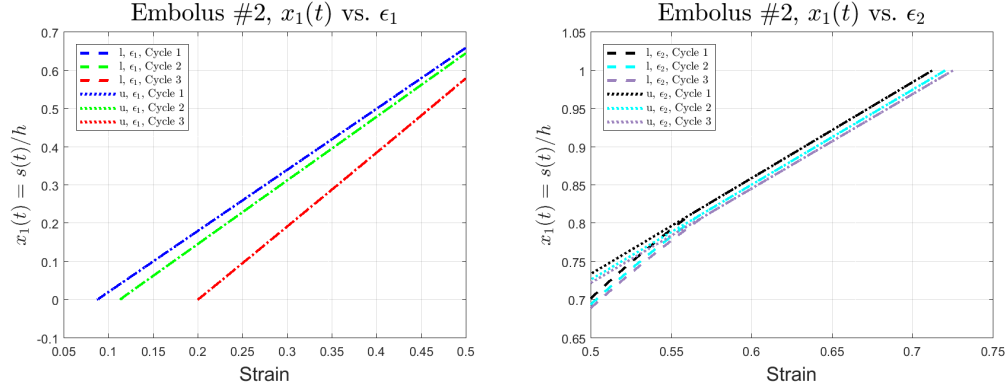


Figure 3.8: Phase boundary location for loading (l, dashed lines) and unloading (u, dotted lines) phases of embolus #2, cycles 1, 2, and 3 of strain regions $\epsilon_1 \in [0, 0.5]$ and $\epsilon_2 \in [0.5, 0.8]$.

of compression strains. Compression and decompression do not follow the same pathway, meaning that the stress-strain behavior of pulmonary emboli exhibits a hysteresis loop upon cyclical loading, as a result of the dissipation of energy.

This effect has also been previously observed in compression/decompression of blood clots formed *in vitro* as well as for carbon nanotube forests [63, 152]. These findings indicate that there were structural changes in the emboli, some of which were reversible and others irreversible, as shown before for platelet-poor, platelet-rich and whole blood clots formed *in vitro*. During compression, the presence of fiber bundles increased, the pore size decreased, fibers become aligned, and the network density increased. As compression proceeds, the fibrin network is densified, as fibers criss-cross and increasingly bundle. Moreover, RBCs escape from the fibrin network during the compression part of the cycle and some are sucked back in during the decompression part of the cycle. Since the embolus has become distorted by irreversible changes in the network, such as smaller pore size and fibrin fibers alignment, the RBCs must fit into new spaces that are now more compact and aligned due to fibrin fiber and bundle alignment. These structural changes resulted in shape transformation of some RBCs from biconcave to polyhedral or polyhedral with orientation, as a result of fibrin network alignment. During decompression, some fibers unbundle while others stay associated, resulting in new clot structures after compression/decompression cycles. As a result, not all RBCs return back into the embolus during passive decompression. Therefore, every new cycle of compression/decompression starts with an embolus with changed structures. In addition, some RBC deformation is reversible, but RBC breakage is irreversible, so those cells do not participate in the subsequent mechanical responses.

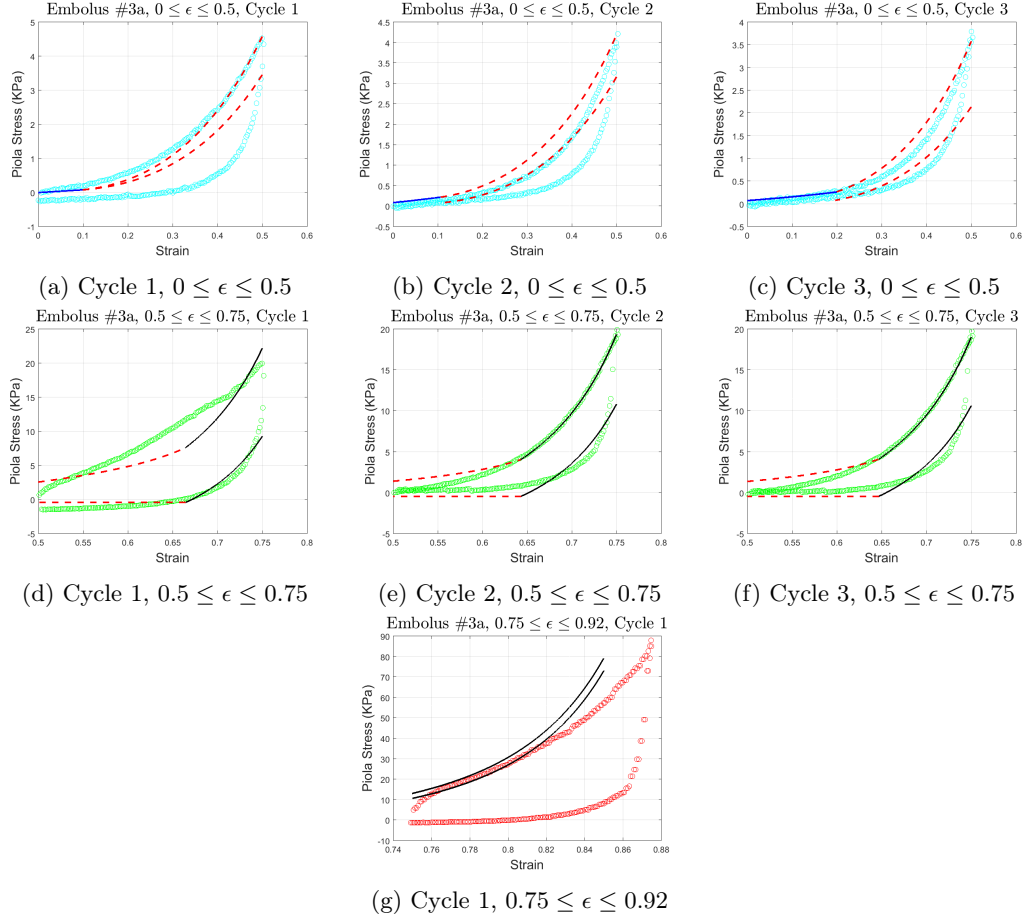


Figure 3.9: The stress-strain response of embolus #3a to compression and decompression for the regions $0 \leq \epsilon \leq 0.5$ ((a), (b), and (c)), region $0.5 \leq \epsilon \leq 0.75$ ((d), (e), and (f)), and region $0.75 \leq \epsilon \leq 0.92$ ((g)). The circles represent data points from the experiments, the solid blue lines represent the fully rarefied phase, the dashed red lines represent the transition phase, and the solid black lines represent the fully densified phase.

3.6.3 Response structural dependence

We demonstrated that variations in the composition of emboli can lead to quantitatively different normal stress-strain responses. Emboli with high fibrin content demonstrate higher normal stress compared to emboli that have high RBC content. This finding agrees with *in vitro* results, where it was demonstrated that increasing fibrinogen concentration dramatically increased the normal stress but increasing RBC concentration did not much affect the normal stress, because they start to rupture at higher stresses [1].

The mechanical response of emboli depends on the relative proportions of fibrin and RBCs. Under compression, fibrin fibers and RBCs may undergo large deformation without rupture. For

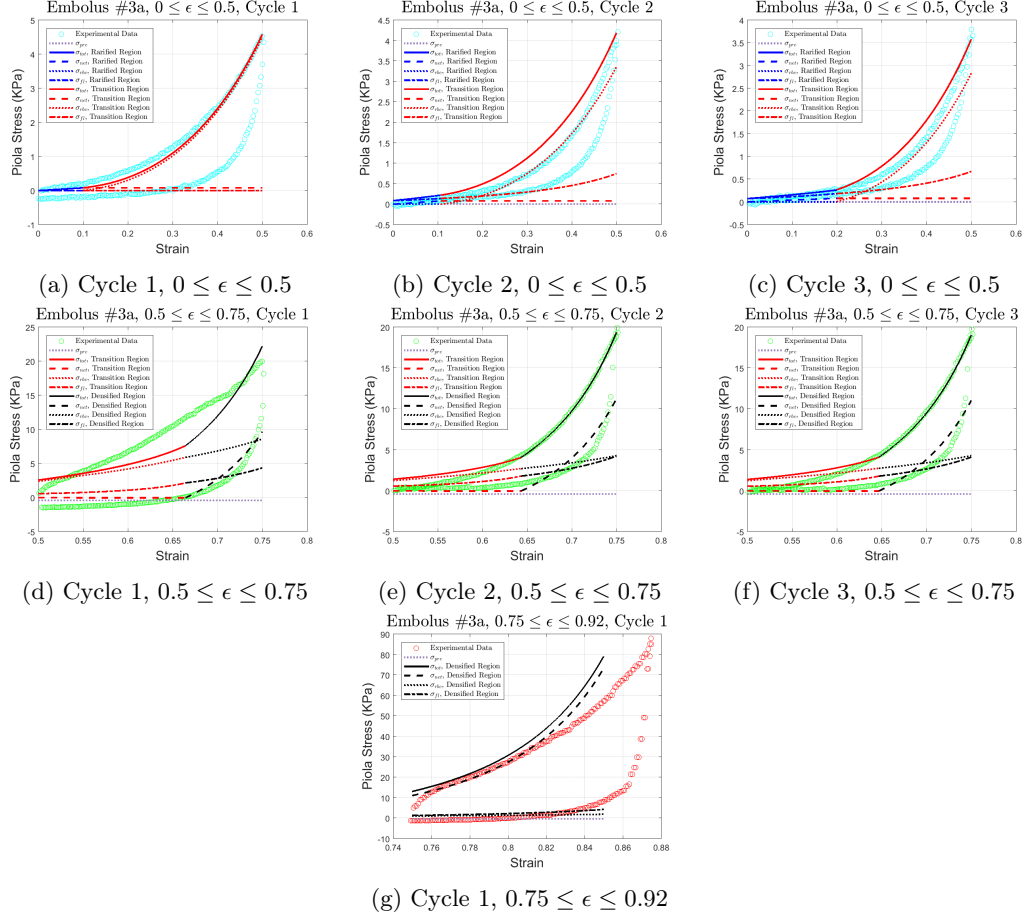


Figure 3.10: The contributions in the stress-strain response of embolus #3a to compression for the regions $0 \leq \epsilon \leq 0.5$ ((a), (b), and (c)), region $0.5 \leq \epsilon \leq 0.75$ ((d), (e), and (f)), and region $0.75 \leq \epsilon \leq 0.92$ ((g)). The circles represent data points from the experiments, the purple dotted lines represent the pre-stress, the solid lines represent the total stresses, the dashed lines represent the network contributions, the dotted lines represent the RBC contributions, and the dot-dashed lines represent the fluid contributions.

example, RBCs change shape from normal biconcave to polyhedral and may return to their original shape following decompression [63, 153]. Compression of emboli caused some RBCs to be squeezed out, due to their flexibility, in agreement with results from compression of whole blood clots [63].

3.6.4 Comparison of different emboli

Recall that embolus #1 has initial and final heights and cross-sectional areas $h = 5.3mm$, $h_f = 0.5mm$, $A_0 = 158.8mm^2$, and $A_f = 1489mm^2$, respectively, and the fitting parameters are listed in Table 3.2(a). Embolus #2 has $h = 2.56mm$, $h_f = 0.2mm$, $A_0 = 131.2mm^2$, and

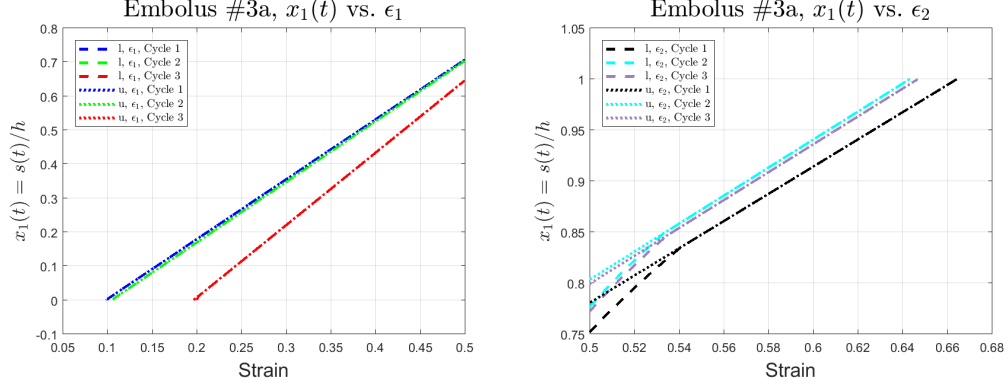


Figure 3.11: Phase boundary location for loading (l, dashed lines) and unloading (u, dotted lines) phases of embolus #3a, cycles 1, 2, and 3 of strain regions $\epsilon_1 \in [0, 0.5]$ and $\epsilon_2 \in [0.5, 0.75]$.

$A_f = 313.7mm^2$, and the fitting parameters are listed Table 3.2(b). Multiplying through, embolus #1 has initial volume $V_0 = 841.64mm^3$ and final volume $V_f = 744.5mm^3$, whereas embolus #2 has $V_0 = 335.87mm^3$ and $V_f = 62.74mm^3$. The fraction of volume change in embolus #2 $\Delta V/V_0 = 0.81$ is significantly higher than $\Delta V/V_0 = 0.12$ in embolus #1, suggesting that the initial volume fraction of RBCs ($f_{0,0 \leq \epsilon \leq 0.5}$ in cycle 1) in embolus #2 is significantly higher than in embolus #1. This is consistent with our fitting parameters in Table 3.2 which have been obtained solely from the stress-strain curves. A higher $f_{0,0 \leq \epsilon \leq 0.5}$ in cycle 1 means that the proportion of stress carried by the RBCs (than that carried by the network) in embolus #2 is larger than embolus #1. This trend is confirmed when we look at the stress-strain plots of embolus #1 and embolus #2 in Figure 3.4 and Figure 3.7, where the contributions of network, RBCs, and fluids are plotted separately.

3.6.5 Heterogeneity of emboli

Although our model treats thrombi as being homogeneous, thrombi are not necessarily so, especially large thrombi. Embolus #3, for example, is clearly heterogeneous. Recall that embolus #3 was cut into three sections (a, b, and c), each of which was treated individually, and that the stress-strain responses of sections a, b, and c were measured and fitted separately. Embolus #3a has $h = 2.60mm$, $h_f = 0.33mm$, $A_0 = 120.81mm^2$, and $A_f = 266.4mm^2$. Embolus #3b has $h = 2.80mm$, $h_f = 0.35mm$, $A_0 = 74mm^2$, and $A_f = 383mm^2$. Embolus #3c has $h = 2.23mm$, $h_f = 0.28mm$, $A_0 = 177.4mm^2$, and $A_f = 236mm^2$. Multiplying through, embolus #3a has $V_0 = 313.56mm^3$, $V_f = 86.58mm^3$, and $\Delta V/V_0 = 0.72$, embolus #3b has $V_0 = 206.51mm^3$, $V_f = 134.15mm^3$, and $\Delta V/V_0 = 0.35$, and embolus #3c has $V_0 = 394.97mm^3$, $V_f = 65.98mm^3$, and $\Delta V/V_0 = 0.83$. The

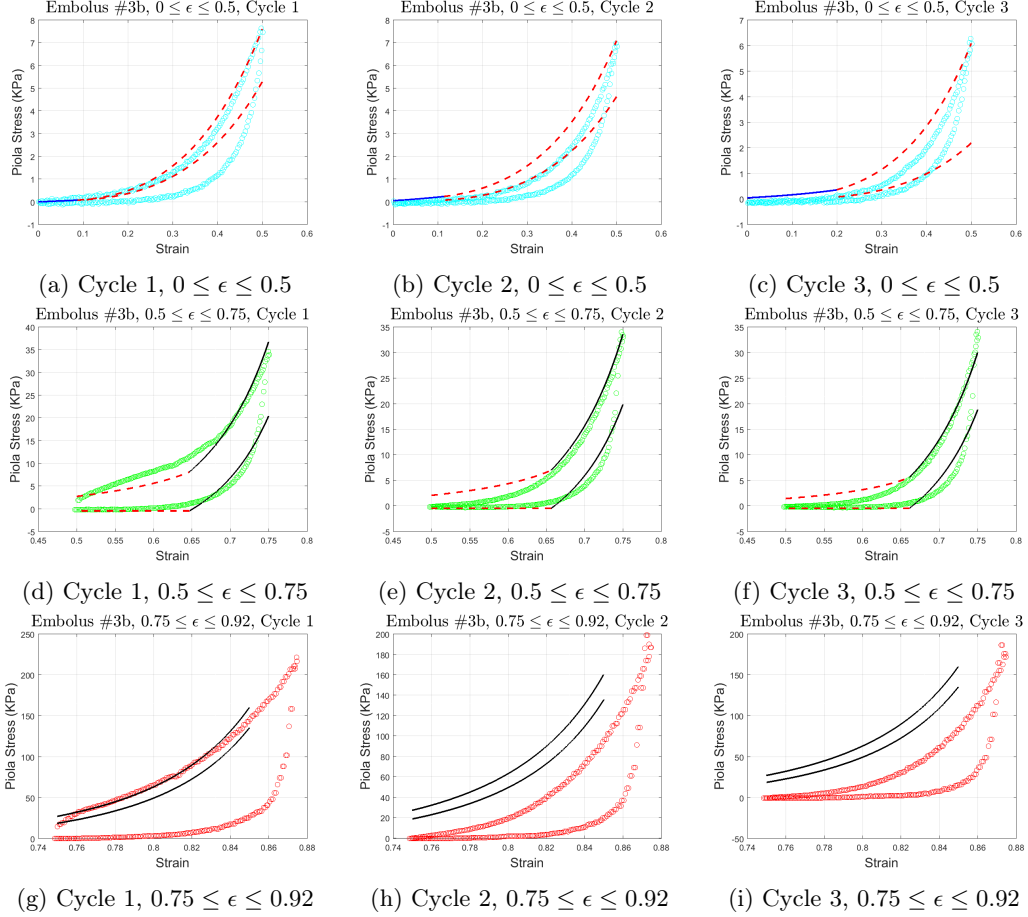


Figure 3.12: The stress-strain response of embolus #3b to compression and decompression for the regions $0 \leq \epsilon \leq 0.5$ ((a), (b), and (c)), region $0.5 \leq \epsilon \leq 0.75$ ((d), (e), and (f)), and region $0.75 \leq \epsilon \leq 0.92$ ((g), (h), and (i)). The circles represent data points from the experiments, the solid blue lines represent the fully rarefied phase, the dashed red lines represent the transition phase, and the solid black lines represent the fully densified phase.

fitting parameters for embolus #3a can be found in Table 3.3(a), for embolus #3b in Table 3.3(b), and for embolus #3c in Table 3.3(c). From the volume changes and the fits, it is clear that each piece of embolus #3 is different. The fraction of volume change of embolus #3b is relatively small, as is the case in embolus #1, whereas the fraction of volume changes in embolus #3a and embolus #3c are large, as is the case in embolus #2. Accordingly, $f_{0,0 \leq \epsilon \leq 0.5}$ in cycle 1 is higher in embolus #3a and embolus #3c than in embolus #3b (see Table 3.3).

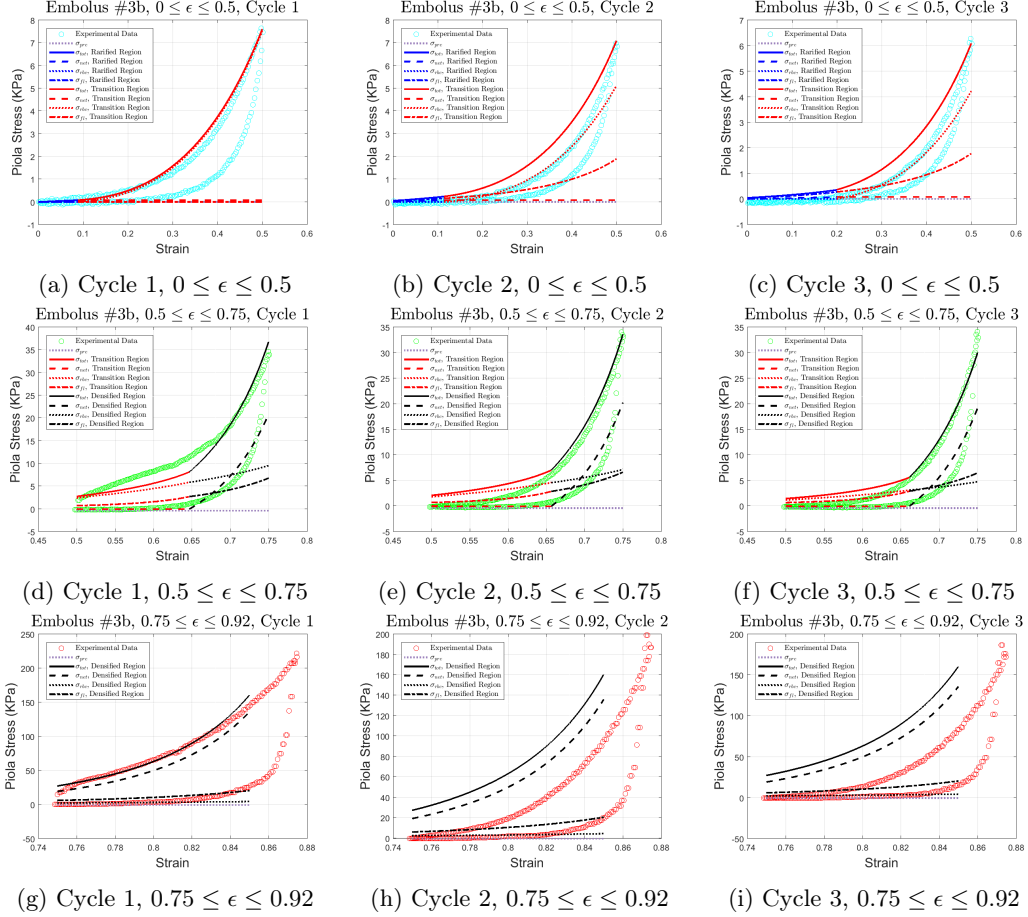


Figure 3.13: The contributions in the stress-strain response of embolus #3b to compression for the regions $0 \leq \epsilon \leq 0.5$ ((a), (b), and (c)), region $0.5 \leq \epsilon \leq 0.75$ ((d), (e), and (f)), and region $0.75 \leq \epsilon \leq 0.92$ ((g), (h), and (i)). The circles represent data points from the experiments, the purple dotted lines represent the pre-stress, the solid lines represent the total stresses, the dashed lines represent the network contributions, the dotted lines represent the RBC contributions, and the dot-dashed lines represent the fluid contributions.

3.6.6 Comparisons with other studies

Some relevant studies in the literature will be mentioned here but more may be found in a recent review of research on the mechanical behavior of clots and thrombi based on experimental, analytical, and computational methods [154]. Uniaxial and biaxial tensile tests on thrombi have been reported [136–138, 155, 156], comparisons of *ex vivo* thrombi and *in vitro* thrombus models [50, 154, 157], shear testing of *ex vivo* thrombi [158], *in vitro* thrombus models [159], and compression testing of *in vitro* thrombus models [44, 139, 140, 144, 160], and for *ex vivo* thrombi [139, 140, 161]. Linear models [105, 155, 158], nonlinear continuum models [137, 144, 158, 159], and computational methods

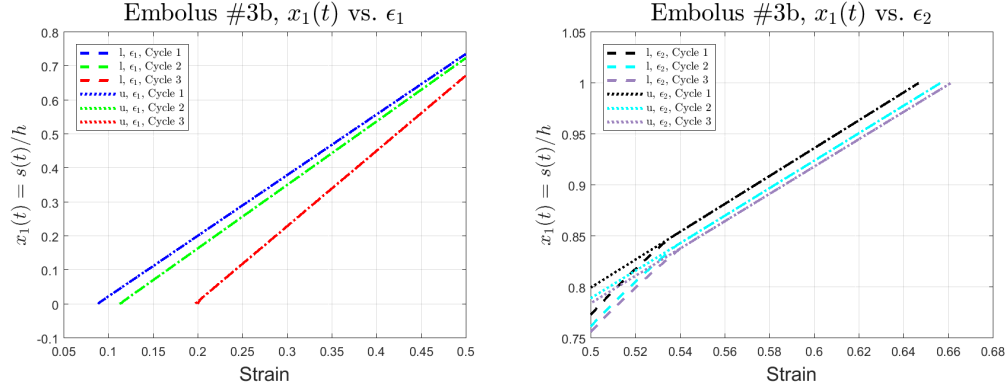


Figure 3.14: Phase boundary location for loading (l, dashed lines) and unloading (u, dotted lines) phases of embolus #3b, cycles 1, 2, and 3 of strain regions $\epsilon_1 \in [0, 0.5]$ and $\epsilon_2 \in [0.5, 0.75]$.

[136, 156, 160] have been used to interpret data from various experiments.

While tensile strength of fibrin networks is important in the context of fibrin’s use as a biomaterial, and shear oscillatory forces occur due to blood flow, thrombi *in vivo* are primarily subject to compressive forces due to the compression of vascular walls by surrounding musculature. Our compression experiments differ from previous compression tests of *in vitro* thrombi since we extracted natural *in vivo* emboli, which have much smaller pore sizes than artificial *in vitro* thrombi because they have already undergone clot contraction (see [1] Supplementary Material Figure 1). This structural difference also allows RBCs to flow out from artificial *in vitro* thrombi, but not from our natural *ex vivo* emboli, since the pores are too small. Our compression tests differ from some others [139, 140, 161] in the following ways: they studied differences between thrombi, including aged vs. red, calcified vs. non-calcified, and thrombi from different species, using force-controlled experiments. Although they apply large strains (up to 95%) and get nonlinear stress-strain curves, they do not provide a mathematical model to identify the mechanisms that lead to stresses due to these deformations. In contrast, we do provide such a mathematical framework. Ashton *et al.* recognized that thrombi are heterogeneous, as they discuss three layers of thrombi that have different compositions and different mechanical behaviors [140]. These authors treat the thrombi as linear viscoelastic materials, but they only studied small strains. They also prepared mimics of thrombi varying the levels of fibrinogen, thrombin and calcium, but do not discuss the mechanical effects of RBCs, fluid flow, and clot contraction caused by platelets [140]. Xie *et al.* focused on aged thrombi, discussed the compression geometry, and primarily compared ultrasound measurements to those from their compressive device while carefully accounting for friction between the device plates and

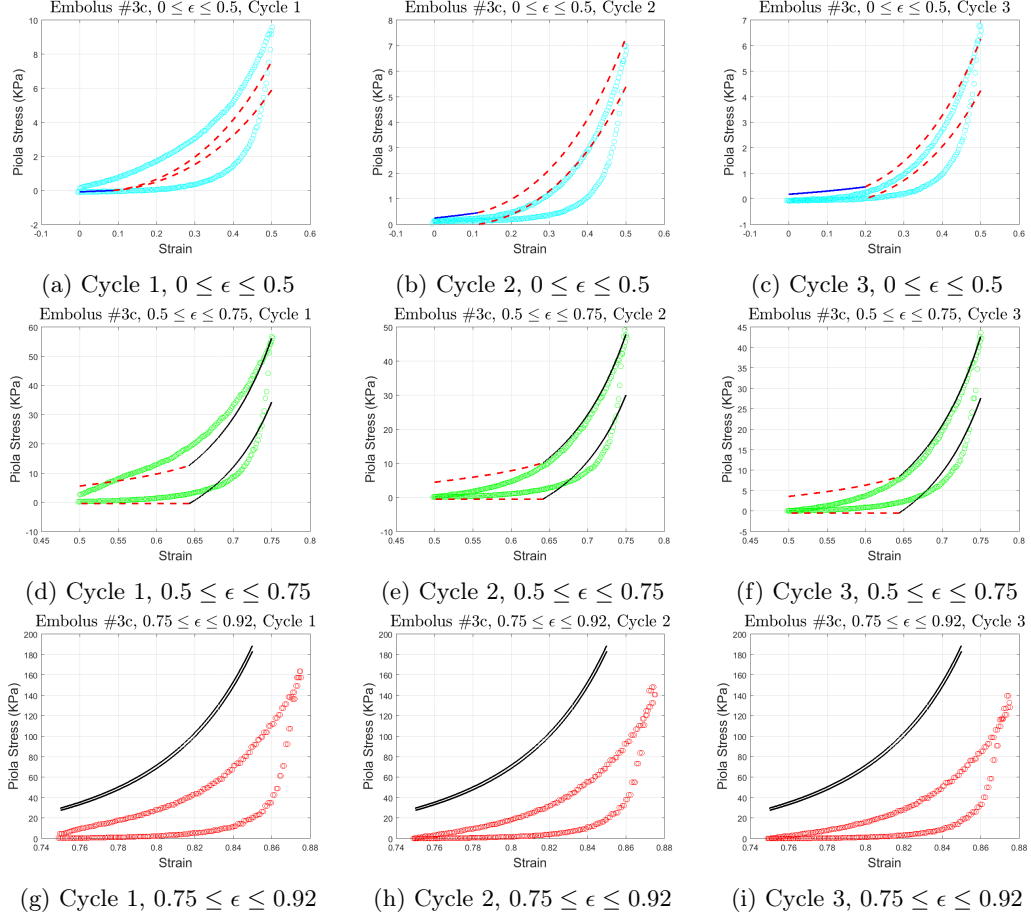


Figure 3.15: The stress-strain response of embolus #3c to compression and decompression for the regions $0 \leq \epsilon \leq 0.5$ ((a), (b), and (c)), region $0.5 \leq \epsilon \leq 0.75$ ((d), (e), and (f)), and region $0.75 \leq \epsilon \leq 0.92$ ((g), (h), and (i)). The circles represent data points from the experiments, the solid blue lines represent the fully rarefied phase, the dashed red lines represent the transition phase, and the solid black lines represent the fully densified phase.

the sample [161]. However, they confine their studies to small strains and therefore do not comment on the densification of the sample. That being said, the moduli obtained in all these studies were in the kPa range, validating our results.

Our model differs from previously published models in a number of ways. Firstly, even though some other previous models considered poroelasticity and viscoelasticity [144, 156, 158–160], our model also includes a phase change from the linear rarefied phase to the nonlinear densified phase with a propagating interface. Thus, we identify phase boundary propagation as another source of dissipation in addition to dissipation caused by fluid flow and the viscoelastic nature of the network. Next, even aforementioned nonlinear models assume the thrombi are incompressible, isotropic, and

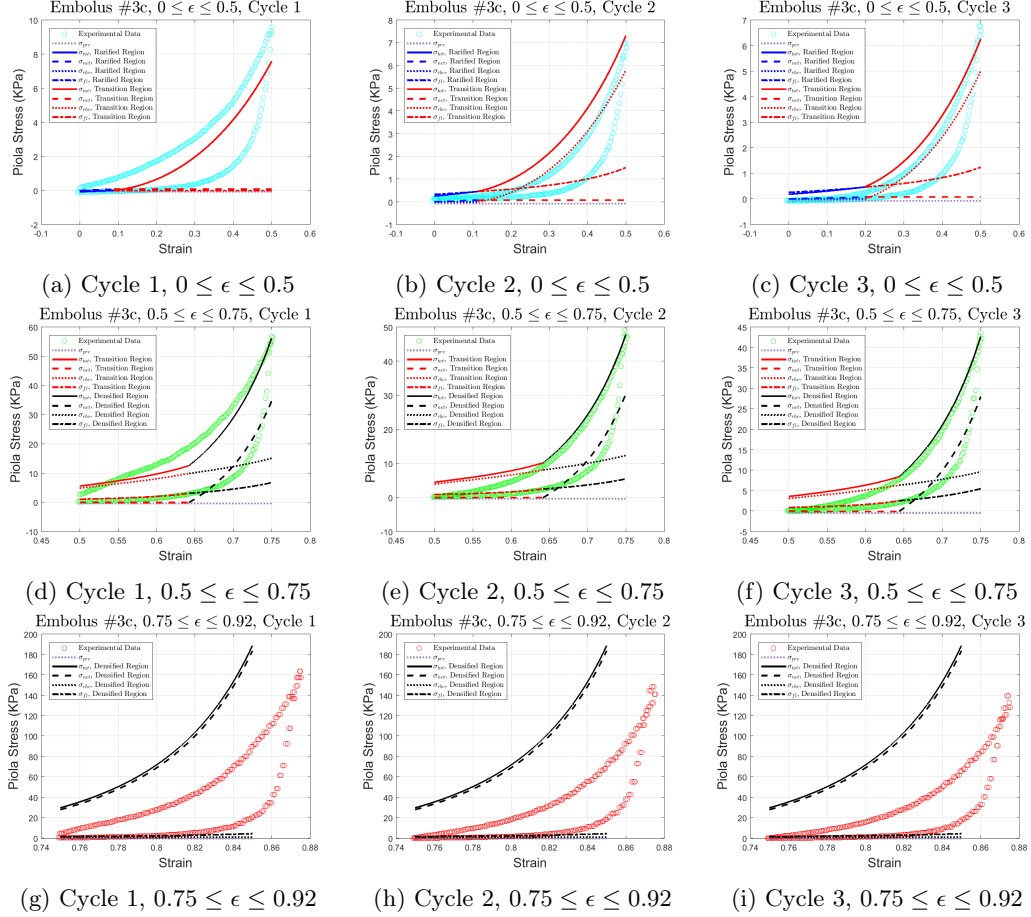


Figure 3.16: The contributions in the stress-strain response of embolus #3c to compression for the regions $0 \leq \epsilon \leq 0.5$ ((a), (b), and (c)), region $0.5 \leq \epsilon \leq 0.75$ ((d), (e), and (f)), and region $0.75 \leq \epsilon \leq 0.92$ ((g), (h), and (i)). The circles represent data points from the experiments, the purple dotted lines represent the pre-stress, the solid lines represent the total stresses, the dashed lines represent the network contributions, the dotted lines represent the RBC contributions, and the dot-dashed lines represent the fluid contributions.

homogeneous, whereas we recognize that some of these assumptions do not always hold. Liquid is forced out during compression, thus making the thrombi compressible. Additionally, since the two phases coexist [44], thrombi are not truly homogeneous under applied loads; in fact, we have shown that different regions of the same embolus (embolus #3) may have different mechanical properties. Furthermore, it has been shown that densified emboli have fibers predominantly aligned in a plane perpendicular to the compression direction [44], so emboli are not isotropic under loads. Finally, our model accounts for the primary microscopic components (fibrin network, RBCs, fluid) of the emboli separately, instead of considering the entire embolus as one uniform material, better describing emboli of different component concentrations. Also similar to some models that track

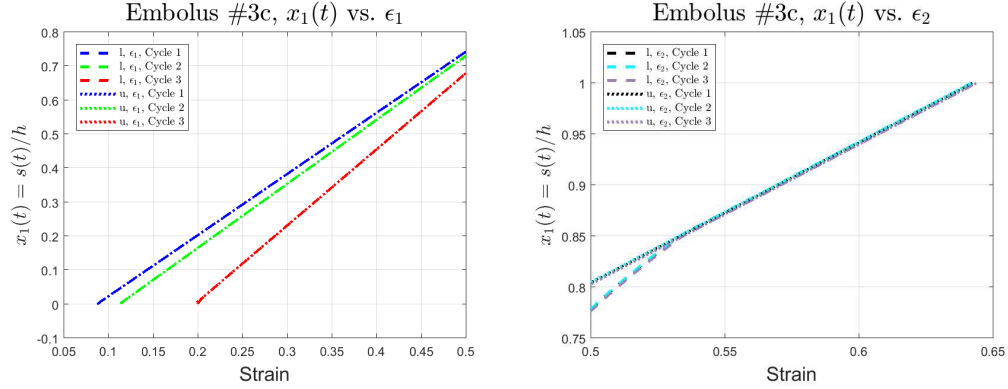


Figure 3.17: Phase boundary location for loading (l, dashed lines) and unloading (u, dotted lines) phases of embolus #3c, cycles 1, 2, and 3 of strain regions $\epsilon_1 \in [0, 0.5]$ and $\epsilon_2 \in [0.5, 0.75]$.

damage evolution [162], we track how the moduli, pore size, etc., evolve from one cycle to the next, although we do not give specific quantitative expressions for the evolution.

3.6.7 Implications

Thrombi *in vivo* undergo dramatic deformations under (patho) physiological conditions such as hydrodynamic blood shear, contraction of platelets, and contraction of surrounding muscle tissue. Therefore, the outcomes of many thrombotic disorders, including deep vein thrombosis, other venous thrombosis, and embolization, are largely determined by the mechanical behavior of thrombi. Here we have shown that emboli share some similarities with whole blood clots, such as similar hysteretic stress-strain response to cyclic compression, but also differ from them in important ways. The pore size in thrombi is smaller than that in blood clots, thus their mechanical behavior is strongly influenced by the presence of RBCs that cannot escape under compression.

Thromboemboli represent a unique biological material that has some unusual mechanical properties that have implications for the pathophysiology of deep vein thrombosis and other thrombotic conditions. This new information may be important for understanding the response of thrombi to compressive forces and to predicting the likelihood of embolization, which is the most serious consequence of deep vein thrombosis, as well as embolization in the arterial system resulting in stroke.

Although there are some structural differences between pulmonary emboli and their parent deep vein thrombi, they are similar in structure and thus similar in mechanical properties. The response of deep vein thrombi to compression is important for the design and use of thrombectomy or even

ultrasound devices for removal of these thrombi. The fact that our model accounts for general trends seen in cyclic stress- strain response of emboli in terms of fibrin and RBC content means it can help in classifying emboli as rich in fibrin or rich in red blood cells, and can help in understanding what responses to expect when stresses are applied by removal devices to thrombi *in vivo*. The results here provide a basis for making such devices that work more effectively because they are based on the real compressive responses of the thrombi.

3.7 Conclusions

Here we characterized the mechanical response of pulmonary emboli to cyclic compression while simultaneously tracking changes in their structure. We observed directly for the first time that pulmonary emboli behave like foams (open soft network of fibers with large pores) in response to compression and passive decompression.

Stress-strain curves for all pulmonary emboli revealed four portions. The compression part of curve has the following regions: 1) linear regime in which normal stress increases proportionally with increasing compressive strain, and 2) non-linear response as result of rapid upturn in normal stress. The passive decompression part of curve has the following regions: 3) non-linearly elastic region or re-stretching of the network, in which normal stress dropped rapidly; 4) at lower strains, the normal stress was rather insensitive to decompression, reflecting a linear response to strain and resulting in a closed cycle. Thus, compression and decompression do not follow the same pathway, meaning that the stress- strain behavior of pulmonary emboli exhibits a hysteresis loop upon cyclic loading, indicating the dissipation of energy. We described this behavior using a continuum theory of phase transitions, which acknowledges that within a range of compressive stresses the fibrin network of the embolus can have co-existing rarefied and densified phases. The fibers are mostly straight in the rarefied phase, while they are significantly bent with a number of contacts in the densified phase. The fractions of each phase change as the embolus is compressed or decompressed. The fibrin fibers and RBCs are damaged during the compression process, causing irreversible changes in the structure of the emboli.

We showed that the stress response of emboli depends on their structure. Variations in the composition of emboli can lead to quantitatively different normal stress-strain responses. Emboli with a high fibrin component demonstrate higher normal stress compared to emboli that have a high

RBC component.

Understanding these nuances in mechanical properties of emboli will garner a deeper understanding of thromboembolisms and therapeutic disintegration and removal of intravascular thrombi using mechanical means such as ultrasound, aspiration, and mechanical thrombectomy.

Chapter 4

Humidity Dependence of Fracture Toughness of Cellulose Fibrous Networks

This chapter is based on work published in [163] R. Spiewak, G. S. Vankayalapati, J. M. Considine, K. T. Turner, and P. K. Purohit. “Humidity dependence of fracture toughness of cellulose fibrous networks”, *Engineering Fracture Mechanics*, **264**: 108330, (2022). DOI:10.1016/j.engfracmech.2022.108330.

Abstract

Cellulose-based materials are increasingly finding applications in technology due to their sustainability and biodegradability. The sensitivity of cellulose fiber networks to environmental conditions such as temperature and humidity is well known. Yet, there is an incomplete understanding of the dependence of the fracture toughness of cellulose networks on environmental conditions. In the current study, we assess the effect of moisture content on the out-of-plane (i.e., z-dir.) fracture toughness of a particular cellulose network, specifically Whatman cellulose filter paper. Experimental measurements are performed at 16% RH along the desorption isotherm and 23, 37, 50, 75% RH along the adsorption isotherm using out-of-plane tensile tests and double cantilever beam (DCB) tests. Cohesive zone modeling and finite element simulations are used to extract quantitative properties that describe the crack growth behavior. Overall, the fracture toughness of filter paper decreased with increasing humidity. Additionally, a novel model is developed to capture the high peak and sudden drop in the experimental force measurement caused by the existence of an initiation region. This model is found to be in good agreement with experimental data. The relative effect of each independent cohesive parameter is explored to better understand the cohesive zone-based humidity dependence model. The methods described

here may be applied to study rupture of other fiber networks with weak bonds.

4.1 Introduction

Cellulose is an abundantly available polymer in nature. Cellulose networks have good mechanical [72, 73] and barrier [74] properties. Filter paper is a network consisting of pure cellulose fibers bound to each other mechanically by entanglement and chemically by hydrogen bonds. The cellulose fibers are flattened hollow tubes, typically 25–35 micrometers wide with thicknesses of 1 to 4 micrometers. When the paper is loaded in tension, permanent deformation occurs through the breaking of inter-fiber bonds (namely, a surface area of multiple hydrogen bonds connecting two fibers) [75, 76] and removal of microcrimps. These cellulose networks can fail when subjected to tensile loads during manufacture or in successive operations. It has been demonstrated [77] that these failures generally occur due to rapid propagation of cracks from pre-existing flaws, such as notches or creases. On account of the presence of a stress concentration around a flaw, the stress at which failure occurs is well below the strength of an un-flawed sheet, thus making fracture toughness, the ability of cellulose networks to resist crack growth, an important performance parameter to be studied.

Previous work in the application of fracture mechanics to paper has been carried out by Wani-garatne [164], Tryding et al. [165] and Zechner et al. [166]. Work of fracture methods that were developed to estimate the fracture toughness of ductile materials have been applied to paper [167, 168]. Atomistic modeling of cellulose networks has also been used to shed light on the fracture of paper [169]. There are some works using cohesive zone modeling to model the fracture of paper, including [166, 170–172]. Zechner et al. [166] developed a method combining images from experiments with cohesive zone modeling to reliably determine the crack tip, and therefore also the fracture initiation toughness value, of commercial printing paper. Mao et al. [170] used a cohesive zone model to describe the fracture behavior of notched cellulose nanopaper, commercial printing paper, and buckypaper. Makela and Ostlund [171] studied fracture of copy paper along combinations of machine- and cross-directions, also utilizing a cohesive zone model. Meng et al. [172] modeled fracture of cellulose nanofibril network papers using cohesive zone properties derived from the potential energy differences during fiber pullout at the interfaces between hydrogen bonds at a molecular scale. These previous works have shown that cohesive zone modeling is an effective technique to estimate the fracture toughness of cellulose networks, which otherwise cannot be evaluated accurately as these

networks exhibit a nonlinear and ductile fracture behavior, but no work has been done extending this technique to study the influence of humidity on these networks.

The macroscale behavior of fibrous networks, in general, depends on the properties of the fibers and the bonds between the fibers; the effects of microscale fiber properties on macroscale material behavior have been studied in networks of random fibers [21, 25, 29–31] and of fibers with cellular shapes [25, 26, 28], using large scale finite element simulations. Since fibrous networks generally perform structural functions, their macroscale mechanical properties such as fracture toughness are of critical importance. Network rupture has been studied in [21] by allowing the bonds connecting the fibers to fail in tension as well as shear through finite element simulations of three-dimensional isotropic random fiber networks. However, while it is true that fibrous materials can be three-dimensionally isotropic, they are also often found as sheets which are orthotropic in nature. It is difficult to identify the z-direction properties of thin web orthotropic materials, so fracture studies of such materials are few. Since cellulose papers are a common two-dimensional fibrous network we use it as a vehicle to develop methods to characterize fracture toughness of such materials.

Additionally, as mentioned previously, rupture has been studied in [21] in generalized three-dimensional random fibrous networks by allowing the bonds connecting the fibers to fail. The resulting stress-stretch curves show an initial positive slope which decreases to zero as more bonds break, then the slope of the stress-stretch curve becomes negative and the stress ultimately goes to zero. This resembles traction-separation laws used in cohesive-zone modeling, which account for damage accumulation. Similar stress-strain curves were obtained by [173], who studied mechanics of random fiber networks using stochastic breaking of bonds.

The properties of paper in the thickness direction (i.e., z-direction), although not necessary for conventional paper use and difficult to measure since the characteristic length scales are of the same order of magnitude as the fibrous microstructure of the material, are needed to extend the use of paper for novel applications such as in the fabrication of piezoelectric cellulose sheets and batteries [174–177]. Moreover, the information about the out-of-plane properties of paper are helpful in studying scoring, folding and 3-D forming operations.

Earlier works of measuring the mechanical properties of paper in the z-direction are few [178–181]. Nygard et al. [179] used a double notch shear (DNS) test to measure the out-of-plane shear strength of paperboard. The DNS test is advantageous because of its ability to overcome the potential drawbacks arising from the conventional out-of-plane tests which require the paper to be

glued between rigid blocks. Ostlund et al. [178] developed experimental techniques to measure the out-of-plane normal and shear properties of paperboard using an extended double notch shear test.

Humidity is an important parameter that can significantly affect the mechanical properties of cellulose networks. Increases in environmental humidity increases the moisture content in the paper and in turn reduces the stiffness of the fibers and the number of fiber-fiber bonds, and thus lead to mechanical changes of the overall network. The effect of humidity on the mechanical and fracture properties of paper is important during converting operations and use by consumers.

Many studies have examined the effect of humidity on the tensile properties of cellulose networks [5, 8, 9, 15, 182–188]. Gamstedt et al. [9] and Celino et al. [8] reviewed works involving moisture-induced softening and swelling of plant and natural cellulose fiber composites. Placet et al. [183] found that water sorption showed a significant influence on the tensile properties and fracture mode of cellulose-based hemp fibers. Alamri et al. [15] investigated cellulose-reinforced epoxy composites at two different humidities and found that strength, modulus, and fracture toughness decreased as a result of moisture absorption. Benitez et al. [184], and Meng et al. [185] also observed decrease in modulus, strength and tensile toughness of cellulose nanopaper sheets with the increase of relative humidity as a result of easier interfacial debonding between cellulose nanofibers (CNFs), which they attribute to moisture induced bond weakening. Benitez et al. [184] also showed a clear transition of the fracture mechanism of cellulose nanopaper network from brittle to pull-out phenomena when varied between 0 and 100% RH. Moropoulou et al. [186] reported a decrease in the tensile strength of filter paper with increase in moisture content and also showed the hysteresis effect of adsorption and desorption. Nissan et al. [5] explored the effect of moisture on the Young’s modulus of hydrogen bond dominated solids like paper, and also established an empirical relation between the modulus and moisture content. Of all the aforementioned earlier works involving both pure cellulose (micro and nano) networks and cellulose-based composites, the effect of humidity on the fracture toughness of porous cellulose networks has not been studied.

The objectives of this work are to characterize the z-direction properties using tensile tests and out-of-plane fracture of filter paper (a porous 100% cellulose network) as a function of moisture content using a double cantilever beam (DCB) specimen and model the fracture properties using cohesive zone modeling. Continuum cohesive zone models provide the convenience of tuning a few parameters such as peak stress and separation at failure to model one-dimensional fracture propagation. Use of cohesive zone models also allows us to bypass expensive finite element simulations of discrete

fiber networks which require the specification of a host of parameters for the fibers and bonds. For these reasons, and since we do not have control over individual fiber and fiber-fiber bonds properties in cellulose networks, we describe the fracture behavior through continuum traction-separation laws.

The paper is organized as follows: In Section 4.2 and Section 4.3, we discuss the materials, methods, and theory used in this study. The results of the experiments and simulations, and related discussion, is provided in Section 4.4. Finally, the main conclusions are discussed in Section 4.5.

4.2 Materials and Methods

4.2.1 Materials

Commercial poly(methyl methacrylate) (PMMA) sheets (Curbell Plastics, Inc.), hydrophobic in nature [189], with thickness 2.85 – 3.05 mm were used as the top and bottom beams of the DCB. GE Whatman Grade-1 Filter Paper (Sigma Aldrich Inc.) with a nominal thickness of 170 micrometers is the cellulose network that is studied. Whatman filter paper was chosen since its manufacturing process is well established, so the properties of commercially available Whatman paper are relatively consistent. Additionally, Whatman filter paper is 100% cellulose, thicker, and weaker than commercial copy paper, so there is a greater chance of the crack propagating entirely through the paper and not shifting to an interface. Copy paper also contains inorganic materials to increase brightness and surface smoothness. The filter paper was bonded to the PMMA beams using Loctite 409 (McMaster Inc.). The thickness of the adhesive layer was carefully controlled to ensure that it did not fully infiltrate the paper layer (details below).

4.2.2 Conditioning and Specimen Preparation

If the relative humidity (RH) approaches a particular value from a lower RH (adsorption), the paper contains less water than if approached from a higher value (desorption). This hysteresis is well known in the paper industry. Since the direction from which a particular RH is approached plays an important role, it is a standard practice to convert relative humidity to moisture content. Here, the humidities 23%, 37%, 50%, and 75% are approached along an adsorption isotherm and 16% RH is achieved along a desorption isotherm. The filter paper specimens were conditioned for 48 hours at every humidity at room temperature before measuring the mass of the specimens. These paper specimens were then adhered to the PMMA substrates and left in the humidity chamber for another

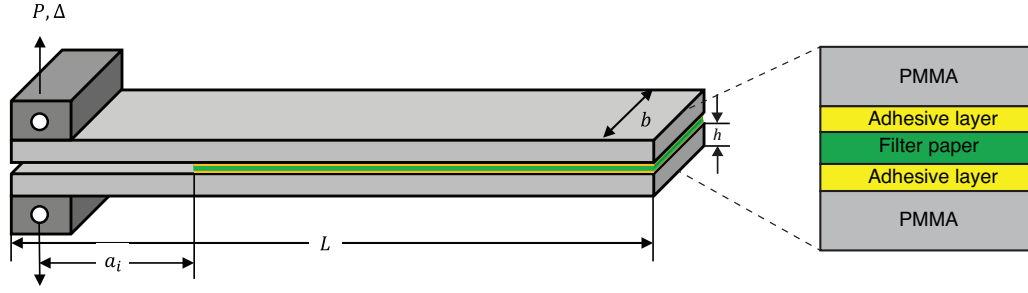


Figure 4.1: Schematic of the DCB specimen in this study.

48 hours before testing. The dry weight of the specimens was measured by placing the filter papers in a vacuum oven at 50°C for 48 hours. Moisture content is measured as Eq. (4.1).

$$mc = \frac{m_w - m_d}{m_d} * 100 \quad (4.1)$$

where m_d is the mass of the dry specimen, m_w is the mass of filter paper specimens at a particular RH, and mc is the moisture content.

The PMMA beams that used in the DCB have a width of 9.5-10 mm and length of 70 mm. The beams are laser cut (Universal Laser PLS 4.75 flatbed laser cutter) from PMMA sheets of thickness 2.85-3.05 mm. After multiple trials using multiple adhesives and epoxies, thin pressure sensitive adhesives, and a thick 3M VHB tape, 70% wt./wt. Loctite 409 in acetone was determined to be the optimum composition of the adhesive to bond filter paper and the PMMA beams. This particular adhesive solution was strong enough to hold the filter paper between the two beams, thin enough to not penetrate into the filter paper, and sufficiently stiff to not deform meaningfully and affect measurements. An adjustable thin film coating applicator (Futiantian Technology Co., Ltd., China) is used to generate adhesive coatings of thickness 10 micrometers on PMMA surfaces. Samples were scrutinized both under optical microscope and SEM images to verify that the adhesive did not penetrate into the filter paper. An initial crack of length $a_i \approx 27\text{mm}$ is obtained by placing the filter paper at a distance of 30 mm from the beginning between the beams (see Figure 4.1).

4.2.3 Out-of-plane Tensile Test

Cellulose fibrous networks have out-of-plane modulus and strength typically an order of magnitude (or two) less than the in-plane properties. Filter paper is held in between two aluminum loading blocks using double-sided Norton polyurethane foam tape (1mm thick). The aluminum blocks (5mm \times 5mm) are mounted onto the machine using single pin joints on the top and bottom to help with self-correcting any misalignment during the test. Peak stress/traction of filter paper in the out-of-plane direction is calculated from the maximum measured force during the test. A uniaxial testing machine in displacement control (Criterion Model 43, MTS) was used for all mechanical testing. A displacement rate of 1mm/min is used in the tests. Since most of the displacement applied deforms the foam tapes, optical measurements were performed (on the machine direction (MD) edge of the specimen) to measure the initial strain; from this strain and the measured stress the modulus was calculated. The tests are recorded at 30 frames per second, and up to 200 frames are used to calculate strain (eg. strain at 200th frame = 4.2 \pm 1.0 %). The images were converted to grayscale images and line profiles of pixel intensity were extracted at 4 different locations to measure deformation of the paper during the test. The width at the average half peak intensity was measured in all images and used to calculate strain by comparing the average thickness to the one from the first frame.

4.2.4 Double Cantilever Beam Testing

Double cantilever beam (DCB) tests were performed to determine the out-of-plane fracture toughness of the filter paper when the crack runs in the machine direction (MD). A displacement rate of 1 mm/min is used in all the tests. The load is applied to loading blocks adhered to the PMMA beams. From the loading cycle, the applied load versus displacement curve was obtained, and the crack length a and the strain energy release rate G were calculated using the following equations obtained by modifying (for different beam and foundation materials) the augmented double cantilever approach by Kanninen [190]:

$$a = \left(\frac{CE'bh^3}{8} \right)^{\frac{1}{3}} - \xi \quad (4.2)$$

$$G = \frac{12P^2a^2}{E'b^2h^3} \left(1 + \xi \frac{1}{a} \right)^2 \quad (4.3)$$

$$\xi = \left(\frac{h^3h_f E'}{6 E_f} \right)^{\frac{1}{4}}, \quad (4.4)$$

where h is the thickness of each PMMA beam, b is the width of the beam, E' is the plane-strain modulus of the beam, h_f is the thickness of the Whatman paper foundation material, E_f is the out-of-plane modulus of the Whatman paper foundation material, C is the compliance of the elastic specimen measured from the force-displacement curve, and P is the applied load.

4.3 Theory and Calculations

4.3.1 Cohesive Zone Model, Traction-Separation Law, Critical Energy Release Rate, and Non-Dimensional Parameter

Cohesive zone models have been shown to be effective at describing adhesion and fracture at material interfaces [191, 192]. Since we have a thin sample of cellulose material in which the crack moves straight ahead in a one-dimensional manner, we use cohesive zone models to study crack propagation in our Whatman filter paper specimens.

The specimen and loading conditions were designed to maintain mode I fracture and to prevent shear loading at the interface. As such, the shear stress is negligible, and only the normal traction t_n must be considered. Therefore, similar to the derivation in [192], from initial stress until final failure, there are two regions characterized by the presence or absence of damage: the opening region before damage initiation, and the softening region after damage initiation until final failure. In the opening region the traction-separation law is linear-elastic:

$$t_n = K_n \delta_n, \quad (4.5)$$

where K_n is the stiffness in the normal direction and δ_n is the displacement. Once the traction reaches the critical value t_n^0 at displacement $\delta_n^0 = t_n^0/K_n$, damage initiation occurs. Then, in the softening region, the damage evolves as the traction predicted by the traction-separation law in the linear-elastic region multiplied by the damage parameter $(1 - D)$. With a linear damage parameter

$$(1 - D) = \left(\frac{\delta_n^0}{\delta_n} \right) \left(\frac{\delta_n^f - \delta_n}{\delta_n^f - \delta_n^0} \right), \quad (4.6)$$

where δ_n^f is the normal displacement to failure, the traction-separation law in the softening region

becomes

$$t_n = K_n \delta_n^0 \left(\frac{\delta_n^f - \delta_n}{\delta_n^f - \delta_n^0} \right). \quad (4.7)$$

Thus, the complete traction-separation law with linear softening is

$$t_n = \begin{cases} K_n \delta_n, & 0 \leq \delta_n \leq \delta_n^0, \\ K_n \delta_n^0 \left(\frac{\delta_n^f - \delta_n}{\delta_n^f - \delta_n^0} \right), & \delta_n \geq \delta_n^0 \end{cases}, \quad (4.8)$$

where

$$\delta_n^0 = \frac{t_n^0}{K_n}, \quad (4.9)$$

with the following parameters: t_n^0 , the critical normal traction, peak stress, or cohesive strength of the cellulose network; K_n , the normal stiffness; and δ_n^f , the displacement to failure.

With an exponential damage parameter

$$(1 - D) = \left(\frac{\delta_n^0}{\delta_n} \right) \left(1 - \frac{1 - \exp \left[-\alpha \left(\frac{\delta_n - \delta_n^0}{\delta_n^f - \delta_n^0} \right) \right]}{1 - \exp(-\alpha)} \right), \quad (4.10)$$

where δ_n^f is once again the normal displacement to failure and α is the exponential parameter, the traction-separation law in the softening region becomes

$$t_n = K_n \delta_n^0 \left(1 - \frac{1 - \exp \left[-\alpha \left(\frac{\delta_n - \delta_n^0}{\delta_n^f - \delta_n^0} \right) \right]}{1 - \exp(-\alpha)} \right). \quad (4.11)$$

Thus, the complete traction-separation law with exponential softening is

$$t_n = \begin{cases} K_n \delta_n, & 0 \leq \delta_n \leq \delta_n^0 \\ K_n \delta_n^0 \left(1 - \frac{1 - \exp \left[-\alpha \left(\frac{\delta_n - \delta_n^0}{\delta_n^f - \delta_n^0} \right) \right]}{1 - \exp(-\alpha)} \right), & \delta_n \geq \delta_n^0 \end{cases}, \quad (4.12)$$

where the parameters t_n^0 , K_n , and δ_n^f are the same as in the traction-separation law with linear softening (Eq. (4.8)), and α is the exponential parameter governing the shape of the exponential softening.

The toughness, or critical energy release rate, is the area under the traction-separation law curve and it can be expressed in terms of the previously defined parameters as [193–196]:

$$G_{Ic} = \int_0^{\delta_c} t_n d\delta_n. \quad (4.13)$$

Consistent with previous work [192, 197], a non-dimensional parameter (NDP) is constructed to enable comparison between materials:

$$NDP = \frac{E_{PMMA} G_{Ic}}{(t_n^0)^2 h}. \quad (4.14)$$

The NDP is a measure of the toughness of a material: the lower the NDP , the tougher the material.

4.3.2 Finite element analysis

Finite element (FE) modeling and analysis was used to find the force-displacement curves corresponding to the cohesive parameters of different relative humidities. FE analysis was performed using the commercial software ABAQUS\Standard (Dassault Systèmes Simulia Corp) using a 2D plane strain model. The PMMA beams have length 67 mm and height 2.86 mm , and the Whatman filter paper has length 40 mm and height $171 \text{ }\mu\text{m}$. The Whatman filter paper region was aligned with the free end of the PMMA rectangular regions to give a pre-crack length of 27 mm (see Figure 4.2). Displacement controlled vertical loading was applied at the top and bottom corners of the PMMA beams (see Figure 4.2), and the inner corners of the PMMA beams are fixed in the horizontal direction. The PMMA beams were modeled as CPE4 plane strain elements, with Young’s modulus 2.016 GPa to include both the contribution from the PMMA itself and the layer of Loctite adhering the Whatman filter paper to the PMMA beams, and Poisson’s ratio $\gamma = 0.4$ (see Figure 4.3 for a brief discussion of element types). The Whatman filter paper was modeled as a single row of COH2D4 cohesive elements with material properties captured by the cohesive parameters. The mesh was refined closer to the COH2D4 cohesive elements, and through a mesh convergence study, the number of elements in the mesh was selected to be approximately 22,000. This method of using cohesive elements with uniform properties is a standard technique to model the fracture of materials.

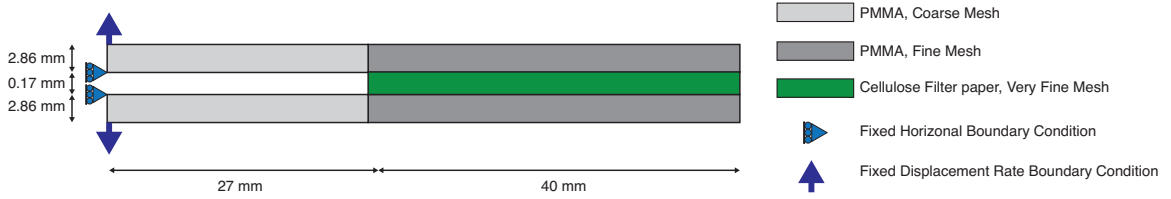


Figure 4.2: Diagram of the part, partitions, and mesh density used in the finite element simulations. Also depicted are the length and height dimensions (not drawn to scale), as well as the locations of the loading (purple arrows) and fixed boundary (blue triangles) conditions.

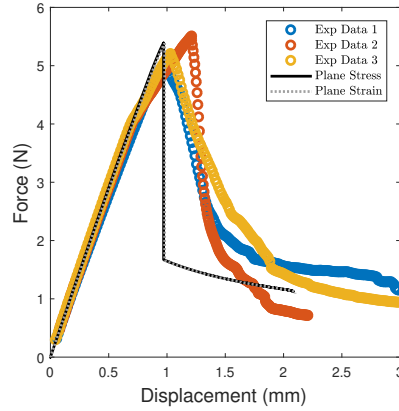


Figure 4.3: Comparison of experimental results and simulations using both plane stress CPS4 and plane strain CPE4 elements to represent the PMMA beams. The plane strain element CPE4 in ABAQUS is, according to the ABAQUS documentation, a special case of plane stress element CPS4. The modifications ABAQUS makes include modifying the input Young's modulus E to use the effective plane strain modulus $E' = E/(1-\nu^2)$. Therefore, as expected, results are identical for plane stress CPS4 and plane strain CPE4 elements, when using the modified input modulus $E'' = E(1-\nu^2)$ for the plane strain CPE4 elements, where E is the modulus for the plane stress CPS4 elements.

4.4 Results and Discussion

4.4.1 Experimental Critical Energy Release Rate

Force versus displacement data obtained from the loading of DCB specimens is used to calculate crack length a and energy release rate G from the compliance model using modified beam theory given by Eq. (4.2) and Eq. (4.3). Figure 4.4 shows an example force-displacement curve and G_C as a function of the crack length a calculated from this curve. G is not defined when $a < a_i$. The energy release rate decreases as the crack grows ($a > a_i$) and stabilizes over a set of crack lengths as the crack propagates. The average energy release rate in the steady state region (gray shaded region) is taken as the critical energy release rate G_c . This value is representative of the toughness of a sharp crack tip in a uniform material; the initial crack tip here is blunt, and there are other factors as

Humidity	Moisture Content (%)	Young's modulus $E(MPa)$	Toughness $G_{Ic}(J/m^2)$
16% RH	2.71	6.41 ± 1.75	16.34 ± 1.19
23% RH	3.17	5.57	12.90 ± 1.16
37% RH	4.05	4.28	9.27 ± 2.55
50% RH	5.11	3.12 ± 0.85	7.26 ± 0.65
75% RH	9.03	0.86 ± 0.34	2.32 ± 0.56

Table 4.1: Summary of out-of-plane toughness values of filter paper as a function of humidity. Two or three experiments were performed for each RH, and the results are given in the form $X \pm Y$, where X represents the mean value and Y represents the standard deviation.

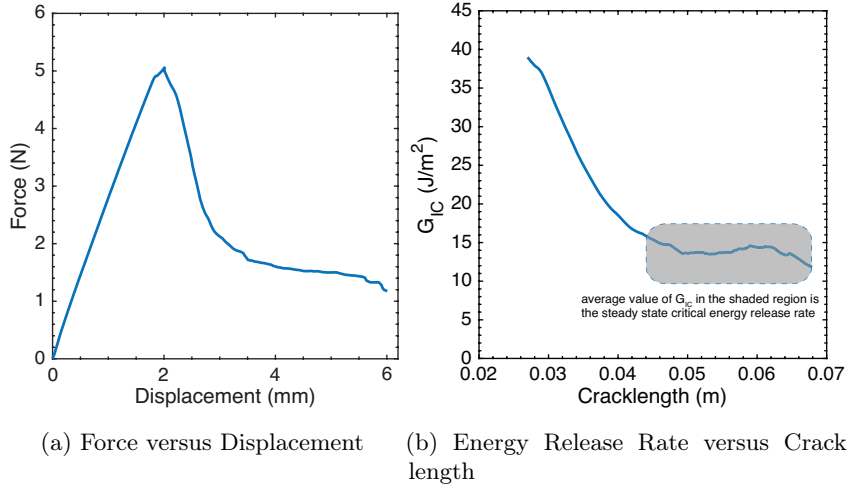


Figure 4.4: Representative Force-Displacement and subsequent Energy Release Rate plots at 23% RH from a DCB specimen

well such as artificial compression induced by the scissor cut at the edge, which is why the initial energy release rate is higher than the steady state value. This is a commonly observed phenomenon in the absence of sharp crack or some other artifact at the pre-crack in a DCB configuration, as reported by River and Okkonen [198] who categorized the quantities as crack initiation energy and crack arrest energy, and as explained by Long and Hui [199] who depicted why the assumption of translational invariance, or steady-state crack growth, does not hold in the crack initiation region using the example of hydrogels. In principle, especially for soft materials and for materials with no sharp crack, an extra term of stress and deformation fields due to crack initiation must be included in G .

Table 4.1 shows the variation of critical energy release rate as a function of moisture content. As moisture content increases, the toughness of the paper decreases, which is expected due to the weakening of the individual cellulose fibers and the bonds between them. This behavior of modulus with moisture content was also observed in similar earlier works [5, 200–203].

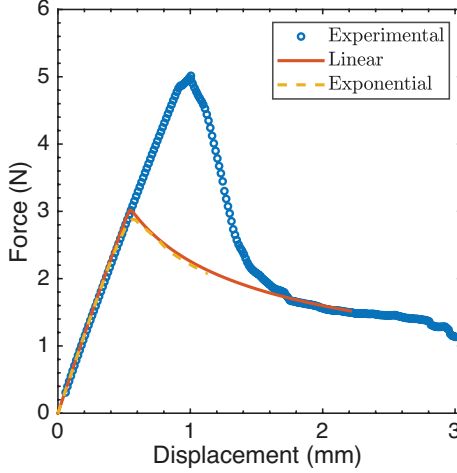


Figure 4.5: Comparisons between experimental data (blue hollow circles) and simulation results for traction-separation law with linear softening Eq. (4.8) (red solid curve) and traction-separation law with exponential softening Eq. (4.12) (yellow dashed curve) for 23% RH.

4.4.2 Finite Element Modeling Results

4.4.2.1 Exponential vs. Linear Softening

Simulations for 23% relative humidity were run with both linear softening Eq. (4.8) and exponential softening Eq. (4.12), to determine which traction-separation law fit best with the experimental results (Figure 4.5). As can be seen in Figure 4.5, the results from both simulations were almost identical. As such, the traction-separation law with linear softening Eq. (4.8) was chosen for the remainder of the simulations because it has fewer parameters and has a slight advantage in terms of the speed of simulations.

4.4.2.2 Parameters for Different Relative Humidities

The parameters for the simulations were selected in the following manner. t_n was chosen as the measured peak stress from the out-of-plane tensile tests. K_0 was chosen as

$$K_0 = \frac{E_f}{h_f}, \quad (4.15)$$

based on the out-of-plane modulus E_f of the filter paper from the out-of-plane tensile tests and the thickness of the filter paper h_f . δ_f was then chosen such that the resulting toughness value Eq. (4.13) from the traction-separation law Eq. (4.8) was within the uncertainty range of the toughness values

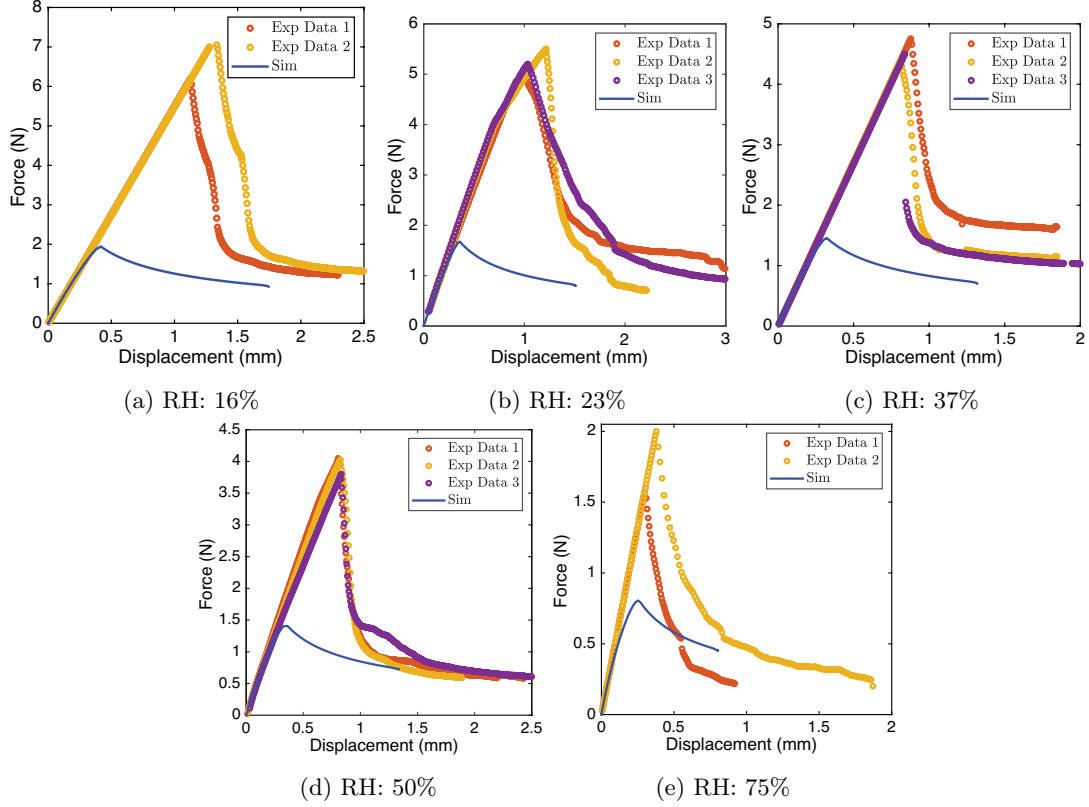


Figure 4.6: Force displacement plots from simulations (solid curves) as compared with experimental data (hollow circles) at different relative humidities (a) 16% RH, (b) 23% RH, (c) 37% RH, (d) 50% RH, and (e) 75% RH.

from the experimental data. Finally, NDP was calculated using Eq. (4.14).

The parameters for which the force displacement plots from simulations of different relative humidity (Figure 4.6) best fit with the corresponding force displacement plots from experiments are listed in Table 4.2, and the peak stresses t_n^0 and displacements δ_c and δ_f are plotted vs. humidity in Figure 4.7(a).

Figure 4.7(b) shows the traction-separation laws with linear softening (Eq. (4.8)) for the different relative humidities. The toughness, or critical energy release rate, value from the simulations is found by calculating the area under the traction-separation curve (Eq. (4.13)).

As can be seen in Figure 4.6, the initial loading portion of the simulations and the unloading stable crack growth regions fit well with the experimental data, but the simulations do not capture the large peak force and sudden drop which are present in the plots from the experimental data. The reason that these simulations cannot capture the peak force and sudden drop from the experimental results is, as mentioned earlier in Section 4.4.1, that the Whatman filter paper in the experiments

%RH	K_0 (10^{10} Pa/m)	t_n^0 (MPa)	δ_f (μm)	G_{Ic} (J/m^2)	NDP (unit-less)	F_{max} (N)
16	3.77	0.800	19.63	16.34	17.00	1.94
23	3.28	0.600	24.69	12.90	23.86	1.86
37	2.52	0.400	30.46	9.27	38.57	1.64
50	1.84	0.310	29.95	7.26	50.31	1.41
75	0.51	0.075	47.04	2.32	274.64	0.81

Table 4.2: Simulation parameter values by humidity for which force displacement plots from simulations at different relative humidities best fit with the corresponding force displacement plots from experiments.

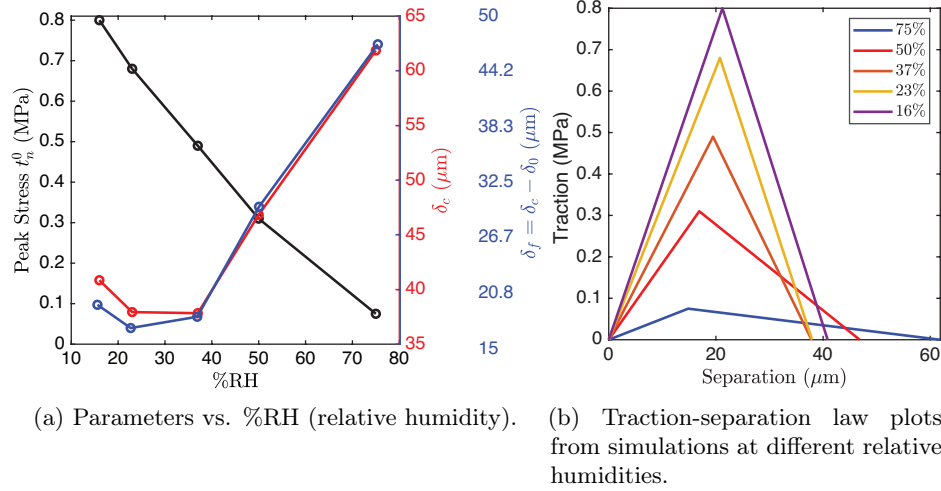


Figure 4.7: Cohesive parameters and cohesive law at different relative humidities: (a) Plots of the parameters peak stress t_n^0 , and displacements δ_f and δ_c vs. %RH (relative humidity), and (b) Traction-separation law plots from simulations at different relative humidities, using the traction-separation law with linear softening (Eq. (4.8)).

does not have a sharp crack, and the crack must be initiated before fracture mechanics applies [198, 199]. We also considered other possibilities, such as compressive stresses far ahead of the crack and non-uniform drying. Since there is compression ahead of the cohesive zone as can be seen in Figure 4.8, the cellulose network ahead of the crack could be damaged by the compression [1, 63, 199, 204] and could have a lower toughness than the initial region which is only subject to tension. Additionally, the specimens are cut to the required sizes using scissors which could potentially induce an artificial compression at the edge (pre-crack), which increases the resistance to the crack propagation at the pre-crack tip.

From Figure 4.8 it can be observed that the maximum compressive stress ahead of the crack is around 0.55 MPa for the 16% RH and 0.15 MPa for the 75% RH. From Table 4.1, the out-of-plane Young's modulus of the filter paper at 16% RH is 6.41 MPa and at 75% RH is 0.86 MPa. Hence,

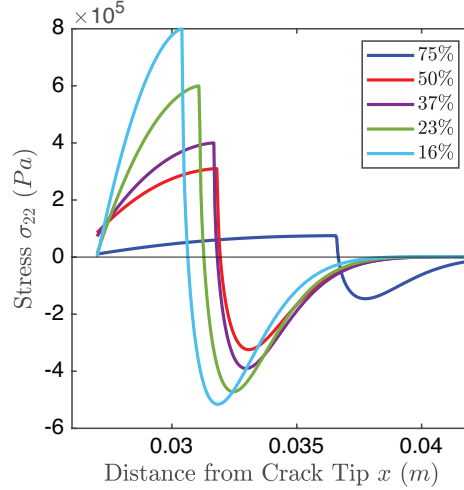


Figure 4.8: Stress profile along the direction of crack propagation, in the simulation frame just before the crack begins to open initially. Crack tip position initially, before the crack begins to open, is at 27 mm .

the compressive strain in the cellulose fibers ahead of the crack tip is around $0.55/6.41 = 0.086$ for 16% RH and $0.15/0.86 = 0.17$ for 75% RH. Buckling typically starts around compressive strain of 0.05 in foams and fiber networks [45], which is smaller than the compressive strains calculated above. However, the compressive stiffness is likely higher than the tensile stiffness, especially because compressing porous fibrous networks causes an increase in density which therefore could increase compressive stiffness [205, 206], and this could likely lower the calculated compressive strains. Moreover, the peak compressive stress/strain is millimeters ahead of the crack tip before the crack starts to propagate, whereas the sudden drop from peak force happens even before the crack starts to propagate. Additionally, the compressive strain limit of 0.05 in general foams and fiber networks [45] is valid for 3D isotropic materials. This is not necessarily the limit for cellulose networks, in particular filter paper, which are non-isotropic materials and most of the fibers are not aligned in the out-of-plane direction of loading. This implies that the presence of compressive stresses ahead of the crack tip may not be a significant factor contributing to the force anomaly.

To study the impact of artifacts at the pre-crack, such as having a blunt crack or scissors-induced compression, a new type of experiment was done at one humidity (31% RH) with multiple loading-unloading cycles. The phenomenon of initial high peak force and sudden drop can be clearly isolated (as shown in Figure 7(a) in [163]) from the region of stable crack growth using the equation resulting in a flat R-curve (as shown in Figure 7(b) in [163]) using (4.2) and (4.3). This experiment shows

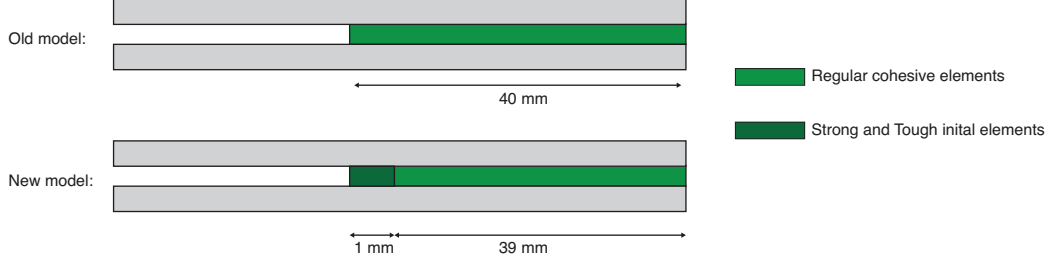


Figure 4.9: Cartoon depicting the changes made to the model in order to incorporate the tougher initiation region cohesive elements, as well as the regular cohesive elements. (Note: This image is not to scale.)

%RH	Element Type	K_0 (10^{10} Pa/m)	t_n^0 (MPa)	δ_f (μm)	G_{Ic} (J/m^2)	NDP (unit-less)	F_{max} (N)
16	Initiation Cohesive Elements	781.77	8.000	21.36	89.50	0.93	6.41
	Steady State Cohesive Elements	3.77	0.800	19.63	16.34	17.00	
23	Initiation Cohesive Elements	692.94	6.000	19.14	59.98	1.11	5.04
	Steady State Cohesive Elements	3.28	0.600	24.69	12.90	23.86	
37	Initiation Cohesive Elements	517.65	4.000	20.22	41.98	1.75	3.70
	Steady State Cohesive Elements	2.52	0.400	30.46	9.27	38.57	
50	Initiation Cohesive Elements	255.29	3.100	20.84	34.18	2.39	3.05
	Steady State Cohesive Elements	1.84	0.310	29.95	7.26	50.31	
75	Initiation Cohesive Elements	55.41	0.750	16.59	6.73	7.96	1.03
	Steady State Cohesive Elements	0.51	0.075	47.04	2.32	274.64	

Table 4.3: Simulation parameter values by humidity for which force displacement plots from simulations including the initiation element region at different relative humidities best fit with the corresponding force displacement plots from experiments.

that among the reasons causing the initial high peak force, artifacts at the pre-crack, such as having a blunt crack or scissors-induced compression are the primary reason for the force anomaly and further corroborates that compression ahead of the crack-tip is not a significant factor.

Inspired by a previous report [199], to account for the change in behavior from crack initiation to crack propagation, cohesive elements representing the Whatman paper are divided into two regions: a crack initiation region with parameters that give higher toughness, and the steady state crack growth region comprising the rest of the Whatman filter paper with parameters estimated before (see Figure 4.9). We choose a length for this crack initiation region to be 1 mm since this is about 10 times larger than the root radius of the initial crack. We choose the cohesive parameters for this initiation region by using the following process: First, as the toughness value we take the maximum energy release rate in the experimental data (as calculated by Eq. (4.3)). We choose the peak stress t_n^0 to be exactly one order of magnitude larger than in the steady state region, and we choose the stiffness K_0 to be about two orders of magnitude larger than in the steady state region. We calculate the displacement to failure δ_f parameter from the toughness relation Eq. (4.13), and NDP from Eq. (4.14).

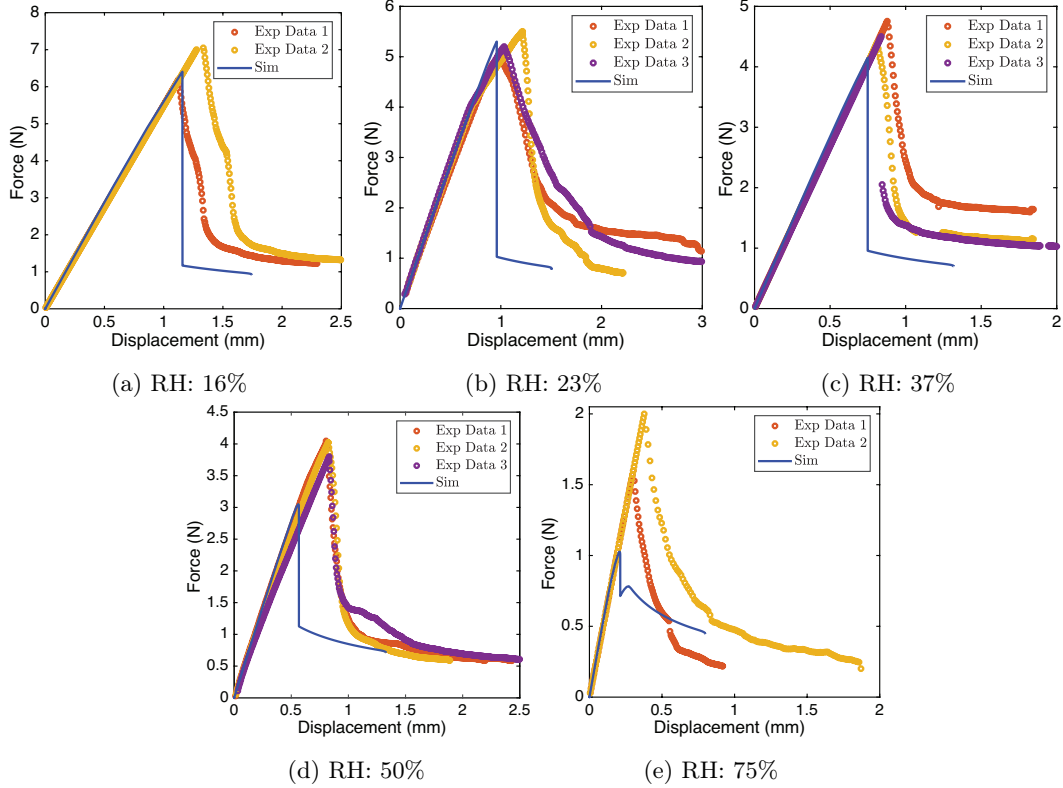


Figure 4.10: Force displacement plots from simulations including the tougher cohesive element crack initiation regions (solid curves) as compared with experimental data (colored circles) at different relative humidities (a) 16% RH, (b) 23% RH, (c) 37% RH, (d) 50% RH, and (e) 75% RH.

As can be seen in Figure 4.10, the simulations including the initiation region to represent the apparent toughness due to the artifacts at the pre-crack, such as having a blunt crack or scissors-induced compression, capture not only the initial loading portion and the steady state crack growth region of the unloading portion of the force-displacement curves, but also the peak force and the sudden drop. The transition between the initiation region and steady state crack growth region is known to be complex [199], so we do not model it here. The parameters of the simulations using the initiation region model for which the force displacement plots from simulations of different relative humidities (Figure 4.10) best fit with the corresponding force displacement plots from experiments are listed in Table 4.3. There is some variability in the experimental data, and small variations in the thickness and modulus of the PMMA have a large effect on the energy release rate (see Eq. (4.3)) so the fits are not exact, but the key qualitative features of the force-displacement curve can be explained by the presence of an initiation region to represent the apparent toughness due to the pre-crack artifacts in our finite element calculations (see Figure 4.11 for verification that both the

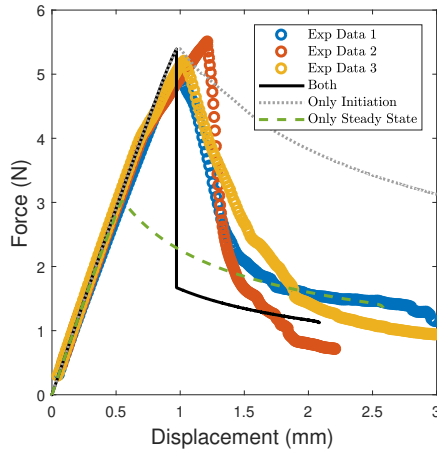


Figure 4.11: Experimental results compared to simulation results using the model developed in the manuscript (solid curve), a simulation in which all the cohesive elements had the same parameters as in the initiation region (dotted curve), and the simulation from the manuscript using only the parameters from the steady state region (dashed curve).

initiation region and steady state region are necessary to capture the experimental results).

The results shown here with the high peak force and sudden drop to a plateau region of steady state crack growth, both in experiments and simulations, resemble results from earlier works such as [198]. Depicted there is a plot for three different materials exhibiting the same behavior with an initial high peak force and then a sudden drop to a lower plateau (see Figure 11 in [198]). However, these plots exhibit a saw-tooth pattern due to a boundary condition of holding opening displacement of the DCB fixed in cycles. This is not seen in our experimental results since we continuously increase the opening displacement of our DCB, not doing so in a step-wise fashion. In our simulations the opening displacement is increased in a step-wise fashion but those steps are small so that it mimics a continuous increase. Nonetheless, it is clear that there is a direct analogy between the crack initiation energy in [198] and our initiation region toughness value G_{Ii} , and between the crack arrest energy in [198] and our steady state crack growth region toughness value G_{Ic} .

Generally, it is preferable to design experiments in such a way that either a sharp crack is produced before any measurements are taken or precautions are taken to make sure the material is uniform throughout the length, to avoid high peaks and sudden drops in the force-displacement data. However, in some systems it is difficult to introduce a sharp crack initially, such as in [198] or when studying the fracture toughness of the out-of-plane direction of two-dimensional sheets as we do here. Our simulation approach which includes an initial crack initiation region with

tougher/stronger cohesive elements to represent the apparent toughness due to artifacts, followed by steady-state crack growth region cohesive elements accounts for this difficulty in the experiment and allows for extraction of useful data even in such situations in which experimentally obtaining a sharp crack is difficult or even impossible.

4.4.2.3 Parametric study

In studying the effect on the force-displacement plot of each of the five different parameters in the bi-linear traction-separation law, it is important to keep in mind that only three of them can be independent for any given simulation. For example, the parameter G_{Ic} defined above (Eq. (4.13)) for the bi-linear traction-separation law Eq. (4.8) can be rewritten as

$$G_{Ic} = \frac{t_n^0}{2} \left(\frac{t_n^0}{K_n} + \delta_f \right), \quad (4.16)$$

and therefore the parameter NDP defined above (Eq. (4.14)) can also be rewritten

$$NDP = \frac{E_{PMMMA}}{2h} \left(\frac{1}{K_n} + \frac{\delta_f}{t_n^0} \right), \quad (4.17)$$

both now entirely in terms of cohesive properties t_n^0 , K_n , and δ_f . Alternatively, the above equations Eq. (4.16) and Eq. (4.17) can be rearranged into

$$t_n^0 = \sqrt{\frac{E_{PMMMA} G_{Ic}}{h NDP}} \quad (4.18)$$

$$\delta_f = \sqrt{\frac{E_{PMMMA} G_{Ic}}{h NDP}} \left(\frac{2h NDP}{E_{PMMMA}} - \frac{1}{K_n} \right), \quad (4.19)$$

such that the cohesive parameters δ_f and t_n are entirely in terms of cohesive parameters K_n , G_{Ic} , and NDP . The latter three are the ones we use in our parameter study below.

As can be seen in Figure 4.12(a), a 10% change in the K_0 value, both higher and lower, has no visible effect on the force-displacement plots. The 10% lower $K_0 = 5.91 * 10^{12} Pa/m$ yields a slightly lower peak force of 5.37 N and pulls the sudden drop to a slightly lower displacement of 0.968 mm, and vice versa for the 10% higher K_0 . Similarly, as can be seen in Figure 4.12(b), a 10% change in the NDP parameter has little visible effect; a 10% lower $NDP = 0.90$ yields a slightly higher peak force of 5.41 N and pushes the sudden drop to a slightly higher displacement of 0.98 mm, and a 10% higher $NDP = 1.10$ yields a slightly lower peak force of 5.34 N and pulls the sudden drop to a

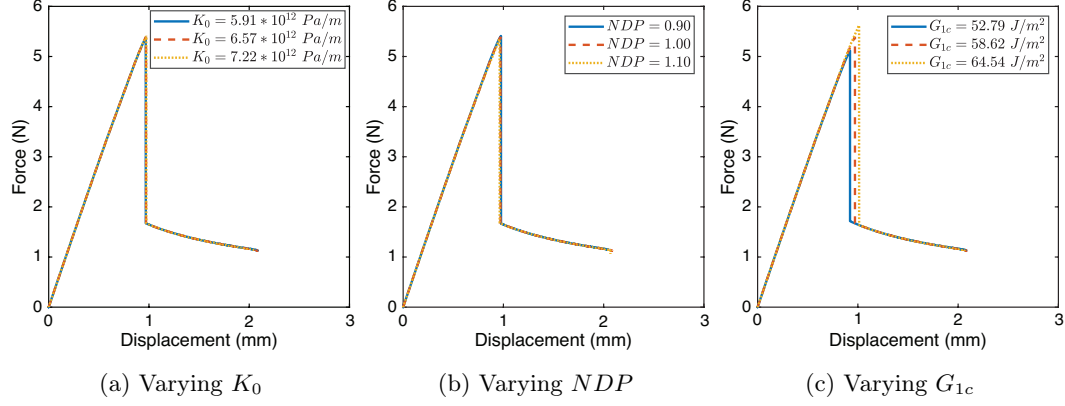


Figure 4.12: Study of the effects of how 10% changes in tough initiation region cohesive parameters affect the force-displacement results plots. The three independent cohesive parameters studied were (a) K_0 , (b) NDP , and (c) G_{1c} . In all of these simulations, the regular cohesive parameters were $K_0 = 2.56524 \times 10^{12} \text{ Pa/m}$, $\sigma_0 = 8.89728 \times 10^6 \text{ Pa}$, $\delta_f = 7.76926 \times 10^{-6} \text{ m}$, $G_{1c} = 18.064 \text{ J/m}^2$, and $NDP = 1.00$. (a) Varying K_0 : tough initiation region cohesive parameter NDP was held fixed at 1.00 and G_{1c} was held fixed at 58.62 J/m^2 , while tough initiation region cohesive parameters $K_0 = 5.91 \times 10^{12} \text{ Pa/m}$, $t_n = 7.02 \times 10^6 \text{ Pa}$, and $\delta_f = 15.54 \times 10^{-6} \text{ m}$ (blue solid curve), $K_0 = 6.57 \times 10^{12} \text{ Pa/m}$, $t_n = 7.02 \times 10^6 \text{ Pa}$, and $\delta_f = 15.66 \times 10^{-6} \text{ m}$ (red dashed curve), and $K_0 = 7.22 \times 10^{12} \text{ Pa/m}$, $t_n = 7.02 \times 10^6 \text{ Pa}$, and $\delta_f = 15.75 \times 10^{-6} \text{ m}$ (yellow dotted curve). (b) Varying NDP : tough initiation region cohesive parameter K_0 was held fixed at $6.56524 \times 10^{12} \text{ Pa/m}$ and G_{1c} was held fixed at 58.6179 J/m^2 , while tough initiation region cohesive parameters $NDP = 0.90$, $t_n = 7.40 \times 10^6 \text{ Pa}$, and $\delta_f = 14.74 \times 10^{-6} \text{ m}$ (blue solid curve), $NDP = 1.00$, $t_n = 7.02 \times 10^6 \text{ Pa}$, and $\delta_f = 15.66 \times 10^{-6} \text{ m}$ (red dashed curve), and $NDP = 1.10$, $t_n = 6.69 \times 10^6 \text{ Pa}$, and $\delta_f = 16.52 \times 10^{-6} \text{ m}$ (yellow dotted curve). (c) Varying G_{1c} : tough initiation region cohesive parameter K_0 was held fixed at $6.56524 \times 10^{12} \text{ Pa/m}$ and NDP was held fixed at 1.00, while tough initiation region cohesive parameters $G_{1c} = 52.79 \text{ J/m}^2$, $t_n = 6.66 \times 10^6 \text{ Pa}$, and $\delta_f = 14.85 \times 10^{-6} \text{ m}$ (blue solid curve), $G_{1c} = 58.62 \text{ J/m}^2$, $t_n = 7.02 \times 10^6 \text{ Pa}$, and $\delta_f = 15.66 \times 10^{-6} \text{ m}$ (red dashed curve), and $G_{1c} = 64.54 \text{ J/m}^2$, $t_n = 7.36 \times 10^6 \text{ Pa}$, and $\delta_f = 16.20 \times 10^{-6} \text{ m}$ (yellow dotted curve).

slightly lower displacement of 0.96 mm , both as compared to the $NDP = 1.00$ with a peak force of 5.39 N and sudden drop at a displacement of 0.97 mm . (Larger changes in NDP may have more significant effects.) However, as can be seen in Figure 4.12(c), a 10% change in the G_{Ii} parameter has a much more significant effect on the force-displacement plots; a 10% lower $G_{Ii} = 52.79 \text{ J/m}^2$ yields a lower peak force of 5.11 N and pulls the sudden drop to a lower displacement of 0.92 mm , and a 10% higher $G_{Ii} = 64.54 \text{ J/m}^2$ yields a higher peak force of 5.62 N and pushes the sudden drop to a higher displacement of 1.01 mm , both as compared to the $G_{Ii} = 58.62 \text{ J/m}^2$ with a peak force of 5.39 N and sudden drop at displacement 0.97 mm .

It should also be noted that, as expected, for each of the simulations, the toughness value is

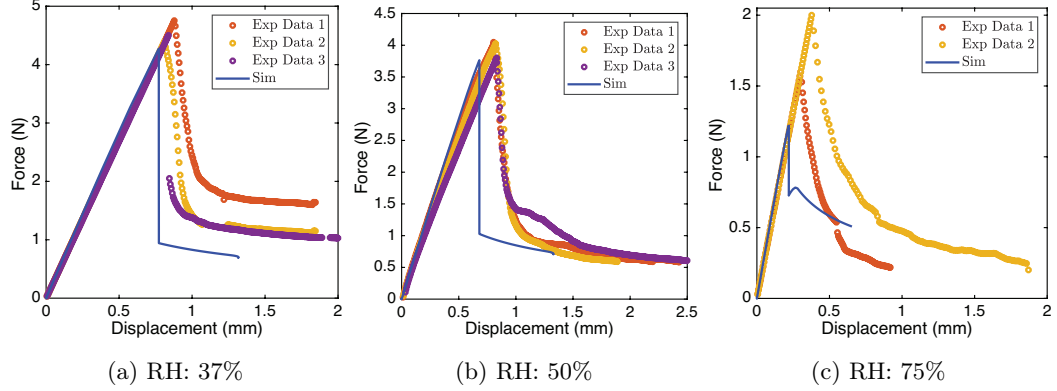


Figure 4.13: Results for fixing the NDP in the initiation region instead of the peak stress there.

(approximately) directly proportional to the square of the peak force value:

$$G_{Ii} \approx 2F_{\max}^2. \quad (4.20)$$

4.4.2.4 Comparison of experiments and simulations

As can be seen in Figure 4.10, the force-displacement plots obtained from the finite element calculations with linear softening and tougher initiation region fit the experimental data quite well. For example, for 16% relative humidity in Figure 4.10(a), the loading slopes from the experimental data and the simulation results are almost identical, the peak forces are very close, and the unloading curves are similar in shape and magnitude, including the sudden drop from the peak force and its location in the plot. The same is true for 23% relative humidity. The peak forces are less close in (Figure 4.10(b)), 37% relative humidity (Figure 4.10(c)), 50% relative humidity (Figure 4.10(d)), and 75% relative humidity (Figure 4.10(e)), but all other characteristics of the experiment are captured. It should be noted that small variations in the thickness and modulus of the PMMA have a large effect on the energy release rate (see Eq. (4.3)) so the fits are not exact. Additionally, if the NDP in the initiation region is held fixed at 1 instead of specifying the peak stress there, the fits would improve (see Figure 4.13).

It should also be noted that the displacement value used here for comparison in both the experimental data and the simulation results is $\delta = \Delta/2$, or half of the distance between the two ends of the original crack tip, and not Δ , the full distance between the two ends of the original crack tip.

A comparison of the toughness values measured from experiments to those calculated from the simulation results for different relative humidities can be found in Table 4.4. The toughness values

RH:	16%	23%	37%	50%	75%
Simulation $G_{I_c}(J/m^2)$:	16.33	12.90	9.27	7.26	2.32
Experiment $G_{I_c}(J/m^2)$:	16.34 ± 1.19	12.90 ± 1.16	9.27 ± 2.55	7.26 ± 0.65	2.32 ± 0.56

Table 4.4: Toughness values calculated from simulations at different relative humidities and the corresponding values as measured from experiments. The experimental results are given in the form $X \pm Y$, where X represents the mean value and Y represents the standard deviation. The toughness values calculated from the simulation results for all five relative humidities are within the measurement errors of the toughness values measured from the experimental data.

calculated from the simulation results for all five relative humidities are within the measurement errors of the toughness values measured from the experimental data.

The reader can also simultaneously look at Supplementary Material Video 1 of [163], to visualize the crack propagation during fracture in the experiment and simulation.

4.5 Conclusion

In the current study, the effect of moisture content on out-of-plane toughness of cellulose filter paper was studied using double cantilever beam fracture tests. Cohesive zone modeling was used to describe crack propagation in the filter paper. The parameters of the traction-separation laws were fitted to experimental data. Experimental measurements revealed a decreasing trend in the modulus and fracture toughness with an increase in moisture content, as a consequence of moisture induced weakening of cellulose network. Due to pre-crack artifacts, there is a higher peak force and sudden decrease as the crack grows, which was captured by the newly developed finite element model involving two kinds of cohesive elements: tough elements near the initial crack tip to represent the apparent toughness due to artifacts at the pre-crack, such as having a blunt crack or scissors-induced compression, succeeded by steady state crack growth elements. The effect of each independent cohesive parameter was also investigated, and the overall force-displacement curves of the DCB specimens was captured quite well.

Chapter 5

Conclusions

In this dissertation, we focus on specific fibrous network materials such as fibrin fiber networks in blood clots, pulmonary emboli, and Whatman filter paper cellulose networks, and on specific behavior such as development of pre-stress, compression, and fracture. These materials specifically are comprised of randomly oriented, relatively stiff, straight fibers, and the mechanical properties studied here comprise three stages of life that materials frequently will experience: first, fiber strands grow and connect to become a network, and the material forms; then, natural forces act upon the material, resulting in physical and structural changes in the material; and finally, the material undergoes failure processes, and the material breaks down. These stages are represented here in the following fashion: First, the growth of a fibrous network material, specifically a fibrin network, is studied analytically from the level of individual fibers and their molecular polymerization, from which material properties are extracted using an 8-chain model [41, 49–51]. Then, since such a material in nature experiences forces which act upon it and change its structural and physical properties, the loading and unloading cycles of compression and decompression experienced by fibrin network blood clots and thromboemboli in veins are simulated here by cyclical compression and decompression of *ex vivo* pulmonary emboli between parallel rheometer plates. Finally, a common failure process is fracture under tensile forces, which is modeled here using continuum cohesive zone traction-separation laws and small scale finite element analysis of Whatman filter paper cellulose fibrous networks. These are three basic stages of the life-cycle of fibrous network materials, properties studied here of fibrous network materials which emerge from these life-cycles, and the specific fibrous network materials studied.

We modeled blood clot formation – from fibrinogen to fibrin monomers and oligomers, to protofibrils to fiber formation – as a set of ODEs for chemical rate of change in concentration of the reacting structures of each individual stage. The solutions to that system of ODEs give the average number of protofibrils per fiber cross-section as a function of fibrin polymerization time. By variation of

the rate constants involved in the intermediary biochemical reactions, we demonstrated that the two most important stages determining final fiber thickness are the reactions for fiber initiation by lateral aggregation of protofibrils, and fiber growth by association with additional protofibrils. The resulting average number of protofibrils per fiber cross-section is directly related to the radius of a fiber, yielding the radius of a fiber as a function of polymerization time. This fiber radius is used as an input in calculating the evolving tensile force on a helical fiber. We derive the tensile force in a helical fiber by a force balance on the fiber cross-section in which some protofibrils are stretched and others are shortened. The tensile force in a network fiber depends on the fiber radius and the stretch of the fiber with respect to a (hypothetical) free fiber in equilibrium. We also model relaxation of a fiber transversely cut from a network, yielding the relaxation time, which seems to depend on the stretch of the fiber as well as the fiber length and radius. The resulting timescales and fiber strains are in excellent agreement with previous reports of cutting of fibrin fibers from a network [60]. Finally, we derive network properties such as stress due to polymerization and/or external forces from fiber properties using an 8-chain model [41, 49]. We show that the inherent tensile stress in polymerizing fibrin networks depends on fiber length, radius, solid volume fractions, etc. The computed inherent network stress is in agreement with experimental results. Estimations of inherent stress in a fibrin fiber network, as well as of other network material properties, will be useful in interpreting experiments performed on blood clots and thrombi, in the use of fibrin as a biomaterial, and in the application and development of novel methods of treatment of thrombotic states such as in mechanical thrombectomy and thrombolysis.

We then characterized the mechanical response of pulmonary emboli to cyclic compression while simultaneously tracking changes in their structure. We observed directly for the first time that pulmonary emboli behave like foams (open soft network of fibers with large pores) in response to compression and passive decompression. Additionally, stress-strain curves for all pulmonary emboli revealed four portions characteristic of a hysteresis loop. The compression part of curve has the following regions: 1) linear regime in which normal stress increases proportionally with increasing compressive strain, and 2) non-linear response as result of rapid upturn in normal stress. The passive decompression part of curve has the following regions: 3) non-linearly elastic region or re-stretching of the network, in which normal stress dropped rapidly; 4) at lower strains, the normal stress was rather insensitive to decompression, reflecting a linear response to strain and resulting in a closed cycle. Thus, compression and decompression do not follow the same pathway, meaning

that the stress- strain behavior of pulmonary emboli exhibits a hysteresis loop upon cyclic loading, indicating the dissipation of energy. We described this behavior using a continuum theory of phase transitions, which acknowledges that within a range of compressive stresses the fibrin network of the embolus can have co-existing rarefied and densified phases. The fibers are mostly straight in the rarefied phase, while they are significantly bent with a number of contacts in the densified phase. The fractions of each phase change as the embolus is compressed or decompressed. The fibrin fibers and RBCs are damaged during the compression process, causing irreversible changes in the structure of the emboli. We also showed that the stress response of emboli depends on their structure, namely, that variations in the composition of emboli can lead to quantitatively different normal stress-strain responses. Emboli with a high fibrin component demonstrate higher normal stress compared to emboli that have a high RBC component. Understanding these nuances in mechanical properties of emboli will garner a deeper understanding of thromboembolisms and therapeutic disintegration and removal of intravascular thrombi using mechanical means such as ultrasound, aspiration, and mechanical thrombectomy.

Next, we studied the effect of moisture content on out-of-plane toughness of cellulose filter paper using double cantilever beam fracture tests. Cohesive zone modeling was used to describe crack propagation in the filter paper. We fitted the parameters of the traction-separation laws to experimental data. Experimental measurements revealed a decreasing trend in the modulus and fracture toughness with an increase in moisture content, as a consequence of moisture induced weakening of the cellulose network. Due to pre-crack artifacts, there is a higher peak force and sudden decrease as the crack grows, which we captured by the newly developed finite element model involving two kinds of cohesive elements: tough elements near the initial crack tip to represent the apparent toughness due to artifacts at the pre-crack, such as having a blunt crack or scissors-induced compression, succeeded by steady state crack growth elements. We investigated the effect of each independent cohesive parameter and captured the overall force-displacement curves of the DCB specimens quite well.

The work on the mechanics of fibrous networks discussed here differs from previous studies in that we did not perform large scale finite element calculations, rather we focused on continuum mechanical models to study mechanical behaviors of these networks. Unlike large finite element calculations, these continuum mechanical models are built to capture specific mechanical behaviors, and their origins are in disparate fields which have little to do with networks. Additionally, the

models derived for each of the specific materials can be applied to the other materials discussed, as well as to other fibrous network materials, with some parameter changes and possibly other minor variations. For example, the cohesive zone model presented for cellulose networks can be applied to fibrin networks in blood clots. We think this is feasible because [207] have revealed with simulations for cracked specimens stress-strain curves of the same shape as in the traction-separation laws in cohesive zone models for cellulose networks. This and other aspects of the work in this dissertation can also be expanded upon and applied to additional problems in the future, such as how inherent tension in fibrin fiber networks affects the fracture toughness of the network material; how the properties of individual fibers in, and helical structure of, other types of fibrous network materials, such as carbon nanotubes in hierarchically arranged helical fiber ropes [208, 209], would affect the properties of those materials; how fluid flow would affect the rate-dependent mechanical behavior of the network; how additional substances in fibrous networks would affect the material properties of the network, similar to how red blood cells affect the material properties of emboli; and modulating the fracture properties of cellulose network materials with a physical parameter other than the humidity dependence studied here.

The works presented here have direct relevance to biological, clinical, and industrial applications including in the use of fibrin as a biomaterial – for example, the inherent tension may comprise a thermodynamic mechanism to control fiber diameter, and thus modulate the overall network structure – and in the application and development of novel methods of treatment of thrombotic states such as in mechanical thrombectomy since the susceptibility of fibrin to fibrinolytic enzymes depends strongly on the mechanical tension of the proteinaceous fibrous substrate [58–61]; garnering a deeper understanding of thromboembolisms, therapeutic disintegration and removal of intravascular thrombi using mechanical means such as ultrasound, aspiration, and mechanical thrombectomy; and in the fabrication of piezoelectric cellulose sheets and batteries [174–177, 210], and in studying scoring, folding and 3-D forming operations. Thus, as well as in mechanics and materials disciplines, this work is important in furthering scientific knowledge from biological, clinical, and industrial settings.

BIBLIOGRAPHY

- [1] I. N. Chernysh, R. Spiewak, C. L. Cambor, P. K. Purohit, and J. W. Weisel. “Structure, mechanical properties, and modeling of cyclically compressed pulmonary emboli”, *Journal of the Mechanical Behavior of Biomedical Materials*, **105**: 103699, (2020). DOI:10.1016/j.jmbbm.2020.103699.
- [2] M. T. J. J. M. Punter, B. E. Vos, B. M. Mulder, and G. H. Koenderink. “Poroelectricity of (bio)polymer networks during compression: theory and experiment”, *Soft Matter*, **16**: 1298–1305, (2020). DOI:10.1039/C9SM01973A.
- [3] D. A. Fletcher and R. D. Mullins. “Cell mechanics and the cytoskeleton”, *Nature*, **463**: 485–492, (2010). DOI:10.1038/nature08908.
- [4] K. A. Jansen, A. J. Licup, A. Sharma, R. Rens, F. C. MacKintosh, and G. H. Koenderink. “The role of network architecture in collagen mechanics”, *Biophysical Journal*, **114**(11): 2665–2678, (2018). DOI:10.1016/j.bpj.2018.04.043.
- [5] A. H. Nissan. “H-Bond Dissociation in Hydrogen Bond Dominated Solids”, *Macromolecules*, **9**(5): 840–850, (Sept. 1976). DOI:10.1021/ma60053a026.
- [6] S. Toll. “Packing mechanics of fiber reinforcements”, *Polymer Engineering and Science*, **38**(8): 1337–1350, (1998). DOI:10.1002/pen.10304.
- [7] F. Lundell, L. D. Söderberg, and P. H. Alfredsson. “Fluid mechanics of papermaking”, *Annual Review of Fluid Mechanics*, **43**(1): 195–217, (2011). DOI:10.1146/annurev-fluid-122109-160700.
- [8] A. Céline, S. Fréour, F. Jacquemin, and P. Casari. “The hygroscopic behavior of plant fibers: a review”, *Frontiers in Chemistry*, **1**(43): 1–12, (Jan. 2014). DOI:10.3389/fchem.2013.00043.
- [9] E. K. Gamstedt. “Moisture induced softening and swelling of natural cellulose fibres in composite applications”, in *37th Riso International Symposium on Materials Science*, vol. 139: 012003, IOP Conference Series: Materials Science and Engineering, (2016). DOI:10.1088/1757-899X/139/1/012003.

- [10] A. Saha, C. Jiang, and A. A. Martí. “Carbon nanotube networks on different platforms”, *Carbon*, **79**: 1–18, (2014). DOI:10.1016/j.carbon.2014.07.060.
- [11] C. M. van Wyck. “Note on the compressibility of wool”, *Journal of the Textile Institute Transactions*, **37**(12): T285–T292, (1946).
- [12] X. Liu and X. Wang. “A comparative study on the felting propensity of animal fibers”, *Textile Research Journal*, **77**(12): 957–963, (2007). DOI:10.1177/0040517507083517.
- [13] P. J. Flory and J. Rehner. “Statistical mechanics of cross-linked polymer networks i. rubberlike elasticity”, *The Journal of Chemical Physics*, **11**(11): 512–520, (1943). DOI:10.1063/1.1723791.
- [14] P. J. Flory and J. Rehner. “Statistical mechanics of cross-linked polymer networks ii. swelling”, *The Journal of Chemical Physics*, **11**(11): 521–526, (1943). DOI:10.1063/1.1723792.
- [15] H. Alamri and I. Low. “Mechanical properties and water absorption behaviour of recycled cellulose fibre reinforced epoxy composites”, *Polymer Testing*, **31**(5): 620–628, (Aug. 2012). DOI:10.1016/j.polymertesting.2012.04.002.
- [16] F. Xu, Y. Cui, D. Bao, D. Lin, S. Yuan, X. Wang, H. Wang, and Y. Sun. “A 3d interconnected cu network supported by carbon felt skeleton for highly thermally conductive epoxy composites”, *Chemical Engineering Journal*, **388**: 124287, (2020). DOI:https://doi.org/10.1016/j.cej.2020.124287.
- [17] J.-Y. Sun, X. Zhao, W. R. K. Illeperuma, O. Chaudhuri, K. H. Oh, D. J. Mooney, J. J. Vlassak, and Z. Suo. “Highly stretchable and tough hydrogels”, *Nature*, **489**: 133–136, (2012). DOI:10.1038/nature11409.
- [18] T. Gan, Y. Zhang, and Y. Guan. “In situ gelation of p(nipam-hema) microgel dispersion and its applications as injectable 3d cell scaffold”, *Biomacromolecules*, **10**(6): 1410–1415, (2009). DOI:10.1021/bm900022m.
- [19] T. Itahara, T. Tsuchida, and M. Morimoto. “Solvent-driven swelling and shrinking of poly(nipam) gels crosslinked by tris-methacrylated phloroglucinol derivatives”, *Polymer Chemistry*, **1**: 1062–1066, (2010). DOI:10.1039/C0PY00068J.

- [20] B. S. Hwang, J. S. Kim, J. M. Kim, and T. S. Shim. “Thermogelling behaviors of aqueous poly(n-isopropylacrylamide-co-2-hydroxyethyl methacrylate) microgel–silica nanoparticle composite dispersions”, *Materials*, **14**(5): 1212, (2021). DOI:10.3390/ma14051212.
- [21] S. Deogekar and R. C. Picu. “On the strength of random fiber networks”, *Journal of the Mechanics and Physics of Solids*, **116**: 1–16, (2018). DOI:10.1016/j.jmps.2018.03.026.
- [22] A. S. Shahsavari and R. C. Picu. “Size effect on mechanical behavior of random fiber networks”, *International Journal of Solids and Structures*, **50**(20-21): 3332–3338, (2013). DOI:10.1016/j.ijsolstr.2013.06.004.
- [23] R. C. Picu and A. Sengab. “Structural evolution and stability of non-crosslinked fiber networks with inter-fiber adhesion”, *Soft Matter*, **14**(12): 2254–2266, (2018). DOI:10.1039/c7sm02555f.
- [24] L. Zhang, S. P. Lake, V. H. Barocas, M. S. Shephard, and R. C. Picu. “Cross-linked fiber network embedded in an elastic matrix”, *Soft Matter*, **9**(28): 6398–6405, (2013). DOI:10.1039/C3SM50838B.
- [25] S. Deogekar, M. Islam, and R. Picu. “Parameters controlling the strength of stochastic fibrous materials”, *International Journal of Solids and Structures*, **168**: 194–202, (2019). DOI:10.1016/j.ijsolstr.2019.03.033.
- [26] S. Deogekar, Z. Yan, and R. C. Picu. “Random Fiber Networks With Superior Properties Through Network Topology Control”, *Journal of Applied Mechanics*, **86**(8): 081010, (06 2019). DOI:10.1115/1.4043828.
- [27] M. R. Islam and R. C. Picu. “Random fiber networks with inclusions: The mechanism of reinforcement”, *Physical Review E*, **99**(6): 063001, (2019). DOI:10.1103/PhysRevE.99.063001.
- [28] S. Deogekar and R. C. Picu. “Strength of stochastic fibrous materials under multiaxial loading”, *Soft Matter*, **17**: 704–714, (2021). DOI:10.1039/D0SM01713B.
- [29] P. R. Onck, T. Koeman, T. Van Dillen, and E. Van Der Giessen. “Alternative explanation of stiffening in cross-linked semiflexible networks”, *Physical Review Letters*, **95**(17): 178102, (2005). DOI:10.1103/PhysRevLett.95.178102.
- [30] G. Žagar, P. R. Onck, and E. V. der Giessen. “Elasticity of rigidly cross-linked networks of athermal filaments”, *Macromolecules*, **44**: 7026–7033, (2011). DOI:10.1021/ma201257v.

- [31] G. Žagar, P. R. Onck, and E. V. der Giessen. “Two fundamental mechanisms govern the stiffening of cross-linked networks”, *Biophysical Journal*, **108**: 1470–1479, (2015). DOI:10.1016/j.bpj.2015.02.015.
- [32] C. P. Broedersz, M. Sheinman, and F. C. MacKintosh. “Filament-length-controlled elasticity in 3d fiber networks”, *Physical Review Letters*, **108**: 078102, (2012). DOI:10.1103/PhysRevLett.108.078102.
- [33] J. L. Shivers, S. Arzash, and F. C. MacKintosh. “Nonlinear poisson effect governed by a mechanical critical transition”, *Physical Review Letters*, **124**: 038002, (2020). DOI:10.1103/PhysRevLett.124.038002.
- [34] A. S. Abhilash, B. M. Baker, B. Trappmann, C. S. Chen, and V. B. Shenoy. “Remodeling of fibrous extracellular matrices by contractile cells: Predictions from discrete fiber network simulations”, *Biophysical Journal*, **107**: 1829–1840, (2014). DOI:http://dx.doi.org/10.1016/j.bpj.2014.08.029.
- [35] E. Ban, J. M. Franklin, S. Nam, L. R. Smith, H. Wang, R. G. Wells, O. Chaudhuri, J. T. Liphardt, and V. B. Shenoy. “Mechanisms of plastic deformation in collagen networks induced by cellular forces”, *Biophysical Journal*, **114**: 450–461, (2018). DOI:https://doi.org/10.1016/j.bpj.2017.11.3739.
- [36] E. Ban, H. Wang, J. M. Franklin, J. T. Liphardt, P. A. Janmey, and V. B. Shenoy. “Strong tri-axial coupling and anomalous poisson effect in collagen networks”, *Proceedings of the National Academy of Sciences*, **116**(14): 6790–6799, (2019). DOI:10.1073/pnas.1815659116.
- [37] R. I. Litvinov and J. W. Weisel. “Fibrin mechanical properties and their structural origins”, *Matrix Biology*, **60-61**: 110–123, (2017). DOI:10.1016/j.matbio.2016.08.003.
- [38] G. S. Vankayalapati and K. T. Turner. “Hierarchical architected cellulose sheets with improved toughness using elastic heterogeneity”, *Cellulose, (In Preparation)*.
- [39] R. S. Rivlin and D. W. Saunders. “The free energy of deformation for vulcanized rubber”, *Transactions of the Faraday Society*, **48**: 200–206, (1952). DOI:10.1039/TF9524800200.
- [40] R. OGDEN. “Elastic deformations of rubberlike solids”, in *Mechanics of Solids*

- (H. HOPKINS and M. SEWELL, eds.): 499–537. Oxford: Pergamon, (1982). DOI:<https://doi.org/10.1016/B978-0-08-025443-2.50021-5>.
- [41] E. M. Arruda and M. C. Boyce. “A three-dimensional constitutive model for the large stretch behavior of rubber elastic materials”, *Journal of the Mechanics and Physics of Solids*, **41**(2): 389–412, (1993). DOI:[10.1016/0022-5096\(93\)90013-6](https://doi.org/10.1016/0022-5096(93)90013-6).
- [42] M. A. Biot. “General theory of three-dimensional consolidation”, *Journal of Applied Physics*, **12**(2): 155–164, (1941). DOI:[10.1063/1.1712886](https://doi.org/10.1063/1.1712886).
- [43] T. Komori, M. Itoh, and A. Takaku. “A model analysis of the compressibility of fiber assemblies”, *Textile Research Journal*, **62**(10): 567–574, (1992). DOI:[10.1177/004051759206201002](https://doi.org/10.1177/004051759206201002).
- [44] O. V. Kim, X. Liang, R. I. Litvinov, J. W. Weisel, M. S. Alber, and P. K. Purohit. “Foam-like compression behavior of fibrin networks”, *Biomechanics and Modeling in Mechanobiology*, **15**(1): 213–228, (2016). DOI:[10.1007/s10237-015-0683-z](https://doi.org/10.1007/s10237-015-0683-z).
- [45] L. J. Gibson and M. F. Ashby. *Cellular Solids: Structure and Properties*. New York: Cambridge University Press, New York, (1999).
- [46] R. Abeyaratne and J. K. Knowles. *Evolution of Phase Transitions: A Continuum Theory*. Cambridge, U.K.: Cambridge University Press, Cambridge, U.K., (2006).
- [47] G. Verhille, S. Moulinet, N. Vandenberghe, M. Adda-Bedia, and P. L. Gal. “Structure and mechanics of aegagropilae fiber network”, *Proceedings of the National Academy of Sciences*, **114**(18): 4607–4612, (2017). DOI:[10.1073/pnas.1620688114](https://doi.org/10.1073/pnas.1620688114).
- [48] A. Ed-Daoui and P. Snabre. “Poroviscoelasticity and compression-softening of agarose hydrogels”, *Rheologica Acta*, **60**: 327–351, (2021). DOI:[10.1007/s00397-021-01267-3](https://doi.org/10.1007/s00397-021-01267-3).
- [49] H. J. Qi, C. Ortiz, and M. C. Boyce. “Mechanics of biomacromolecular networks containing folded domains”, *Journal of Engineering Materials and Technology, Transactions of the ASME*, **128**(4): 509–518, (2006). DOI:[10.1115/1.2345442](https://doi.org/10.1115/1.2345442).
- [50] A. E. X. Brown, R. I. Litvinov, D. E. Discher, P. K. Purohit, and J. W. Weisel. “Multiscale mechanics of fibrin polymer: Gel stretching with protein unfolding and loss of water”, *Science*, **325**(5941): 741–744, (2009). DOI:[10.1126/science.1172484](https://doi.org/10.1126/science.1172484).

- [51] P. K. Purohit, R. I. Litvinov, A. E. X. Brown, D. E. Discher, and J. W. Weisel. “Protein unfolding accounts for the unusual mechanical behavior of fibrin networks”, *Acta Biomaterialia*, **7**: 2374–2383, (2011). DOI:10.1016/j.actbio.2011.02.026.
- [52] J. W. Weisel and R. I. Litvinov. *Fibrin Formation, Structure and Properties* : ch. 13, 405–456. Cham: Springer International Publishing, (2017). DOI:10.1007/978-3-319-49674-0_13.
- [53] J. W. Weisel, C. Nagaswami, and L. Makowski. “Twisting of fibrin fibers limits their radial growth”, *Proceedings of the National Academy of Sciences of the United States of America*, **84**: 8991–8995, (1987). DOI:10.1007/s10704-012-9758-3.
- [54] O. V. Kim, R. I. Litvinov, M. S. Alber, and J. W. Weisel. “Quantitative structural mechanobiology of platelet-driven blood clot contraction”, *Nature Communications*, **8**(1): 1274, (2017). DOI:10.1038/s41467-017-00885-x.
- [55] W. A. Lam, O. Chaudhuri, A. Crow, K. D. Webster, T.-D. Li, A. Kita, J. Huang, and D. A. Fletcher. “Mechanics and contraction dynamics of single platelets and implications for clot stiffening”, *Nature Materials*, **10**: 61–66, (2011). DOI:10.1038/nmat2903.
- [56] Y. Sun, O. Oshinowo, D. R. Myers, W. A. Lam, and A. Alexeev. “Resolving the missing link between single platelet force and clot contractile force”, *iScience*, **25**(1): 103690, (2022). DOI:10.1016/j.isci.2021.103690.
- [57] J. W. Weisel and C. Nagaswami. “Computer modeling of fibrin polymerization kinetics correlated with electron microscope and turbidity observations: clot structure and assembly are kinetically controlled”, *Biophysical Journal*, **63**: 111–128, (1992). DOI:10.1016/S0006-3495(92)81594-1.
- [58] N. E. Hudson. “Biophysical mechanisms mediating fibrin fiber lysis”, *BioMed Research International*, **2017**: 2748340, (2017). DOI:10.1155/2017/2748340.
- [59] W. Li, T. Lucioni, R. Li, K. Bonin, S. S. Cho, and M. Guthold. “Stretching single fibrin fibers hampers their lysis”, *Acta Biomaterialia*, **60**: 264–274, (2017). DOI:10.1016/j.actbio.2017.07.037.
- [60] S. J. Cone, A. T. Fuquay, J. M. Litofsky, T. C. Dement, C. A. Carolan, and N. E. Hudson.

- “Inherent fibrin fiber tension propels mechanisms of network clearance during fibrinolysis”, *Acta Biomaterialia*, **107**: 164–177, (2020). DOI:10.1016/j.actbio.2020.02.025.
- [61] I. VARJÚ, P. SÓTONYI, R. MACHOVICH, L. SZABÓ, K. TENEKEDJIEV, M. M. C. G. SILVA, C. LONGSTAFF, and K. KOLEV. “Hindered dissolution of fibrin formed under mechanical stress”, *Journal of Thrombosis and Haemostasis*, **9**(5): 979–986, (2011). DOI:10.1111/j.1538-7836.2011.04203.x.
- [62] T. Feller, S. D. A. Connell, and R. A. S. Ariëns. “Why fibrin biomechanical properties matter for hemostasis and thrombosis”, *Journal of Thrombosis and Haemostasis*, **20**(1): 6–16, (2022). DOI:10.1111/jth.15531.
- [63] X. Liang, I. Chernysh, P. K. Purohit, and J. W. Weisel. “Phase transitions during compression and decompression of clots from platelet-poor plasma, platelet-rich plasma and whole blood”, *Acta Biomaterialia*, **60**: 275–290, (2017). DOI:10.1016/j.actbio.2017.07.011.
- [64] O. V. Kim, R. I. Litvinov, J. Chen, D. Z. Chen, J. W. Weisel, and M. S. Alber. “Compression-induced structural and mechanical changes of fibrin-collagen composites”, *Matrix Biology*, **60-61**: 141–156, (2017). DOI:10.1016/j.matbio.2016.10.007.
- [65] S. Duffy, M. Farrell, K. McArdle, J. Thornton, D. Vale, E. Rainsford, L. Morris, D. S. Liebeskind, E. MacCarthy, and M. Gilvarry. “Novel methodology to replicate clot analogs with diverse composition in acute ischemic stroke”, *Journal of NeuroInterventional Surgery*, **9**(5): 486–491, (2017). DOI:10.1136/neurintsurg-2016-012308.
- [66] J. Gralla, G. Schroth, L. Remonda, K. Nedeltchev, J. Slotboom, and C. Brekenfeld. “Mechanical thrombectomy for acute ischemic stroke: Thrombus-device interaction, efficiency, and complications in vivo”, *Stroke*, **37**(12): 3019–3024, (2006). DOI:10.1161/01.STR.0000248457.55493.85.
- [67] J. E. FRENCH. “The structure of natural and experimental thrombi.”, *Annals of the Royal College of Surgeons of England*, **36**: 191–200, (1965).
- [68] R. Spiewak, A. Gosselin, D. Merinov, R. I. Litvinov, J. W. Weisel, V. Tutwiler, and P. K. Purohit. “Biomechanical origins of inherent tension in fibrin networks”, *Journal of the Mechanical Behavior of Biomedical Materials*, (In Preparation).

- [69] V. Tutwiler, J. Singh, R. I. Litvinov, J. L. Bassani, P. K. Purohit, and J. W. Weisel. “Rupture of blood clots: Mechanics and pathophysiology”, *Science Advances*, **6**(35): eabc0496, (2020). DOI:10.1126/sciadv.abc0496.
- [70] S. Liu, G. Bao, Z. Ma, C. J. Kastrup, and J. Li. “Fracture mechanics of blood clots: Measurements of toughness and critical length scales”, *Extreme Mechanics Letters*, **48**: 101444, (2021). DOI:https://doi.org/10.1016/j.eml.2021.101444.
- [71] W. Liu, L. M. Jawerth, E. A. Sparks, M. R. Falvo, R. R. Hantgan, R. Superfine, S. T. Lord, and M. Guthold. “Fibrin fibers have extraordinary extensibility and elasticity”, *Science*, **313**(5787): 634–634, (2006). DOI:10.1126/science.1127317.
- [72] H. Fukuzumi, T. Saito, T. Iwata, Y. Kumamoto, and A. Isogai. “Transparent and High Gas Barrier Films of Cellulose Nanofibers Prepared by TEMPO-Mediated Oxidation”, *Biomacromolecules*, **10**(1): 162–165, (Jan. 2009). DOI:10.1021/bm801065u.
- [73] A. Isogai. “Wood nanocelluloses: fundamentals and applications as new bio-based nanomaterials”, *Journal of Wood Science*, **59**(6): 449–459, (Dec. 2013). DOI:10.1007/s10086-013-1365-z.
- [74] S. Paunonen. “Strength and Barrier Enhancements of Cellophane and Cellulose Derivative Films: A Review”, *BioResources*, **8**: 3098–3121, (2013). DOI:10.15376/BIORES.8.2.3098-3121.
- [75] F. J. Schmied, C. Teichert, L. Kappel, U. Hirn, W. Bauer, and R. Schennach. “What holds paper together: Nanometre scale exploration of bonding between paper fibres”, *SCIENTIFIC REPORTS*, **3**: 2432–2438, (2013). DOI:10.1038/srep02432.
- [76] U. Hirn. “Comprehensive analysis of individual pulp fiber bonds quantifies the mechanisms of fiber bonding in paper”, *Scientific Reports*, **5**: 10503, (2015). DOI:10.1038/srep10503.
- [77] A. Tanaka and T. Yamauchi. “Deformation and fracture of paper during the in-plane fracture toughness testing—Examination of the essential work of fracture method”, *Journal of Materials Science*, **35**: 1827–1833, (2000). DOI:10.1023/A:1004797023064.
- [78] S. J. Pathare, W. Eng, S.-J. J. Lee, and A. K. Ramasubramanian. “Fibrin prestress due to

- platelet aggregation and contraction increases clot stiffness”, *Biophysical Reports*, **1**(2): 100022, (2021). DOI:10.1016/j.bpr.2021.100022.
- [79] S. Britton, O. Kim, F. Pancaldi, Z. Xu, R. I. Litvinov, J. W. Weisel, and M. Alber. “Contribution of nascent cohesive fiber-fiber interactions to the non-linear elasticity of fibrin networks under tensile load”, *Acta Biomaterialia*, **94**: 514–523, (2019). DOI:10.1016/j.actbio.2019.05.068.
- [80] W. LIU, C. R. CARLISLE, E. A. SPARKS, and M. GUTHOLD. “The mechanical properties of single fibrin fibers”, *Journal of Thrombosis and Haemostasis*, **8**(5): 1030–1036, (2010). DOI:10.1111/j.1538-7836.2010.03745.x.
- [81] J.-P. Collet, H. Shuman, R. E. Ledger, S. Lee, and J. W. Weisel. “The elasticity of an individual fibrin fiber in a clot”, *Proceedings of the National Academy of Sciences*, **102**(26): 9133–9137, (2005). DOI:10.1073/pnas.0504120102.
- [82] A. Zhang, H. Jiang, Z. Wu, C. Wu, and B. Qian. “Internal stress, lattice deformation, and modulus of polymers”, *Journal of Applied Polymer Science*, **42**(6): 1779–1791, (1991). DOI:https://doi.org/10.1002/app.1991.070420635.
- [83] Y. Li, A. Nese, X. Hu, N. V. Lebedeva, T. W. LaJoie, J. Burdyńska, M. C. Stefan, W. You, W. Yang, K. Matyjaszewski, and S. S. Sheiko. “Shifting electronic structure by inherent tension in molecular bottlebrushes with polythiophene backbones”, *ACS Macro Letters*, **3**(8): 738–742, (2014). DOI:10.1021/mz5003323.
- [84] J. Torbet, J. M. Freyssinet, and G. Hudry-Clergeon. “Oriented fibrin gels formed by polymerization in strong magnetic fields”, *Nature*, **289**: 91–93, (January 1981). DOI:10.1038/289091a0.
- [85] G. Caracciolo, M. De Spirito, A. C. Castellano, D. Pozzi, G. Amiconi, A. De Pascalis, R. Caminiti, and G. Arcovito. “Protofibrils within fibrin fibres are packed together in a regular array”, *Thrombosis and Haemostasis*, **89**(04): 632–636, (2003). DOI:10.1055/s-0037-1613569.
- [86] C. Yeromonahos, B. Polack, and F. Caton. “Nanostructure of the fibrin clot”, *Biophysical Journal*, **99**(7): 2018–2027, (2010). DOI:10.1016/j.bpj.2010.04.059.

- [87] G. Portale and J. Torbet. “Complex strain induced structural changes observed in fibrin assembled in human plasma”, *Nanoscale*, **10**: 10063–10072, (2018). DOI:10.1039/C8NR00353J.
- [88] K. A. Jansen, A. Zhmurov, B. E. Vos, G. Portale, D. Hermida-Merino, R. I. Litvinov, V. Tutwiler, N. A. Kurniawan, W. Bras, J. W. Weisel, V. Barsegov, and G. H. Koenderink. “Molecular packing structure of fibrin fibers resolved by x-ray scattering and molecular modeling”, *Soft Matter*, **16**: 8272–8283, (2020). DOI:10.1039/D0SM00916D.
- [89] J. W. Weisel, G. N. Phillips Jr., and C. Cohen. “The structure of fibrinogen and fibrin: Ii. architecture of the fibrin clot*”, *Annals of the New York Academy of Sciences*, **408**(1): 367–379, (1983). DOI:10.1111/j.1749-6632.1983.tb23257.x.
- [90] J. W. Weisel. “The electron microscope band pattern of human fibrin: Various stains, lateral order, and carbohydrate localization”, *Journal of Ultrastructure and Molecular Structure Research*, **96**(1): 176–188, (1986). DOI:10.1016/0889-1605(86)90019-4.
- [91] A. Zhmurov, A. D. Protopopova, R. I. Litvinov, P. Zhukov, J. W. Weisel, and V. Barsegov. “Atomic structural models of fibrin oligomers”, *Structure*, **26**: 857–868, (2018). DOI:10.1016/j.str.2018.04.005.
- [92] J. W. Weisel. “Molecular symmetry and binding sites in fibrin assembly”, *Thrombosis Research*, **48**(5): 615–617, (1987). DOI:10.1016/0049-3848(87)90395-1.
- [93] I. S. Yermolenko, V. K. Lishko, T. P. Ugarova, and S. N. Magonov. “High-resolution visualization of fibrinogen molecules and fibrin fibers with atomic force microscopy”, *Biomacromolecules*, **12**(2): 370–379, (2011). DOI:10.1021/bm101122g.
- [94] L. Medved’, T. Ugarova, Y. Veklich, N. Lukinova, and J. Weisel. “Electron microscope investigation of the early stages of fibrin assembly: Twisted protofibrils and fibers”, *Journal of Molecular Biology*, **216**(3): 503–509, (1990). DOI:10.1016/0022-2836(90)90376-W.
- [95] G. M. Grason. “Frustration and packing in curved-filament assemblies: from isometric to isomorphic bundles”, *Soft Matter*, **9**: 6761–6772, (2013). DOI:10.1039/C3SM50229E.
- [96] D. W. Atkinson, C. D. Santangelo, and G. M. Grason. “Mechanics of metric frustration in contorted filament bundles: From local symmetry to columnar elasticity”, *Phys. Rev. Lett.*, **127**: 218002, (Nov 2021). DOI:10.1103/PhysRevLett.127.218002.

- [97] S. A. Chester and L. Anand. “A coupled theory of fluid permeation and large deformations for elastomeric materials”, *Journal of the Mechanics and Physics of Solids*, **58**: 1879–1906, (2010). DOI:10.1016/j.jmps.2010.07.020.
- [98] I. N. Chernysh, C. Nagaswami, and J. W. Weisel. “Visualization and identification of the structures formed during early stages of fibrin polymerization”, *Blood*, **117**(17): 4609–4614, (2011). DOI:10.1182/blood-2010-07-297671.
- [99] H. P. Erickson and W. E. Fowler. “Electron microscopy of fibrinogen, its plasmic fragments and small polymers”, *Annals of the New York Academy of Sciences*, **408**(1): 146–163, (1983). DOI:10.1111/j.1749-6632.1983.tb23242.x.
- [100] J. S. Palmer and M. C. Boyce. “Constitutive modeling of the stress-strain behavior of f-actin filament networks”, *Acta Biomaterialia*, **4**(3): 597–612, (2008). DOI:10.1016/j.actbio.2007.12.007.
- [101] M. Nizette and A. Goriely. “Towards a classification of euler–kirchhoff filaments”, *Journal of Mathematical Physics*, **40**(6): 2830–2866, (1999). DOI:10.1063/1.532731.
- [102] A. Zhmurov, A. D. Protopopova, R. I. Litvinov, P. Zhukov, M. J. W. W. Alexander R, and V. Barsegov. “Structural basis of interfacial flexibility in fibrin oligomers”, *Structure*, **24**: 1907–1917, (2016). DOI:10.1016/j.str.2016.08.009.
- [103] R. Raj and P. K. Purohit. “Phase boundaries as agents of structural change in macromolecules”, *Journal of the Mechanics and Physics of Solids*, **59**: 2044–2069, (2011). DOI:10.1016/j.jmps.2011.07.003.
- [104] C. Brennen and H. Winet. “Fluid mechanics of propulsion by cilia and flagella”, *Annual Review of Fluid Mechanics*, **9**: 339–398, (1977). DOI:10.1146/annurev.fl.09.010177.002011.
- [105] O. V. Kim, R. I. Litvinov, J. W. Weisel, and M. S. Alber. “Structural basis for the nonlinear mechanics of fibrin networks under compression”, *Biomaterials*, **35**(25): 6739–6749, (2014). DOI:10.1016/j.biomaterials.2014.04.056.
- [106] N. E. Hudson, F. Ding, I. Bucay, E. T. O’Brien, III, O. V. Gorkun, R. Superfine, S. T. Lord, N. V. Dokholyan, and M. R. Falvo. “Submillisecond elastic recoil reveals molecu-

- lar origins of fibrin fiber mechanics”, *Biophysical Journal*, **102**(12): 2671–2680, (2013). DOI:10.1016/j.bpj.2013.04.052.
- [107] J. E. Bischoff, E. M. Arruda, and K. Grosh. “A new constitutive model for the compressibility of elastomers at finite deformations”, *Rubber Chemistry and Technology*, **74**(4): 541–559, (2001). DOI:10.5254/1.3544956.
- [108] Z. Yang, I. Mochalkin, and R. F. Doolittle. “A model of fibrin formation based on crystal structures of fibrinogen and fibrin fragments complexed with synthetic peptides”, *Proceedings of the National Academy of Sciences*, **97**(26): 14156–14161, (2000). DOI:10.1073/pnas.97.26.14156.
- [109] M. Guthold, W. Liu, B. Stephens, S. T. Lord, R. R. Hantgan, D. A. Erie, R. M. Taylor, Jr., and R. Superfine. “Visualization and mechanical manipulations of individual fibrin fibers suggest that fiber cross section has fractal dimension 1.3”, *Biophysical Journal*, **87**(6): 4226–4236, (December 2004). DOI:10.1529/biophysj.104.042333.
- [110] W. Li, J. Sigley, M. Pieters, C. C. Helms, C. Nagaswami, J. W. Weisel, and M. Guthold. “Fibrin fiber stiffness is strongly affected by fiber diameter, but not by fibrinogen glycation”, *Biophysical Journal*, **110**(6): 1400–1410, (March 2016). DOI:10.1016/j.bpj.2016.02.021.
- [111] W. Li, J. Sigley, S. Baker, C. Helms, M. Kinney, M. Pieters, P. Brubaker, R. Cubcciotti, and M. Guthold. “Nonuniform internal structure of fibrin fibers: Protein density and bond density strongly decrease with increasing diameter”, *BioMed Research International*, **2017**: 6385628, (October 2017). DOI:10.1155/2017/6385628.
- [112] S. R. Lynch, S. M. Laverty, B. E. Bannish, and N. E. Hudson. “Microscale structural changes of individual fibrin fibers during fibrinolysis”, *Acta Biomaterialia*, (2022). DOI:10.1016/j.actbio.2022.01.006.
- [113] J. C. Maxwell, F.R.S. “L. on the calculation of the equilibrium and stiffness of frames”, *The London, Edinburgh, and Dublin Philosophical Magazine and Journal of Science*, **27**(182): 294–299, (1864). DOI:10.1080/14786446408643668.
- [114] M. Vahabi, A. Sharma, A. J. Licup, A. S. G. van Oosten, P. A. Galie, P. A. Janmey, and F. C. MacKintosh. “Elasticity of fibrous networks under uniaxial prestress”, *Soft Matter*, **12**: 5050–5060, (2016). DOI:10.1039/C6SM00606J.

- [115] S. Arzash, J. L. Shivers, A. J. Licup, A. Sharma, and F. C. MacKintosh. “Stress-stabilized subisostatic fiber networks in a ropelike limit”, *Phys. Rev. E*, **99**: 042412, (Apr 2019). DOI:10.1103/PhysRevE.99.042412.
- [116] D. A. Head, A. J. Levine, and F. C. MacKintosh. “Deformation of cross-linked semiflexible polymer networks”, *Phys. Rev. Lett.*, **91**: 108102, (Sep 2003). DOI:10.1103/PhysRevLett.91.108102.
- [117] G. H. Koenderink, Z. Dogic, F. Nakamura, P. M. Bendix, F. C. MacKintosh, J. H. Hartwig, T. P. Stossel, and D. A. Weitz. “An active biopolymer network controlled by molecular motors”, *Proceedings of the National Academy of Sciences*, **106**(36): 15192–15197, (2009). DOI:10.1073/pnas.0903974106.
- [118] K. A. Jansen, R. G. Bacabac, I. K. Piechocka, and G. H. Koenderink. “Cells actively stiffen fibrin networks by generating contractile stress”, , **105**(10): 2240–2251, (NOVEMBER 2013). DOI:10.1016/j.bpj.2013.10.008.
- [119] T. Su and P. K. Purohit. “Semiflexible filament networks viewed as fluctuating beam-frames”, *Soft Matter*, **8**: 4664–4674, (2012). DOI:10.1039/C2SM07058H.
- [120] R. Al Dieri, F. Peyvandi, E. Santagostino, M. Giansily, P. M. Mannucci, J. F. Schved, S. Béguin, and H. C. Hemker. “The thrombogram in rare inherited coagulation disorders: Its relation to clinical bleeding”, *Thrombosis and Haemostasis*, **88**(4): 576–582, (2002). DOI:10.1055/s-0037-1613258.
- [121] A. S. Wolberg, M. M. Aleman, K. Leiderman, and K. R. Machlus. “Procoagulant activity in hemostasis and thrombosis: Virchow’s triad revisited”, *Anesthesia and Analgesia*, **114**(2): 275–285, (2012). DOI:10.1213/ANE.0b013e31823a088c.
- [122] L. Wilhelmsen, K. Svardsudd, K. Korsan-Bengtson, B. Larsson, L. Welin, and G. Tibblin. “Fibrinogen as a risk factor for stroke and myocardial infarction”, *New England Journal of Medicine*, **311**(8): 501–505, (1984). DOI:10.1056/NEJM198408233110804.
- [123] G. A. Allen, A. S. Wolberg, J. A. Oliver, M. Hoffman, H. R. Roberts, and D. M. Monroe. “Impact of procoagulant concentration on rate, peak and total thrombin generation in a model system”, *Journal of Thrombosis and Haemostasis*, **2**(3): 402–413, (2004). DOI:10.1111/j.1538-7933.2003.00617.x.

- [124] D. A. Gorog, Z. A. Fayad, and V. Fuster. “Arterial thrombus stability: Does it matter and can we detect it?”, *Journal of the American College of Cardiology*, **70**(16): 2036–2047, (2017). DOI:10.1016/j.jacc.2017.08.065.
- [125] A. M. Wendelboe and G. E. Raskob. “Global burden of thrombosis: Epidemiologic aspects”, *Circulation Research*, **118**(9): 1340–1347, (2016). DOI:10.1161/CIRCRESAHA.115.306841.
- [126] S. Lauber, A. Limacher, T. Tritschler, O. Stalder, M. Méan, M. Righini, M. Aschwanden, J. H. Beer, B. Frauchiger, J. Osterwalder, N. Kucher, B. Lämmle, J. Cornuz, A. Angelillo-Scherrer, C. M. Matter, M. Husmann, M. Banyai, D. Staub, L. Mazzolai, O. Hugli, N. Rodondi, and D. Aujesky. “Predictors and outcomes of recurrent venous thromboembolism in elderly patients”, *American Journal of Medicine*, **131**(6): 703.e7–703.e16, (2018). DOI:10.1016/j.amjmed.2017.12.015.
- [127] J. W. G. Yarnell, I. A. Baker, P. M. Sweetnam, D. Bainton, J. R. O’Brien, P. J. Whitehead, and P. C. Elwood. “Fibrinogen, viscosity, and white blood cell count are major risk factors for ischemic heart disease. the caerphilly and speedwell collaborative heart disease studies”, *Circulation*, **83**(3): 836–844, (1991). DOI:10.1161/01.cir.83.3.836.
- [128] J. A. Heit. “Epidemiology of venous thromboembolism”, *Nature Reviews Cardiology*, **12**(8): 464–474, (2015). DOI:10.1038/nrcardio.2015.83.
- [129] S. R. Poort, F. R. Rosendaal, P. H. Reitsma, and R. M. Bertina. “A common genetic variation in the 3’-untranslated region of the prothrombin gene is associated with elevated plasma prothrombin levels and an increase in venous thrombosis”, *Blood*, **88**(10): 3698–3703, (1996). DOI:10.1182/blood.v88.10.3698.bloodjournal188103698.
- [130] O. K. Baskurt and H. J. Meiselman. “Red blood cell mechanical stability test”, *Clinical Hemorheology and Microcirculation*, **55**(1): 55–62, (2013). DOI:10.3233/CH-131689.
- [131] A. L. C. La Corte, H. Philippou, and R. A. S. Arins. “Role of fibrin structure in thrombosis and vascular disease”, *Advances in Protein Chemistry and Structural Biology*, **83**: 75–127, (2011). DOI:10.1016/B978-0-12-381262-9.00003-3.
- [132] D. L. Bark and D. N. Ku. “Wall shear over high degree stenoses pertinent to atherothrombosis”, *Journal of Biomechanics*, **43**(15): 2970–2977, (2010). DOI:10.1016/j.jbiomech.2010.07.011.

- [133] J. J. Hathcock. “Flow effects on coagulation and thrombosis”, *Arteriosclerosis, Thrombosis, and Vascular Biology*, **26**(8): 1729–1737, (2006). DOI:10.1161/01.ATV.0000229658.76797.30.
- [134] J.-J. Chiu and S. Chien. “Effects of disturbed flow on vascular endothelium: Pathophysiological basis and clinical perspectives”, *Physiological Reviews*, **91**(1): 327–387, (2011). DOI:10.1152/physrev.00047.2009.
- [135] P. F. Davies. “Hemodynamic shear stress and the endothelium in cardiovascular pathophysiology”, *Nature Clinical Practice Cardiovascular Medicine*, **6**(1): 16–26, (2009). DOI:10.1038/ncpcardio1397.
- [136] E. Di Martino, S. Mantero, F. Inzoli, G. Melissano, D. Astore, R. Chiesa, and R. Fumero. “Biomechanics of abdominal aortic aneurysm in the presence of endoluminal thrombus: Experimental characterisation and structural static computational analysis”, *European Journal of Vascular and Endovascular Surgery*, **15**(4): 290–299, (1998). DOI:10.1016/S1078-5884(98)80031-2.
- [137] J. P. Vande Geest, M. S. Sacks, and D. A. Vorp. “A planar biaxial constitutive relation for the luminal layer of intra-luminal thrombus in abdominal aortic aneurysms”, *Journal of Biomechanics*, **39**(13): 2347–2354, (2006). DOI:10.1016/j.jbiomech.2006.05.011.
- [138] Z. Teng, J. Feng, Y. Zhang, Y. Huang, M. P. F. Sutcliffe, A. J. Brown, Z. Jing, J. H. Gillard, and Q. Lu. “Layer- and direction-specific material properties, extreme extensibility and ultimate material strength of human abdominal aorta and aneurysm: A uniaxial extension study”, *Annals of Biomedical Engineering*, **43**(11): 2745–2759, (2015). DOI:10.1007/s10439-015-1323-6.
- [139] J. Y. Chueh, A. K. Wakhloo, G. H. Hendricks, C. F. Silva, J. P. Weaver, and M. J. Gounis. “Mechanical characterization of thromboemboli in acute ischemic stroke and laboratory embolus analogs”, *American Journal of Neuroradiology*, **32**(7): 1237–1244, (2011). DOI:10.3174/ajnr.A2485.
- [140] J. H. Ashton, J. P. Vande Geest, B. R. Simon, and D. G. Haskett. “Compressive mechanical properties of the intraluminal thrombus in abdominal aortic aneurysms and fibrin-based thrombus mimics”, *Journal of Biomechanics*, **42**(3): 197–201, (2009). DOI:10.1016/j.jbiomech.2008.10.024.

- [141] Y. Veklich, C. W. Francis, J. White, and J. W. Weisel. “Structural studies of fibrinolysis by electron microscopy”, *Blood*, **92**(12): 4721–4729, (1998). DOI:10.1182/blood.v92.12.4721.
- [142] J. P. Collet, G. Montalescot, C. Lesty, and J. W. Weisel. “A structural and dynamic investigation of the facilitating effect of glycoprotein iib/iiia inhibitors in dissolving platelet-rich clots”, *Circulation Research*, **90**(4): 428–434, (2002). DOI:10.1161/hh0402.105095.
- [143] J.-P. Collet, C. Lesty, G. Montalescot, and J. W. Weisel. “Dynamic changes of fibrin architecture during fibrin formation and intrinsic fibrinolysis of fibrin-rich clots”, *Journal of Biological Chemistry*, **278**(24): 21331–21335, (2003). DOI:10.1074/jbc.M212734200.
- [144] J. Noailly, H. Van Oosterwyck, W. Wilson, T. M. Quinn, and K. Ito. “A poroviscoelastic description of fibrin gels”, *Journal of Biomechanics*, **41**(15): 3265–3269, (2008). DOI:10.1016/j.jbiomech.2008.09.002.
- [145] M. Dao, C. T. Lim, and S. Suresh. “Mechanics of the human red blood cell deformed by optical tweezers”, *Journal of the Mechanics and Physics of Solids*, **51**(11-12): 2259–2280, (2003). DOI:10.1016/j.jmps.2003.09.019.
- [146] C. T. Lim, M. Dao, S. Suresh, C. H. Sow, and K. T. Chew. “Large deformation of living cells using laser traps”, *Acta Materialia*, **52**(7): 1837–1845, (2004). DOI:10.1016/j.actamat.2003.12.028.
- [147] J. C. Simo and K. S. Pister. “Remarks on rate constitutive equations for finite deformation problems: computational implications”, *Computer Methods in Applied Mechanics and Engineering*, **46**(2): 201–215, (1984). DOI:10.1016/0045-7825(84)90062-8.
- [148] E. A. Evans and R. M. Hochmuth. “Membrane viscoelasticity”, *Biophysical Journal*, **16**(1): 1–11, (1976). DOI:10.1016/S0006-3495(76)85658-5.
- [149] R. M. Hochmuth, P. R. Worthy, and E. A. Evans. “Red cell extensional recovery and the determination of membrane viscosity”, *Biophysical Journal*, **26**(1): 101–114, (1979). DOI:10.1016/S0006-3495(79)85238-8.
- [150] R. W. Ogden. *Non-linear Elastic Deformations*. North Chelmsford, MA: Courier Corporation, North Chelmsford, MA, (1997).

- [151] V. Fineschi, E. Turillazzi, M. Neri, C. Pomara, and I. Riezzo. “Histological age determination of venous thrombosis: A neglected forensic task in fatal pulmonary thrombo-embolism”, *Forensic Science International*, **186**(1-3): 22–28, (2009). DOI:10.1016/j.forsciint.2009.01.006.
- [152] J. R. Raney, F. Fraternali, and C. Daraio. “Rate-independent dissipation and loading direction effects in compressed carbon nanotube arrays”, *Nanotechnology*, **24**(25): 255707, (2013). DOI:10.1088/0957-4484/24/25/255707.
- [153] D. B. Cines, T. Lebedeva, C. Nagaswami, V. Hayes, W. Masefski, R. I. Litvinov, L. Rauova, T. J. Lowery, and J. W. Weisel. “Clot contraction: Compression of erythrocytes into tightly packed polyhedra and redistribution of platelets and fibrin”, *Blood*, **123**(10): 1596–1603, (2014). DOI:10.1182/blood-2013-08-523860.
- [154] S. Johnson, S. Duffy, G. Gunning, M. Gilvarry, J. P. McGarry, and P. E. McHugh. “Review of mechanical testing and modelling of thrombus material for vascular implant and device design”, *Annals of Biomedical Engineering*, **45**(11): 2494–2508, (2017). DOI:10.1007/s10439-017-1906-5.
- [155] T. C. Gasser, G. Görgülü, M. Folkesson, and J. Swedenborg. “Failure properties of intraluminal thrombus in abdominal aortic aneurysm under static and pulsating mechanical loads”, *Journal of Vascular Surgery*, **48**(1): 179–188, (2008). DOI:10.1016/j.jvs.2008.01.036.
- [156] M. K. Rausch and J. D. Humphrey. “A microstructurally inspired damage model for early venous thrombus”, *Journal of the Mechanical Behavior of Biomedical Materials*, **55**: 12–20, (2016). DOI:10.1016/j.jmbbm.2015.10.006.
- [157] E. Saldívar, J. N. Orje, and Z. M. Ruggeri. “Tensile destruction test as an estimation of partial proteolysis in fibrin clots”, *American Journal of Hematology*, **71**(2): 119–127, (2002). DOI:10.1002/ajh.10199.
- [158] E. A. Van Dam, S. D. Dams, G. W. M. Peters, M. C. M. Rutten, G. W. H. Schurink, J. Buth, and F. N. Van De Vosse. “Non-linear viscoelastic behavior of abdominal aortic aneurysm thrombus”, *Biomechanics and Modeling in Mechanobiology*, **7**(2): 127–137, (2008). DOI:10.1007/s10237-007-0080-3.

- [159] T. H. S. Van Kempen, A. C. B. Bogaerds, G. W. M. Peters, and F. N. Van De Vosse. “A constitutive model for a maturing fibrin network”, *Biophysical Journal*, **107**(2): 504–513, (2014). DOI:10.1016/j.bpj.2014.05.035.
- [160] C. L. Slaboch, M. S. Alber, E. D. Rosen, and T. C. Ovaert. “Mechano-rheological properties of the murine thrombus determined via nanoindentation and finite element modeling”, *Journal of the Mechanical Behavior of Biomedical Materials*, **10**: 75–86, (2012). DOI:10.1016/j.jmbbm.2012.02.012.
- [161] H. Xie, K. Kim, S. R. Aglyamov, S. Y. Emelianov, M. O’Donnell, W. F. Weitzel, S. K. Wroblewski, D. D. Myers, T. W. Wakefield, and J. M. Rubin. “Correspondence of ultrasound elasticity imaging to direct mechanical measurement in aging dvt in rats”, *Ultrasound in Medicine and Biology*, **31**(10): 1351–1359, (2005). DOI:10.1016/j.ultrasmedbio.2005.06.005.
- [162] M. K. Rausch and J. D. Humphrey. “A computational model of the biochemomechanics of an evolving occlusive thrombus”, *Journal of Elasticity*, **129**(1-2): 125–144, (2017). DOI:10.1007/s10659-017-9626-5.
- [163] R. Spiewak, G. S. Vankayalapati, J. M. Considine, K. T. Turner, and P. K. Purohit. “Humidity dependence of fracture toughness of cellulose fibrous networks”, *Engineering Fracture Mechanics*, **264**: 108330, (2022). DOI:10.1016/j.engfracmech.2022.108330.
- [164] D. M. S. Wanigaratne, *Investigation of An Alternative Technique to Measure Fracture Toughness of Paper*. Ph.D. dissertation, MONASH University, (2004).
- [165] J. Tryding, G. Marin, M. Nygård, P. Mäkelä, and G. Ferrari. “Experimental and theoretical analysis of in-plane cohesive testing of paperboard”, *International Journal of Damage Mechanics*, **26**(6): 895–918, (Aug. 2017). DOI:10.1177/1056789516630776.
- [166] J. Zechner, M. Janko, and O. Kolednik. “Determining the fracture resistance of thin sheet fiber composites – Paper as a model material”, *Composites Science and Technology*, **74**: 43–51, (Jan. 2013). DOI:10.1016/j.compscitech.2012.10.007.
- [167] D. Wanigaratne, W. Batchelor, and I. Parker. “Comparison of Fracture Toughness of Paper with Tensile Properties”, in *55th Appita Annual Conference, Hobart, Australia 30 April-2 May 2001: Proceedings*: 217–223, Appita Inc., (2001).

- [168] S. Golling, D. Frømeta, D. Casellas, an Granstr om, P. Jonsén, and M. Oldenburg. “Determination of the essential work of fracture at high strain rates”, in *6th International Conference Hot Sheet Metal Forming of High-Performance Steel CHS2*: 261–269, Association for Iron & Steel Technology, (2017).
- [169] H. Zhu, S. Zhu, Z. Jia, S. Parvinian, Y. Li, O. Vaaland, L. Hu, and T. Li. “Anomalous scaling law of strength and toughness of cellulose nanopaper”, *Proceedings of the National Academy of Sciences*, **112**(29): 8971–8976, (July 2015). DOI:10.1073/pnas.1502870112.
- [170] R. Mao, S. Goutianos, W. Tu, N. Meng, G. Yang, L. A. Berglund, and T. Peijs. “Comparison of fracture properties of cellulose nanopaper, printing paper and buckypaper”, *Journal of Materials Science*, **52**(16): 9508–9519, (Aug. 2017). DOI:10.1007/s10853-017-1108-4.
- [171] P. Mäkelä and S. Östlund. “Cohesive crack modelling of thin sheet material exhibiting anisotropy, plasticity and large-scale damage evolution”, *Engineering Fracture Mechanics*, **79**: 50–60, (2012). DOI:<https://doi.org/10.1016/j.engfracmech.2011.10.001>.
- [172] Q. Meng, B. Li, T. Li, and X.-Q. Feng. “A multiscale crack-bridging model of cellulose nanopaper”, *Journal of the Mechanics and Physics of Solids*, **103**: 22–39, (2017). DOI:10.1016/j.jmps.2017.03.004.
- [173] A. S. Abhilash, P. K. Purohit, and S. P. Joshi. “Stochastic rate-dependent elasticity and failure of soft fibrous networks”, *Soft Matter*, **8**: 7004–7016, (2012). DOI:10.1039/C2SM25450F.
- [174] S. Yun, J. H. Kim, Y. Li, and J. Kim. “Alignment of cellulose chains of regenerated cellulose by corona poling and its piezoelectricity”, *Journal of Applied Physics*, **103**: 083301, (2008). DOI:10.1063/1.2908883.
- [175] C. Yang, J.-H. Kim, J.-H. Kim, J. Kim, and H. S. Kim. “Piezoelectricity of wet drawn cellulose electro-active paper”, *Sensors and Actuators A: Physical*, **154**: 117–122, (2009). DOI:10.1016/j.sna.2009.07.016.
- [176] R. F. Service. “A battery made with paper: Nanotubes on photocopy paper could lead to cheap, flexible source of power”, *American Association for the Advancement of Science: Science*, (2009). DOI:10.1126/article.31438.

- [177] L. Zeng, S. Chen, M. Liu, H.-M. Cheng, and L. Qiu. “Integrated paper-based flexible li-ion batteries made by a rod coating method”, *American Chemical Society Applied Materials and Interfaces*, **11**: 46776–46782, (2019). DOI:10.1021/acsami.9b15866.
- [178] S. Östlund and M. Nygåards. “Through-thickness mechanical testing and computational modelling of paper and board for efficient materials design”, in *Hannu Paulapuro Symposium, Esbo, Finland*: 69–82, (2009).
- [179] M. Nygåards, C. Fellers, and S. Östlund. “Measuring Out-of-Plane Shear Properties of Paperboard”, *JOURNAL OF PULP AND PAPER SCIENCE*, **33**(2): 6, (2007).
- [180] M. Nygåards. “Experimental techniques for characterization of elasticplastic material properties in paperboard”, *Nordic Pulp & Paper Research Journal*, **23**(4): 432–437, (Dec. 2008). DOI:10.3183/npprj-2008-23-04-p432-437.
- [181] M. Nygåards, N. Hallbäck, M. Just, and J. Tryding. “A finite element model for simulations of creasing and folding of paperboard”, in *ABAQUS User’s Conference*: 1–15, (2005).
- [182] M. Jajcinovic, W. J. Fischer, A. Mautner, W. Bauer, and U. Hirn. “Influence of relative humidity on the strength of hardwood and softwood pulp fibres and fibre to fibre joints”, *Cellulose*, **25**(4): 2681–2690, (Apr. 2018). DOI:10.1007/s10570-018-1720-8.
- [183] V. Placet, O. Cisse, and M. L. Boubakar. “Influence of environmental relative humidity on the tensile and rotational behaviour of hemp fibres”, *Journal of Materials Science*, **47**(7): 3435–3446, (Apr. 2012). DOI:10.1007/s10853-011-6191-3.
- [184] A. J. Benítez, J. Torres-Rendon, M. Poutanen, and A. Walther. “Humidity and Multiscale Structure Govern Mechanical Properties and Deformation Modes in Films of Native Cellulose Nanofibrils”, *Biomacromolecules*, **14**(12): 4497–4506, (Dec. 2013). DOI:10.1021/bm401451m.
- [185] Q. Meng and T. J. Wang. “Mechanics of Strong and Tough Cellulose Nanopaper”, *Applied Mechanics Reviews*, **71**(4): 040801, (July 2019). DOI:10.1115/1.4044018.
- [186] A. Moropoulou and S. Zervos. “The Immediate Impact of Aqueous Treatments on the Strength of Paper”, *Restaurator*, **24**(3): 160–177, (Jan. 2003). DOI:10.1515/REST.2003.160.
- [187] T. Vitale. “Effects of Water on the Mechanical Properties of Paper and their Relationship to the Treatment of Paper”, *MRS Proceedings*, **267**: 397–427, (1992). DOI:10.1557/PROC-267-397.

- [188] H. W. Haslach, Jr. “The moisture and rate-dependent mechanical properties of paper: A review”, *Mechanics of Time-Dependent Materials*, **4**(3): 169–210, (2000). DOI:10.1023/A:1009833415827.
- [189] J. Ko, K. Cho, S. W. Han, H. K. Sung, S. W. Baek, W.-G. Koh, and J. S. Yoon. “Hydrophilic surface modification of poly(methyl methacrylate)-based ocular prostheses using poly(ethylene glycol) grafting”, *Colloids and Surfaces B: Biointerfaces*, **158**: 287–294, (2017). DOI:10.1016/j.colsurfb.2017.07.017.
- [190] M. F. Kanninen. “An augmented double cantilever beam model for studying crack propagation and arrest”, *International Journal of Fracture*, **9**: 83–92, (1973). DOI:10.1007/BF00035958.
- [191] J. W. Hutchinson and A. G. Evans. “Mechanics of materials: Top-down approaches to fracture”, *Acta Materialia*, **48**: 125–135, (2000). DOI:10.1016/S1359-6454(99)00291-8.
- [192] S. Gowrishankar, H. Mei, K. M. Liechti, and R. Huang. “A comparison of direct and iterative methods for determining traction-separation relations”, *International Journal of Fracture*, **177**: 109–128, (2012). DOI:10.1007/s10704-012-9758-3.
- [193] J. R. Rice. “A path independent integral and the approximate analysis of strain concentration by notches and cracks”, *Journal of Applied Mechanics*, **35**: 379–386, (1968).
- [194] J. R. Rice. “Mathematical analysis in the mechanics of fracture”, in *Fracture: An Advanced Treatise* (H. Liebowitz, ed.): ch. 3, 191–311. New York: Academic Press, (1968).
- [195] V. Tvergaard and J. W. Hutchinson. “The relation between crack growth resistance and fracture process parameters in elastic-plastic solids”, *Journal of the Mechanics and Physics of Solids*, **40**(6): 1377–1397, (1992). DOI:10.1016/0022-5096(92)90020-3.
- [196] M. F. Kanninen and C. H. Popelar. *Advanced Fracture Mechanics*. New York: Oxford University Press, New York, (1985).
- [197] M. Thouless and Q. Yang. “Chapter 7 - measurement and analysis of the fracture properties of adhesive joints”, in *Adhesion Science and Engineering* (D. Dillard, A. Pocius, and M. Chaudhury, eds.): 235–271. Amsterdam: Elsevier Science B.V., (2002). DOI:10.1016/B978-0-444-51140-9.50034-2.

- [198] B. H. River and E. A. Okkonen. “Contoured Wood Double Cantilever Beam Specimen for Adhesive Joint Fracture Tests”, *Journal of Testing and Evaluation*, **21**(1): 21–28, (1993). DOI:10.1520/JTE11737J.
- [199] R. Long and C.-Y. Hui. “Fracture toughness of hydrogels: measurement and interpretation”, *Soft Matter*, **12**: 8069–8086, (2016). DOI:10.1039/C6SM01694D.
- [200] M. Lee, S. Kim, H.-Y. Kim, and L. Mahadevan. “Bending and buckling of wet paper”, *Physics of Fluids*, **28**(4): 042101, (Apr. 2016). DOI:10.1063/1.4944659.
- [201] E. Linvill and S. Östlund. “The Combined Effects of Moisture and Temperature on the Mechanical Response of Paper”, *Experimental Mechanics*, **54**(8): 1329–1341, (Oct. 2014). DOI:10.1007/s11340-014-9898-7.
- [202] S. Zauscher, D. F. Caulfield, and A. H. Nissan. “The influence of water on the elastic modulus of paper”, *Tappi Journal*, **80**(1): 214–223, (1997).
- [203] D. Caulfield. “Effect of Moisture and Temperature on the Mechanical Properties of Paper”, in *Solid Mechanics Advances in Paper Related Industries* (R. W. Perkins, R. E. Mark, and J. L. Thorpe, eds.), Proceedings of the National Science Foundation Workshop: 50–62, (1990).
- [204] X. Liang, J. Shin, D. Magagnosc, Y. Jiang, S. Jin Park, A. John Hart, K. Turner, D. S. Gianola, and P. K. Purohit. “Compression and recovery of carbon nanotube forests described as a phase transition”, *International Journal of Solids and Structures*, **122-123**: 196–209, (2017). DOI:10.1016/j.ijsolstr.2017.06.025.
- [205] V. Negi and R. Picu. “Mechanical behavior of cross-linked random fiber networks with inter-fiber adhesion”, *Journal of the Mechanics and Physics of Solids*, **122**: 418–434, (Jan. 2019). DOI:10.1016/j.jmps.2018.09.027.
- [206] S. R. Burke, M. E. Möbius, T. Hjelt, and S. Hutzler. “Properties of lightweight fibrous structures made by a novel foam forming technique”, *Cellulose*, **26**(4): 2529–2539, (Mar. 2019). DOI:10.1007/s10570-018-2205-5.
- [207] V. Tutwiler, F. Maksudov, R. I. Litvinov, J. W. Weisel, and V. Barsegov. “Strength and deformability of fibrin clots: Biomechanics, thermodynamics, and mechanisms of rupture”, *Acta Biomaterialia*, **131**: 355–369, (2021). DOI:10.1016/j.actbio.2021.06.046.

- [208] J. Deng, Y. Xu, S. He, P. Chen, L. Bao, Y. Hu, B. Wang, X. Sun, and H. Peng. “Preparation of biomimetic hierarchically helical fiber actuators from carbon nanotubes”, *Nature Protocols*, **12**: 1349–1358, (2017). DOI:10.1038/nprot.2017.038.
- [209] Z.-L. Zhao, H.-P. Zhao, J.-S. Wang, Z. Zhang, and X.-Q. Feng. “Mechanical properties of carbon nanotube ropes with hierarchical helical structures”, *Journal of the Mechanics and Physics of Solids*, **71**: 64–83, (2014). DOI:10.1016/j.jmps.2014.06.005.
- [210] L. Hu, J. W. Choi, Y. Yang, S. Jeong, F. L. Mantia, L.-F. Cui, and Y. Cui. “Highly conductive paper for energy-storage devices”, *Proceedings of the National Academy of Sciences*, **106**(51): 21490–21494, (2009). DOI:10.1073/pnas.0908858106.